UNIVERSITA' DEGLI STUDI DI PADOVA

DIPARTIMENTO DI INGEGNERIA INDUSTRIALE

CORSO DI LAUREA MAGISTRALE IN INGEGNERIA ENERGETICA

TESI DI LAUREA MAGISTRALE

OPTIMAL HELIOMOBILE FIELD CONFIGURATIONS IN A VARIABLE-GEOMETRY TEST FACILITY FOR CENTRAL RECEIVER SOLAR SYSTEMS

RELATORE: PROF. DAVIDE DEL COL

Dipartimento di Ingegneria Industriale

CORRELATORE: PROF. MANUEL ANTONIO SILVA PÉREZ

Departamento de Ingeniería Energética, Universidad de Sevilla

LAUREANDO: LUDOVICO CRESCIOLI

MATRICOLA N. 1038966

Sommario

Il solare termodinamico è oggi considerato uno tra i più promettenti sistemi a fonte rinnovabile in grado di attenuare parzialmente il consumo di fonti fossili, in un momento in cui la richiesta mondiale di energia aumenta anno dopo anno.
Tra i vari tipi di tecnologia CSP (*concentrated solar power*), i sistemi a collettori parabolici lineari hanno già raggiunto lo stadio di maturità commerciale, mentre i sistemi a torre centrale stanno vivendo un'epoca di rinnovato interesse, come testimoniato dai vari impianti la cui costruzione è in corso o già programmata.
Si evince dalla letteratura scientifica che la diffusione su larga scala di tali impianti è tuttavia ancora distante; da un punto di vista sia energetico che economico, la parte critica risulta essere il campo collettore, che ha il compito di concentrare la radiazione solare incidente: è infatti il sottosistema in cui si concentra fino al 40% del costo di investimento iniziale ed in cui si registrano le maggiori perdite energetiche.
Il nuovo apparato sperimentale per sistemi a torre a geometria variabile costruito presso il centro CTAER di Tabernas (Almería, Spagna) risponde dunque alle necessità di ricerca attuali ed è qui studiato in dettaglio per valutare la bontà dell'innovazione proposta.

Il presente lavoro vuole individuare il vantaggio, in termini di rendimento ottico, garantito da un sistema in cui il campo solare non è più fisso rispetto al ricevitore centrale, bensì segue il movimento apparente del sole durante il giorno. A ciò si aggiunge una seconda caratteristica, ossia che i singoli elementi concentratori, detti eliomobili, si muovono indipendentemente gli uni rispetto agli altri lungo una serie di circonferenze concentriche.
Le potenzialità di un ridotto apparato sperimentale composto da trenta elementi riflettenti sono stimate dopo un processo di ottimizzazione in cui vengono calcolate le configurazioni di campo che massimizzano l'energia convogliata al ricevitore in funzione dell'elevazione solare considerata. Successivamente, tale campo ottimizzato è comparato con un campo fisso ed un altro a geometria variabile in cui le distanze relative tra gli eliomobili di una stessa rotaia non cambiano durante il giorno. Il confronto è stato realizzato a parità di ricevitore e di elementi concentratori, tanto in numero quanto in dimensioni.

Il modello matematico sviluppato ed implementato in Matlab© per il calcolo del rendimento ottico è stato validato attraverso il software di ray-tracing Tonatiuh©. Il risultato finale conferma che un campo mobile è in grado di concentrare durante l'anno una significativa quantità di energia in più al ricevitore, principalmente a causa della riduzione delle perdite energetiche per effetto coseno e spillage. In secondo luogo, non si osserva una sostanziale differenza tra le due tipologie di campo variabile, indicando dunque che un numero limitato di eliomobili consente l'adozione di una semplice strategia operativa senza che venga penalizzato eccessivamente il rendimento ottico annuale.

Abstract

Concentrated Solar Power is nowadays seen as one of the most promising technologies able to replace partially fossil fuel consumption in a world that is increasing energy demand year by year.
Inside CSP world, central receiver systems, known also as solar tower systems, are living an era of renewed interest, witnessed by the number of plants under construction and planned. At the current status, parabolic trough systems have already reached commercial development, but research and improvements project solar towers to the leading actor role: the main advantage is their higher operating temperatures which allow greater efficiencies and ease energy storage. In other words, the capacity factor would be raised, maximizing the value of the electricity generated, and minimizing the levelized cost of energy (LCOE) of such plant.
Before these kind power plant will become widespread, the path is still long and existing scientific literature stresses the need of new ideas and studies able to increase technology performances; this suggestion concerns, above all, the most critical part of the plant: the collector field. It represents alone about the 40% of the total capital cost of a typical power plant and, at the same time, it's the subsystem where the highest absolute value of energy losses occurs. An example of these research efforts is embodied in the new Variable-Geometry Central Receiver System Test Facility located at CTAER, in Tabernas (Almería, Spain), which is studied in detail herein in order to assess its main benefits.

This work focuses on the advantages, in terms of optical efficiency, guaranteed by a system where the solar field is not anymore fixed with respect to the central receiver, but follows the apparent path of the sun during the day. In addition, this innovative concept presents a second characteristic: reflective elements, called here heliomobiles, move independently from each other on concentric rails.
The potential of a small test facility made up of 30 heliomobiles is evaluated after an optimization process which determines the best field configurations as function of the considered solar elevation. Later, the optimized field is compared with other two: one fixed and one variable, where the distance between successive elements on the same rail does not change according to the considered time of the day. Such comparison is *ceteris paribus*.

The developed mathematical model has been implemented in Matlab© and validated through the ray-tracing software Tonatiuh©. The conclusive analysis proves that a variable-geometry field can convey a substantial amount of energy more at the receiver than the fixed one, mainly because of reduced cosine and spillage losses. Secondly, it's quite hard to appreciate the differences between the two different variable fields, meaning that a small number of heliomobiles does not require a complex operating strategy, as the annual optical efficiency is not penalized.

Index

List of Figures

List of Tables

1. Introduction

Analyzing energy trends in the world during the last four decades (1973-2013), it's well known that the amount of primary energy consumption is growing year by year at a high rate, as the graphic shows:

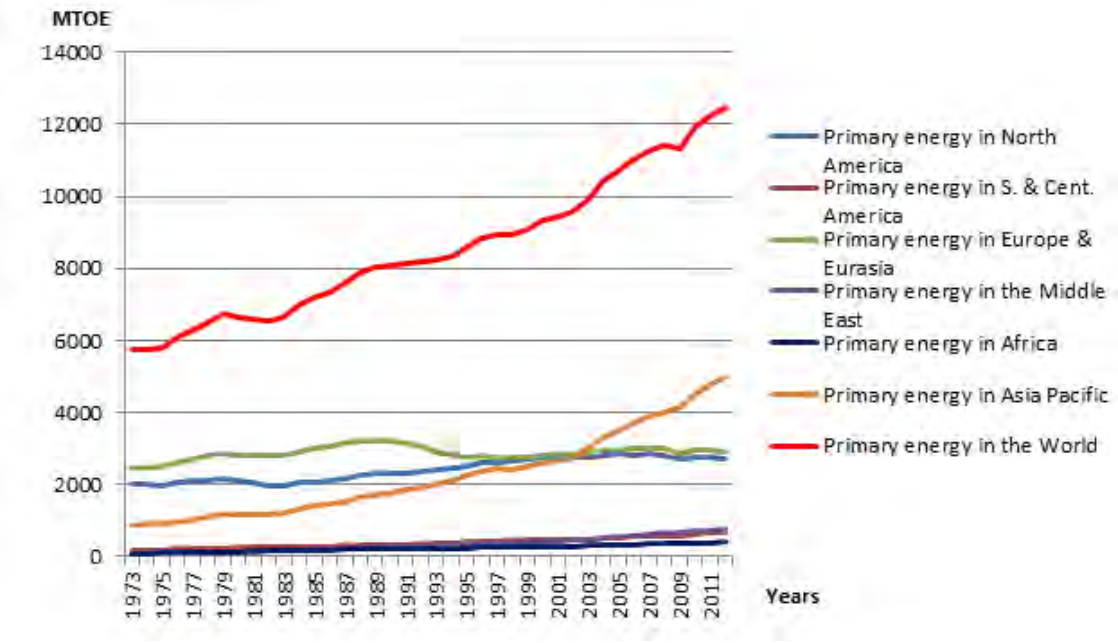

Figure 1-1: primary energy consumption 1973-2013, personal elaboration on BP data (BP, 2013)

Primary energy is energy proceeding from "the capture or extraction of fuels or energy from natural energy flows, the biosphere and natural reserves of fossil fuels within the national territory in a form suitable for use. Inert matter removed from the extracted fuels and quantities re-injected, flared or vented are not included" (United Nations, 2011). The unit of measurement is MTOE, i.e. the amount of energy embodied in a million tons of oil, equivalent to $41.87 \cdot 10^{15}$ J.
In less than forty years world primary energy demand doubled, moving from 6000 MTOE to more than 12000 MTOE in 2013.
In addition, it's worth observing how the human being is satisfying its energy need in the same period: in figure 2 it's possible to appreciate that the fossil-fuel share is almost the 87% of the total primary energy consumed in 2012. But where do we have to look for the reasons of this percentage? And what are its consequences in our world?

The roots of this energetic hunger lie in a technological, economic and social development which, above all during the last century, drove (only a) part of world's population to a standard of living and a life expectancy unknown in mankind history. Paradoxically, in 2012, still 1.3 billion people don't have access to electricity and 2.6 billion to clean cooking facilities (International Energy Agency, 2012).
This path has been followed thanks to high availability of low-cost fossil resources as well; at least this is true till 1979, when the biggest oil crisis took place, slowing oil, natural gas and coal production for some years.

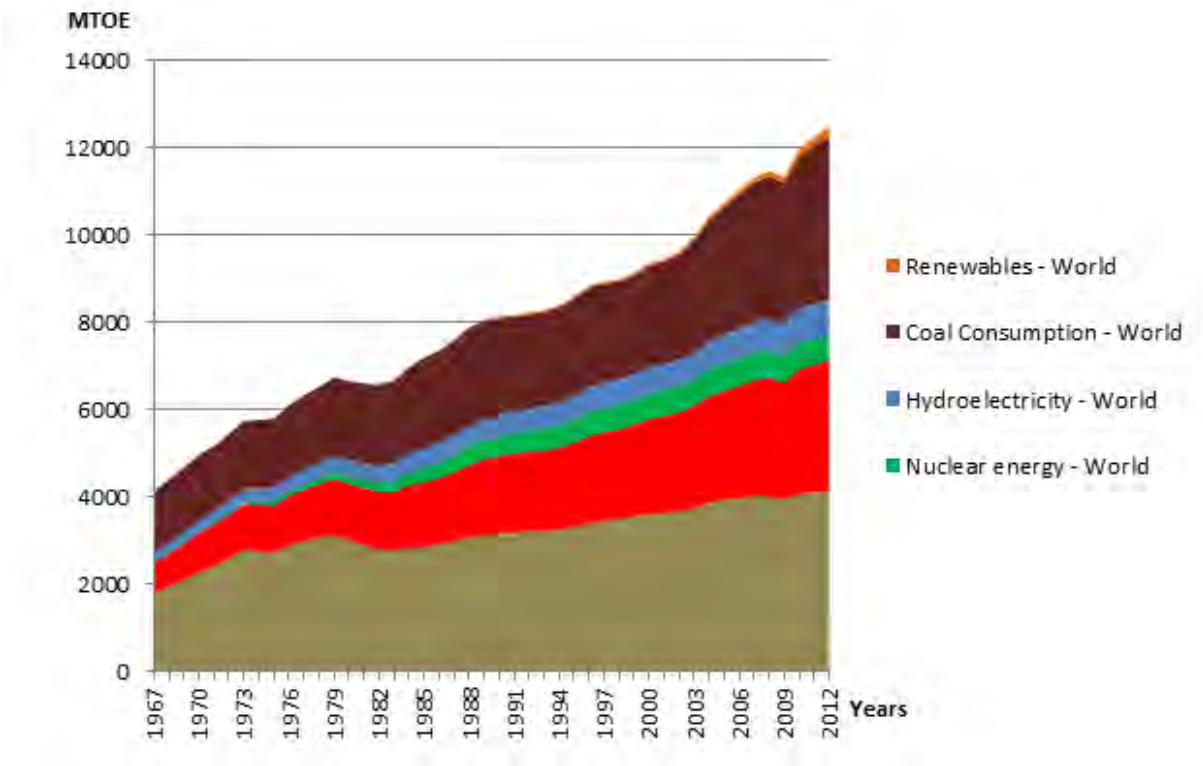

Figure 1-2: primary energy consumption by fuel 1973-2013, personal elaboration on BP data (1)

In parallel, the major problems connected to the current global energy system are mainly four: the emission of pollutants and CO_2 due to combustion of fossil sources, their progressive depletion in an uncertain time, their increasing prices and the strong dependence on few suppliers that many countries have to face with.

About the first topic, it results in a local lower air quality and CO_2 concentration is held the major responsible for anthropic contribution to climate change. The International Energy Agency (IEA) points out that the goal of limiting global warming to 2 C is becoming more difficult and costly while the years are passing (International Energy Agency, 2012). On the other side, China, India, the Middle East and all the emerging economies (except Brazil) are expected to boost especially their coal and oil demand. Nowadays, gas and oil production is the hands of few exporters But even if new extraction techniques, such as unconventional gas and light tight oil, are pushing up the availability estimates of those fuels, by the mid-2020s the OPEC production is supposed to hold again some 80% of the world's proven-plus-probable oil reserves, while the unconventional gas still shows uncertainty over the quality, the production cost and the public acceptance of the resource. It means that coal will be again the cheaper option for generating electricity, but its cut consumption could be crucial to mitigate climate change (International Energy Agency, 2012).

In this complex and uncertain scenario, renewable energies will gain a significant role in the global energy mix, reaching probably almost one-third of the total electricity output, depending on subsidies, fossil-fuel prices and fall of technology cost. Without any doubt it's one of energetic and economic sectors that grew the most in the last two decades.

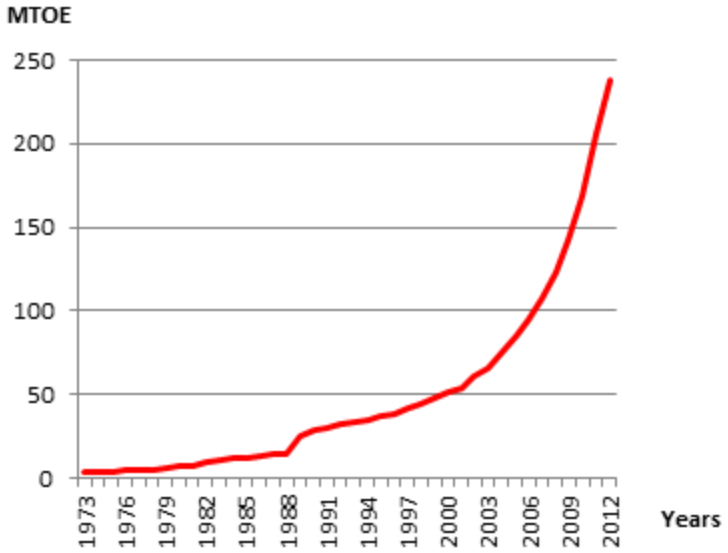

Figure 1-3: renewable energy growth 1973-2013, personal elaboration on BP data

Among these, solar sector is growing more rapidly than the others (International Energy Agency, 2012) (International Energy Agency, 2013), and *concentrated solar power* (CSP) seems the key for countries with plenty of sunshine and clear skies: a typical plant uses mirrors to concentrate sunlight onto a receiver, which collects and transfers the solar energy to a heat transfer fluid that can be used to supply heat for end-use applications or to generate electricity through conventional thermodynamic cycles. It gives the possibility to decouple heat and/or electricity production from solar radiation, and it could be backed up by thermal storage and/or hybridized with combustible fuels.
CSP could appear nothing more than a strong competitor for PV systems, but, on the contrary it means a completely different approach in generating electricity from the Sun, no longer based on a photochemical reaction, but on high-temperature heat absorption, accumulation and storage. From a practical point of view, this characteristic allows a CSP plant to produce even when sun is absent, under favorable conditions during the daytime.

Currently, CSP plants can be grouped into four categories: parabolic through, linear Fresnel, solar dish and central receiver systems. All of them require abundant direct solar radiation to be cost effective, at least 2000 kWh/m^2/year, even though there is no technical limitation at lower irradiation levels.
Coupling this characteristic with the large space needed for their installation, it is possible to identify a number of suitable sites, including Middle East, North Africa, South Africa, India, Southwest of the United States, Mexico, Peru, Chile, Western China, Australia, southern Europe and Turkey.
In 2012 CSP installed capacity for electricity generation was approximately 2GW, while 12GW were planned for installation by 2015. Parabolic trough are now market leaders with more than 90% of total installed capacity; maturated experience provides an estimate of their LCOE, which ranges between 0,14 and 0,36€/kWe (IRENA, 2012). On the other hand, central receiver systems are slightly more expensive, being their LCOE about 0,17 to 0,29€/kWe. In both cases, feed-in tariffs and electricity market regulation are necessary, as witnessed by USA and Spain, where support policies have been introduced in the last decade.

However, it's worth reminding that several studies have already demonstrated a possible substantial cost reduction, as the LCOE is sensitive to plant size, economy of scale, DNI, capacity factor, thermal storage and, not least, fossil fuel prices.

In this scenario, central receiver systems have an undisputable advantage as they are able to reach high temperatures while keeping a considerable plant size; coupling these features with a thermal storage system, capacity factor and plant efficiency would raise, reducing the LCOE. Unlike parabolic trough systems, the LCOE of solar towers tends to decrease as the capacity factor increases. This is mainly due to the significantly lower specific cost (up to three times lower) of the molten-salt energy storage in solar tower plants.

Analyzing the cost breakdown of a typical central receiver system, about the 40% of capital investment cost, which dominates the total cost, is concentrated into the solar field. Beside mass production, cheaper components and new materials, a wise idea for cost reduction is to explore and search for new subsystem designs, like the one projected for the variable-geometry test facility at the CTAER in Almería (Spain).
Mainly developed during the internship at AICIA (Seville, Spain), this work aims to calculate the optimal deployment of the mobile reflective elements in the field and to point out the main benefits and drawbacks of such innovative concept. These two tasks are realized through an optical model of the solar field, written in Matlab environment, and thanks to the open-source ray-tracing software Tonatiuh.

First a review of the state of art of CSP technology is made; then a more detailed description of a conventional central receiver system, its applications and subsystems, especially the collector field, is reported.
As this is the central theme of the work, a review of existing heliostat field layouts and computer tools for system design and analysis is carried out. After the mathematical model is explained, the optimization process for the variable-geometry collector field is introduced, together with a possible operating strategy.
Comparisons between three different kinds of field are finally presented: the analysis is performed on annual, monthly and daily basis, while the validation of the optical efficiency closes the thesis.

2. CSP Systems

Solar radiation is a source of high temperature and energy at origin, with a high irradiance of 63 MW/m^2, but Sun–Earth geometrical constraints lead to a dramatic dilution of flux and the irradiance available for terrestrial use is only slightly higher than 1 kW/m^2. Therefore, it's possible to overcome this low-energy density radiation by making use of optical concentration. Interposing an optical device between the source of radiation and an energy-absorber surface, the goal, in other words, is to concentrate solar radiation onto a reduced area, thus obtaining a higher thermal flux and lowering heat losses. This means a higher absorber temperature.
According to thermodynamics, the conversion of heat to mechanical work will be more efficient the higher the temperature is.

A generic scheme of a CSP system is illustrated below, the optical device tracks the Sun continuously and collects sunlight onto a receiver, which can produce heat or mechanical work through a conventional thermodynamic cycle, which can be back upped with fossil fuels. In the image all the different subsystems are represented, together with energy storage and corresponding heat fluxes.

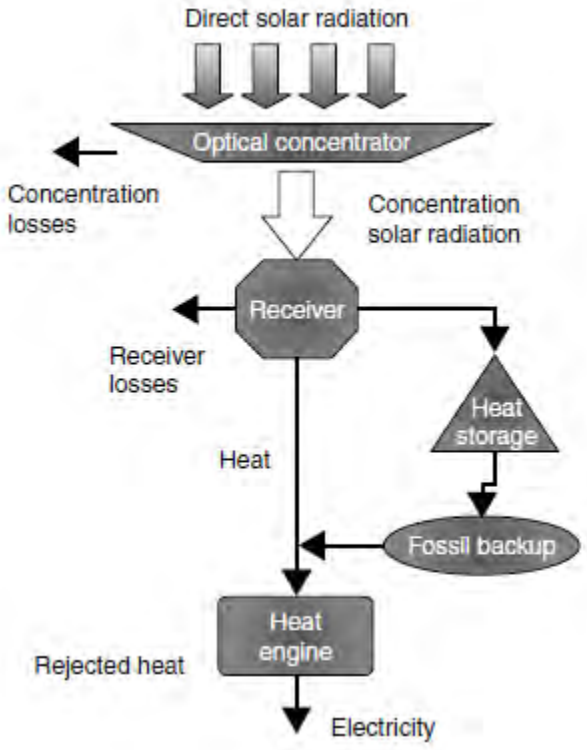

Figure 2-1: CSP scheme (Romero-Alvarez M., 2007)

2.1 Theoretical Background

In the following figure a generic concentrator is represented

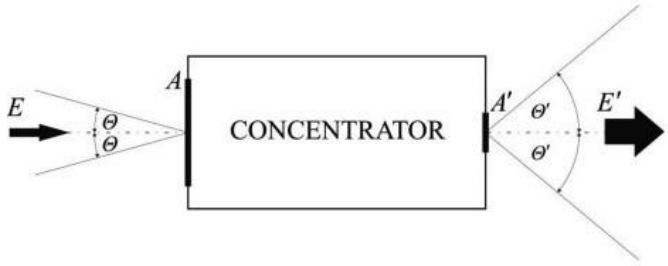

Figure 2-2: scheme of a generic concentrator (Pitz-Paal, 2007)

The energy flux E (in W/m^2), described by a cone with half angle θ, enters through an aperture area A (in m^2) and leaves the system once concentrated into the absorber area $A'<A$ (in m^2).
In the hypothesis that no losses occur in the system, the conservation energy law affirms that:

$$E \cdot A = E' \cdot A'$$

The geometric concentration ratio C is defined as:

$$C = \frac{A}{A'} = \frac{A_{collector}}{A_{absorber}}$$

This ratio has an upper limit that depends on the concentrator type: a three-dimensional concentrator (paraboloid) will better perform than a two-dimensional one (parabolic trough). The reason is explained following the thermodynamic approach by Rabl (Rabl, 1975).

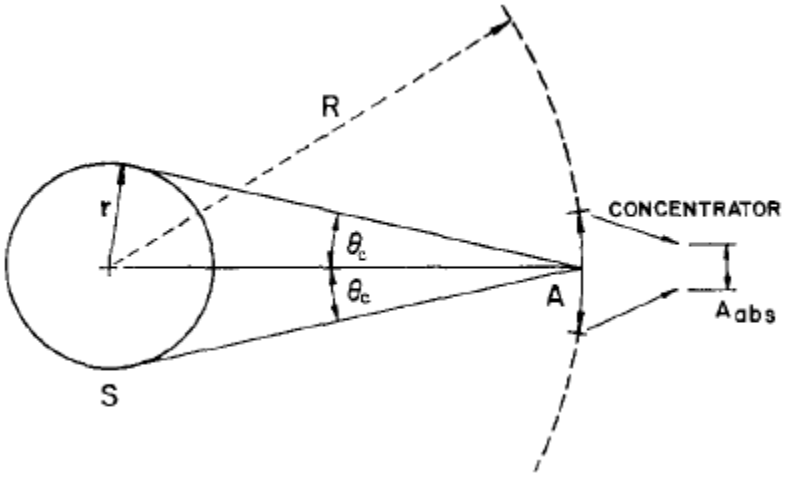

Figure 2-3: radiation transfer from source S through aperture A of the concentrator to absorber surface (Rabl, 1975)

Sun is not a radiative point source, the shape that is fitting best is a disc, and the half angle subtended by solar radiation is θ_c (4,653 mrad). In the next part it is assumed that Sun and absorber are two blackbodies, the source a isotropically radiating sphere of radius r and its aperture area A is normal to the line from source to aperture and at a distance R away from the

center of the source ($A<<R^2$). In addition the source and the absorber surface are at initial temperatures T_S and T_{abs}.
A black body is an ideal physical body that absorbs all incident radiation, its spectrum only depends on its superficial temperature and, for Kirchhoff's law, its absorptivity equals the emissivity:

$$\alpha = \varepsilon = 1$$

$$\rho = \tau = 0$$

If the concentration is perfect, the amount of radiation from the sun on the concentrator will be the fraction of the radiation intercepted by the aperture:

$$Q_{rad} = (4\pi r^2)\ \sigma T_S^4$$

$$F_{S\to A} = \frac{A}{4\pi R^2}$$

$$Q_{rad,S\to A} = F_{S\to A} Q_{rad} = A\frac{r^2}{R^2}\ \sigma T_S^4$$

At the same time the absorber radiates:

$$Q_{rad,abs} = A_{abs}\sigma T_{abs}^4$$

where σ is the Stephan-Boltzmann constant. Only a fraction $F_{A,abs->S} \leq 1$ is redirected to the source:

$$Q_{rad,A\to S} = F_{A_{abs}\to S} A_{abs}\sigma T_{abs}^4$$

When the steady-state is reached, the two black bodies have the same temperature T, which implies:

$$Q_{rad,S\to A} = Q_{rad,A\to S}$$

$$A\frac{r^2}{R^2}\ \sigma T^4 = F_{A_{abs}\to S} A_{abs}\sigma T^4$$

The last equation leads directly to concentration ratio expression:

$$C = \frac{A}{A_{abs}} = \frac{r^2}{R^2} F_{A_{abs}\to S} = \frac{F_{A_{abs}\to S}}{(\sin\theta)^2}$$

$$C \leq \frac{1}{(\sin\theta)^2}$$

If the absorber lays in a transparent medium, whose index of refraction is n, the incident radiation is restricted to angles $\theta \leq \theta_n$. According to Snell's law, when the radiation changes medium, the ratio of the sines of the angle of incidence is equivalent to the reciprocal of the ratio of the refraction indices:

$$\frac{\sin\theta_c}{\sin\theta_n} = \frac{n}{n_c}$$

$$\sin\theta_n = \frac{\sin\theta_c}{n}$$

The new incidence angle to the aperture modifies the concentration ratio expression, in the hypothesis that $n_c = 1$:

$$C_{3D} \leq \left(\frac{n}{\sin\theta_c}\right)^2 \approx 46200$$

This limit can be achieved by a point-focus ideal concentrator, a device able to redirect solar radiation onto one point thanks to a continuous two-axis tracking system; for a line-focus collector (i.e. parabolic trough) the limit is lower, as concentrated radiation now is spread over a line:

$$C_{2D} \leq \frac{n}{\sin\theta_c} \approx 215$$

Concentrators can be divided also by another category; it's common to distinguish imaging from nonimaging optics. The first group identifies those concentrators that reproduce the Sun image on the absorber, by the means of reflective, refractive or diffractive lens or mirror system; nonimaging optics on the other side doesn't attempt to create any image of the source on the target, but rather distribute radiation from all part of the solar disc onto all parts of the absorber (Duffie & Beckman, 2006). Typical examples of the two groups are, respectively, parabolic dish for imaging optics and CPC (compound parabolic concentrator).

Going back to figure 4, it's time to understand the energy balance at the receiver. The power sent by the collector system defines the optical efficiency of the concentrator:

$$\eta_{opt} = \frac{\dot{Q}_{rec}}{\dot{Q}_{available}}$$

$$\dot{Q}_{available} = \int_{refl.\ Surface} I_{b,n}\ dS$$

The receiver is designed to absorb the maximum concentrated radiation, while transferring as much energy as possible to a heat transfer fluid; an ideal receiver would be a blackbody which would present only emission losses. In real applications, it can't be because of the high temperature and the convection heat exchange with the environment.
When the collector begins to concentrate solar radiation onto the receiver surface, its temperature starts to grow and, at the same time, losses mechanism takes place; the process is time-variant till steady state is reached: in that moment energy input from the collector system will be equal to the heat outflow to the heat transfer medium and thermal losses. Thermal power inflow is split into two parts, one is absorbed by the surface and other reflected and transmitted. This happens because real surfaces are modelled as grey bodies and they radiate a constant fraction of black-body energy levels ($0 < \varepsilon < 1$), in addition absorptivity (α), transmissivity (τ) and reflectivity (ρ) are supposed constant across all wavelengths:

$$\dot{Q_{in}} = \alpha \int_{Aperture} \int_{refl.\ Surface} I_{b,n}(t)\ dS\ dA = \alpha A_{rec} C I_{b,n}$$

$$\dot{Q_{abs}} = \dot{m_{HTF}}(h_{out} - h_{in})$$

$$\dot{Q_{in}} = \dot{Q_{abs}} + \dot{Q_{loss}}$$

The total loss is the sum of radiative, convective, conductive and reflective contribution:

$$\dot{Q_{loss}} = \dot{Q_{rad}} + \dot{Q_{conv}} + \dot{Q_{cond}} + \dot{Q_{refl}}$$

Radiative loss is accounted as the most dissipative process as receiver surface emits thermal power proportionally to the fourth power of the temperature, at a rate fixed by its emissivity. For sake of simplicity, assuming a constant temperature for the absorber surface, the energy loss is calculated:

$$\dot{Q_{rad}} = \sigma A_{rec} \varepsilon\ F_{r \to env}(T_{rec}^4 - T_{env}^4)$$

σ is the Stefan–Boltzmann constant [5.67e-08 W/m^{2}K^4], ε is the hemispherical emissivity of the absorber, T_{rec} is the temperature (homogeneous) of the absorber (in K), and T_{env} is the effective temperature of ambient or atmosphere "viewed" by the absorber (in K). $F_{r \to env}$ is a simplified shape factor between receiver and surroundings, added to remember that during a radiative heat transfer the radiation leaving a surface can be intercepted by several other surfaces; the amount of radiation sent to each element depends on the shape factor, which is a geometric factor.

Reflection loss is the loss due to the sunlight reflected from the receiver: a grey body can't absorb all the incoming radiation. This means it will be partly absorbed, reflected and transmitted, and it's taken into account in the balance as the amount of radiation that is not absorbed at the aperture:

$$\dot{Q_{refl}} = (1 - \alpha_{aperture}) A_{rec} C I_{b,n}$$

The movement of air or any fluid around the receiver provokes convection losses; in most of CSP applications it is the sum of forced convection caused by the wind and natural convection originated from local heated air. Some difficulties arise because radiation influences convection and vice versa, both depend on receiver surface and surface temperature. It's common to turn to heat transfer simulation programs that enable computational fluid dynamics or to simplified models in order to decouple the two different contributions, or even to semi-empirical correlations, even if with low accuracy (Lovegrove, 2012). The general expression for this energy loss is:

$$\dot{Q_{conv}} = h A_{rec}(T_{rec} - T_{env})$$

h is the average convection heat transfer coefficient [W/m^{2}K].

Finally conduction losses take place because of heat transfer inside insulating covers and between hot surfaces that are exposed to surrounding environment. For a homogeneous material of 1-D geometry, two endpoints at different constant temperatures generate the following heat flow rate:

$$\dot{Q_{cond}} = k\frac{S}{L}(T_{S1} - T_{S2})$$

k is the thermal conductivity (in W/m·K), *L* is the thickness of the homogeneous material (in m), *S* the cross section of the surfaces considered (in m^2), T_{S1} and T_{S2} their temperatures (in K).

Previous relations lead to receiver efficiency; it is the ratio between the useful thermal flux directed to the heat transfer medium and the concentrated solar flux entering in the aperture:

$$\eta_{rec} = \frac{\dot{Q_{out}}}{CI_{b,n}A_{rec}} = \frac{\dot{Q_{in}} - \dot{Q_{loss}}}{CI_{b,n}A_{rec}}$$

In order to evaluate qualitatively the trend of receiver efficiency as function of receiver temperature and concentration factor, it's worth neglecting the term related to conduction and reflection losses, an operation made possible by the magnitude of radiative and convection contribution. The simplified expression of η_{rec} is:

$$\eta_{rec} = \alpha - \frac{\sigma\varepsilon(T_{rec}^4 - T_{env}^4)}{CI_{b,n}} - \frac{h(T_{rec} - T_{env})}{CI_{b,n}}$$

Assuming an ideal collector system, with unitary optical efficiency and:

- $\alpha = \varepsilon = 0{,}95$
- $\sigma = 5{,}67\text{e-}08$ W/m^{2}K^4
- $T_{env} = 298$ K
- $I_{b,n} = 800$ W/m^2
- $h = 20$ W/m^{2}K, only external convective loss

The following graphic is obtained:

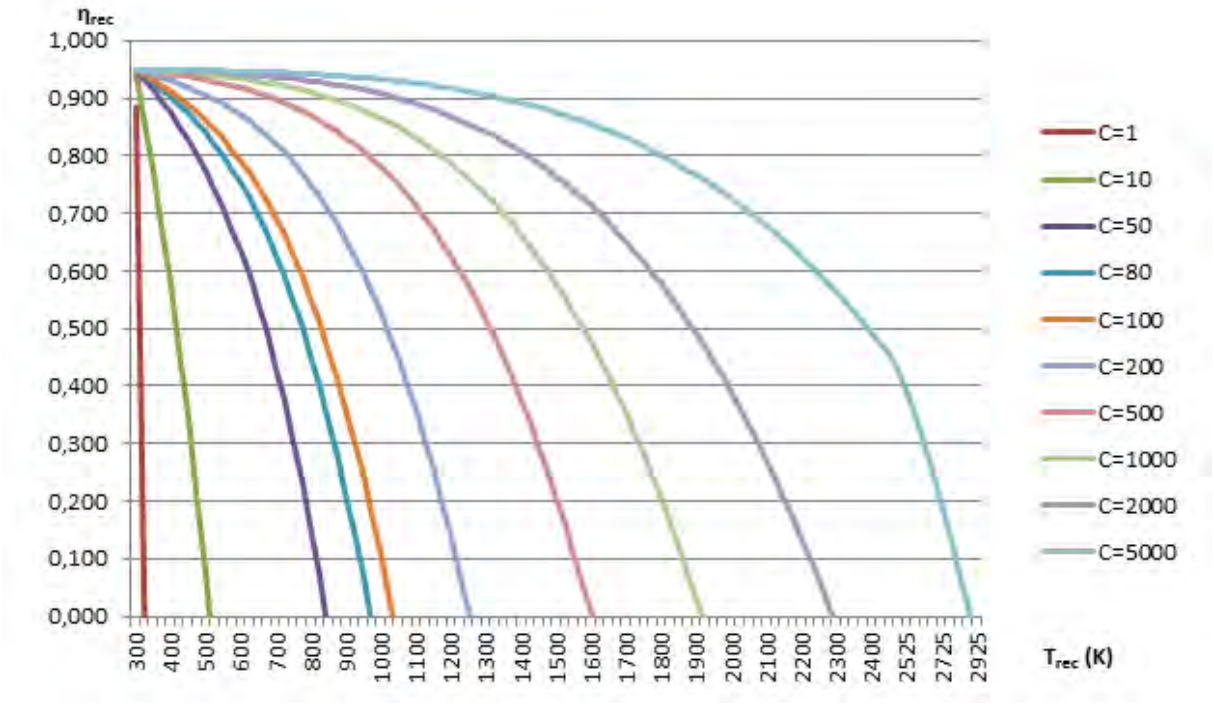

Figure 2-4: receiver efficiency as function of receiver temperature and concentration ratios

As ideal absorber temperature increases, thermal radiation losses increase as well. When losses and gains are equal; the net useful heat is zero and the receiver achieves the maximum temperature (stagnation temperature) (Romero-Alvarez M., 2007). It's represented in the graph by the intersection between each line and the horizontal axis, and it shows clearly a strong sensitiveness on absorptivity to emissivity ratio:

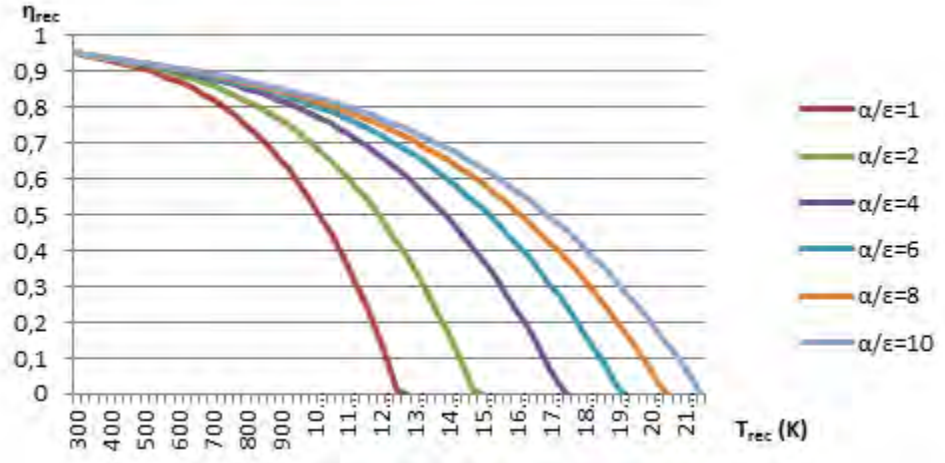

Figure 2-5: receiver efficiency as function of receiver temperature and absorptivity to emissivity ratio

In the figure above a concentration ratio of 200 was selected, then the receiver efficiency was calculated for six different absorptivity-to-emissivity ratios. Stagnation temperature rises according to the ratio.

This behavior is crucial in CSP applications, it happens because in a wide range of temperatures the receiver can't be considered a grey body, whose coefficients α and ε are

assumed constant throughout all solar spectrum. A typical absorber for concentrated solar power is covered by a selective coating, and that introduces an advantage when the need to play with radiative balances arises.
Kirchhoff's law states that at thermal equilibrium (constant temperature), for a particular surface, the monochromatic emissivity is equal to the monochromatic absorptivity:

$$\alpha(\lambda) = \varepsilon(\lambda)$$

If the solar spectrum and the spectrum of the emitted thermal radiation are sufficiently different it would be possible to make use of a material whose α is characterized by a strong wavelength dependence, to achieve high values of the averaged absorptivity α and low values for the average emissivity ε (Pitz-Paal, 2007). For current state-of-art technology this is always true: solar spectrum is comparable to the one of a blackbody at 5777K, while a performing receiver reaches operating temperatures >1000°C. The path to follow is to approach high values of α in the visible wavelengths (390 ÷ 700 nm) and, in parallel, limit the emissivity till the infrared (700 nm ÷ 1 mm).

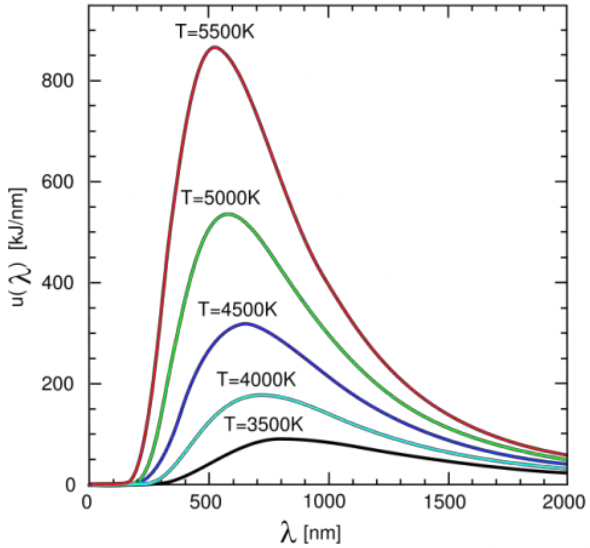

Figure 2-6: blackbody radiation spectrum as temperature function (from https://www.e-education.psu.edu/astro801/content/l3_p5.html)

The explained way to boost up receiver temperature is due to the electricity production, the higher the temperature of heat addition is, and the more efficient the transformation will be. When not employed to make process heat available at a desired temperature, those system are coupled with conventional thermodynamic cycles to generate mechanical/electric power. Before a detailed description of the cycles currently adopted, an idea about the possible global system efficiency (receiver and power cycle) derives from matching receiver efficiency with Carnot cycle efficiency. This is an idealized reversible process, consisting in two isothermal and two isentropic changes of state of the working fluid. Heat is absorbed at T_{rec}-dT and released at T_{env}+dT. In addition, this cycle efficiency reaches the theoretical maximum of any heat-to-mechanical energy conversion process, thus providing an upper limit. If η_{opt} = 1, α/ε = 1 and T_{env} = 298 K:

$$\eta_{Carnot} = \frac{W}{Q_{in}} = 1 - \frac{Q_{out}}{Q_{in}} = 1 - \frac{T_{env}}{T_{rec}}$$

$$\eta_{system} = \eta_{rec}\,\eta_{Carnot}$$

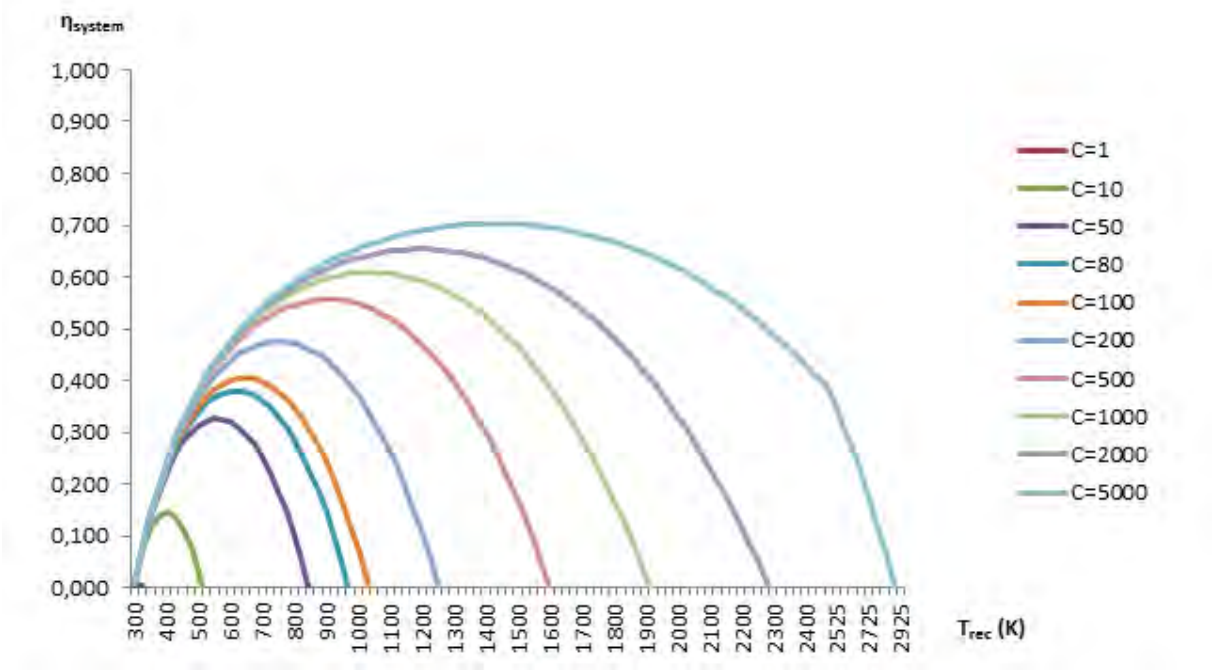

Figure 2-7: upper limit for system efficiency as function of receiver temperature

Although those curves come from an unreal ideal system, all of them clearly present a maximum; at a given concentration ratio an optimum temperature appears:

$$\frac{d\eta_{system}}{dT_{rec}} = 0$$

The found temperature will be the optimum operation temperature for the receiver. It's a crucial parameter for improving the performance of a CSP system as demonstrated by various exergetic analyses: the absorber/receiver subsystem rejects heat to the working fluid and the environment at a very high temperature. In this way the sum of radiative, convective and conductive losses (energy loss of high quality) lead to a significant amount of exergy destruction:

$$\dot{Ex}_{rec,loss} = \left(\dot{Q_{rad}} + \dot{Q_{conv}} + \dot{Q_{cond}} + \dot{Q_{refl}}\right)\left(1 - \frac{T_{env}}{T_{rec}}\right)$$

2.2 Technology description

A concentrated-solar system is defined by its:

- collector system and reflective surface
- receiver and absorber
- heat transfer fluid and heat storage system

and if it is designed to produce electric power:

- heat-to-electricity conversion process

The financial resources and the final use for collected heat are the basis upon which the correct alternative is selected. Space heating and cooling, industrial process heating, electric power (when coupled with a generator) or combined heat and power are the most common applications.
The collector system identifies the four variants of the current state-of-art technology; a further specification is made, separating in two groups the concentrators that focus the sun rays onto a line and the ones that focus onto a point. This is nothing more than the difference explained previously about concentration limit for three-dimensional and two-dimensional concentrators. As briefly said, the concentration ratio in the first case is limited to 60÷80, for a maximum achievable temperature of 550°C, but in the second the ratio is higher (>500), as the maximum temperature that can exceed 1000°C.

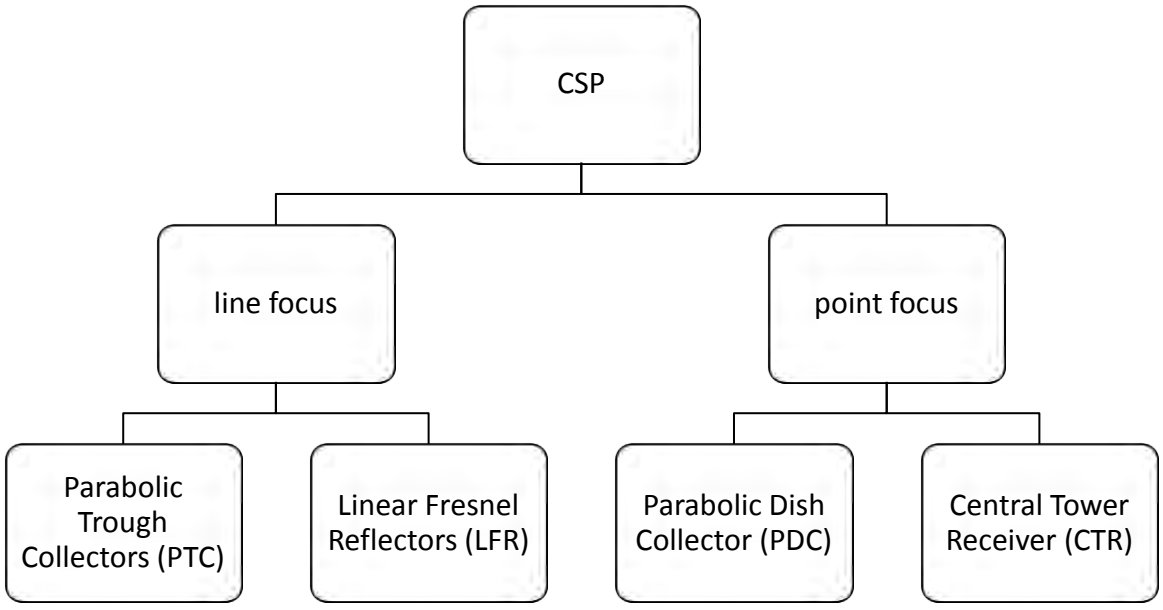

Technological maturity may change considerably when considering those systems: nowadays the market leaders are without any doubt parabolic trough collectors, thanks to their relative easy construction and the experience accumulated since the 80's of the last century. Central tower receivers are living a period of rapid growth as the efforts to reduce their LCOE (levelized cost of electricity) seem to be successful; pilot and demonstration phases ended,

paving the way to commercial scale future. Finally, Linear Fresnel reflectors are still at the pilot stage and parabolic dish collectors, already interesting for stand-alone systems, lack of thermal storage or hybridization, even if research is carried on.

2.2.1 Parabolic Trough Collectors

A PTC is basically made up of a parabolic trough-shaped mirror that reflects direct solar radiation, concentrating it onto a receiver tube located in the focal line of the parabola. With an average concentration factor of 60÷100, the HTF flows in a series of collectors and absorbs the heat warming up till the desired temperature is reached; then, a series of heat exchangers provide to supply steam to a conventional turbine that moves an alternator. The reflector structure is usually in steel or aluminum.
Reflector and absorber tube move together, rotate around an axis, the so-called tracking axis, to follow the apparent daily movement of the sun. The tracking can be N-S, when peak production during summer is the goal, or E-W, if seeking energy well distributed during the year.

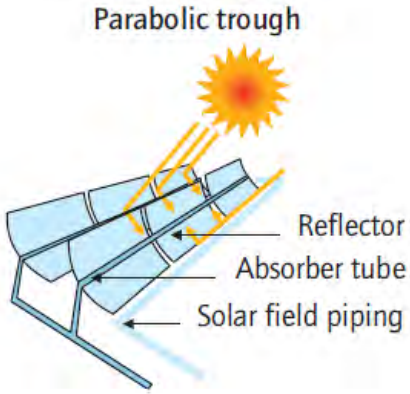

Overall length of a single collector (m)	98.5
Number of parabolic trough modules per collector	8
Gross length of every concentrator module (m)	12.27
Parabola width (m)	5.76
Outer diameter of steel absorber pipe (m)	0.07
Inner diameter of steel absorber pipe (m)	0.055
Number of ball joints between adjacent collectors	4
Net collector aperture per collector (m^2)	548.35
Peak optical efficiency	0.765
Cross section of the steel absorber pipes (m^2)	2.40×10^{-3}
Inner roughness factor of the steel absorber pipes (m)	4.0×10^{-5}
Relative roughness of the steel absorber pipes (m)	7.23×10^{-4}

Figure 2-8: PTC scheme (International Energy Agency, 2010) and Eurotrough collector characteristic parameters (Romero-Alvarez M., 2007)

A typical plant configuration adopted is illustrated in the following figure, which could represent the typical 50 MWe plant size (ex.: Andasol-1) with oil as transfer fluid and molten salts as thermal storage medium.

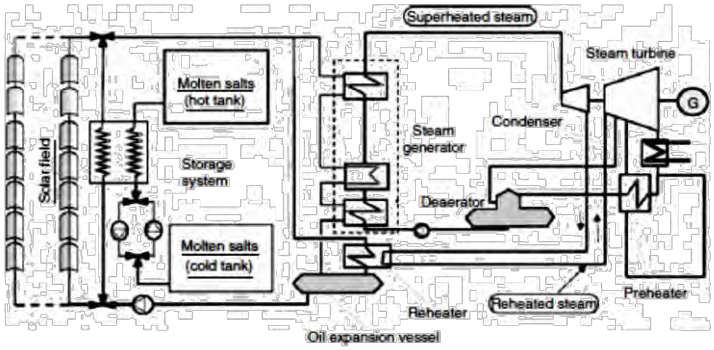

Figure 2-9: Parabolic trough plant scheme (Romero-Alvarez M., 2007)

Performance of such a plant is strongly influenced by the heat transfer medium. Synthetic oils are the most employed for application above 200°C: VP-1 is the most widely used in PTCs, for temperatures up to 395°C; it is a eutectic mixture of 73.5% diphenyl oxide and 26.5% biphenyl. Anyway, the most limiting factor to be taken into account is fluid stability: the high solidification temperature (14°C) requires an auxiliary electric heating system and the maximum temperature allowed is about 400°C, thus limiting the thermodynamic potential of such a plant. Secondary problems are the inflammability, the high capital cost and the intrinsic additional efficiency loss when this medium is coupled with molten salt energy storage to assure operation continuity even when the Sun is down. The diathermic oil heats the molten salt when solar resource exceed production capability, while during cloud period or night time the oil follows the reverse path. Because of the double heat exchange the temperature of the oil flowing to the steam generator at night is lower than the maximum nominal one. Those drawbacks induced several research programs focused on alternative mediums: molten salts, air and water/steam. In each case the goal is to improve plant efficiency and reduce its cost.

In order to ease steam production and avoid the cost and irreversibility represented by a heat exchanger, the DISS (Direct Solar Steam) program took place at the Plataforma Solar de Almería in 1999: steam at 100 bar and 400°C was generated directly in the trough pipe. This option seems interesting, but the slightly higher efficiency comes with more complex heat storage and biphasic fluid circulation.
When storing energy is the priority, molten salts are maybe the principal actors on the stage. It's a eutectic mixture, formed by 60% of sodium nitrate (NaNO3) and by 40% of potassium nitrate (KNO3); the low cost required, the large availability, non-toxicity and non-inflammability, the good heat transport properties and the a operative temperature of 260÷500°C make this medium suitable to satisfy thermal storage and to eliminate its relative heat exchanger. Having it a higher density, an additional positive side effect is that thermal storage requires less volume. Archimede Solar Energy has been the first company to investigate this medium also as HTF, coupling it to a tube absorber with selective coating. Unfortunately, despite the advantages, the high freezing temperature (238°C) is still the main critical issue, implying difficult start-up operation and substantial maintenance.

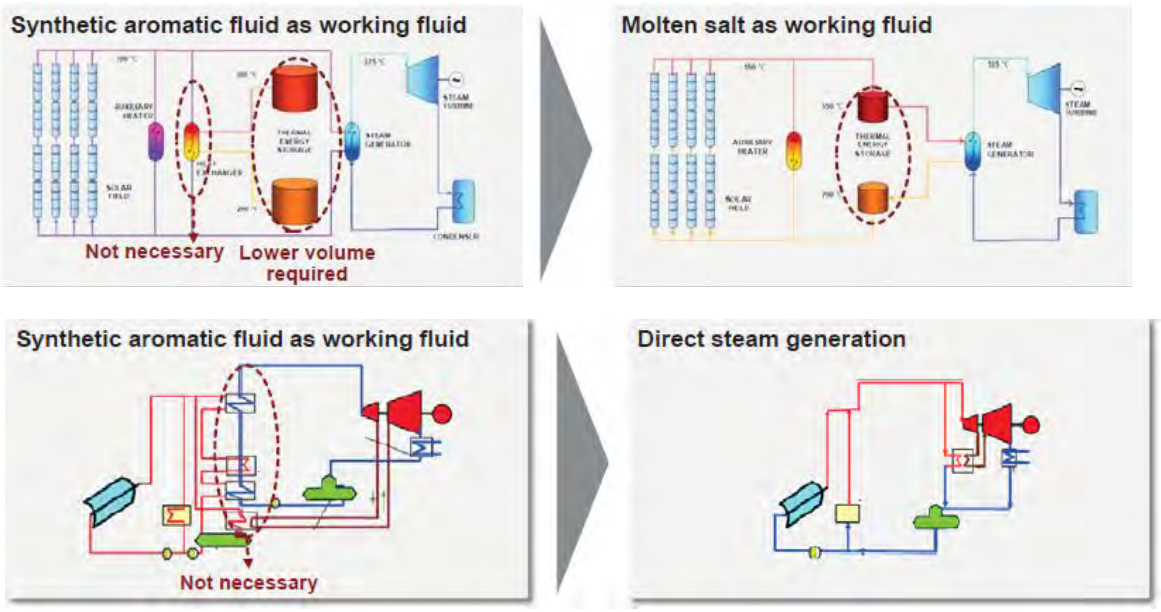

Figure 2-10: heat transfer fluid and relative plant scheme; up, syntetic oil and molten salts, down, water. (A.T. Kerney GmbH, 2010)

Finally, also air has been employed as working fluid, as Airlight Energy developed a large size collector that warms pressurized air till 650°C. The most interesting features of this small plant are the innovative HTF, the reflecting surface (thin polyester film) and thermal storage based on silica gravel.

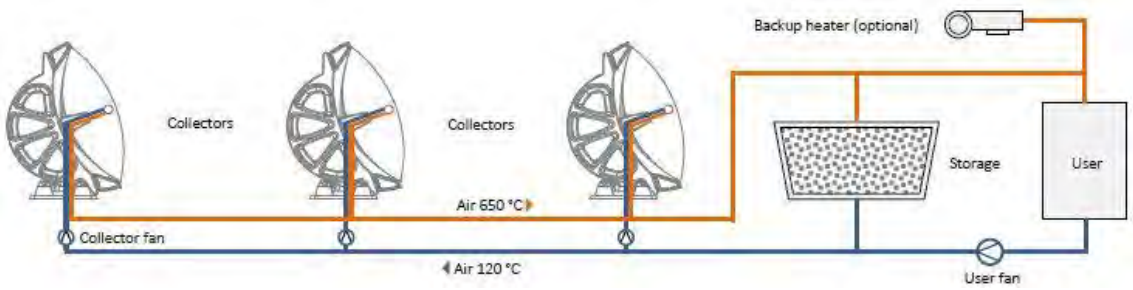

Figure 2-11: Airlight parabolic trough (Ailight Energy, s.d.)

The typical PTC receiver tube is composed of an inner steel pipe surrounded by a glass tube to reduce convective heat losses from the hot steel pipe. The steel pipe has a selective high-absorptivity (>90%), low-emissivity (<30% in the infrared) coating that reduces radiative thermal losses. Receiver tubes with glass vacuum tubes and glass pipes with an antireflective coating achieve higher PTC thermal efficiency and better annual performance, especially at higher operating temperatures (Romero-Alvarez M., 2007).

PT is the most mature CSP technology, accounting for more than 80% of the currently installed CSP capacity, thanks to the offered modularity, fossil back-up or hybridization and, not last, operative and financial experience cumulated,.

2.2.2. Linear Fresnel Reflectors

Large reflectors can be simulated by small reflector elements distributed over some suitable (ground or roof) surface, thus allowing systems built up by small element. Many long-row segments focus collectively on an elevated long linear tower receiver running parallel to the reflector rotational axis; in every instant considered, each row has a unique orientation because of the relative target position.
The linear receiver presents a CPC (compound parabolic concentrator), in order to optimize interception factor.

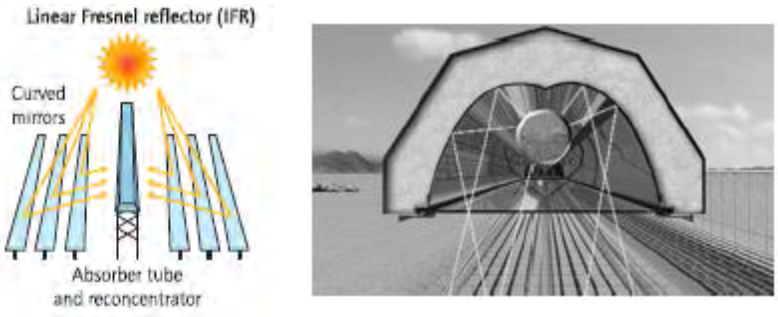

Figure 2-12: LFR scheme (International Energy Agency, 2010) and CPC secondary reflector (Mills, 2012)

In the receiver tube, water usually flows as HTF, this mainly because LF is the less efficient system of the four reported; putting a heat exchanger would just worsen the overall efficiency. Anyway the very advantage of this system is the low capital cost required: each reflective unit has the same dimensions and their disposition permits the use of almost flat glass mirror elements. Coupling these good characteristics together with the very good land usage and the easy cleaning operation we may see how the simple design sets off the poor performances.

2.2.3. Parabolic Dish Concentrator

A parabolic dish concentrator is a point-focus concentrator that collects sunlight on a receiver by means of two-axis tracking system. In the focal point we usually find a Stirling engine or, in some research applications, a micro-turbine.
The ideal shape of the reflecting surface (paraboloid) enables a really high concentration ratio to be achieved (>1000) and optimal design for cavity receivers that minimizes convection heat losses; due to the high flux and temperatures (>750°C) at the receiver, those systems have proved peak conversion efficiencies of above 30%, setting a record for CSP technology. The size of the dish is determined by the power output desired at maximum insolation levels (about 1 kW/m^2) as well as the collector and power-conversion efficiencies. A 5 kWe dish/Stirling system requires a dish of approximately 5,5 m in diameter and a 25 kWe one of about 10 m.

Figure 2-13: Eurodish system (Romero-Alvarez M., 2007)

These concentrators can be divided into groups according to reflecting surface shape and material, tracking method and power unit, but all the proposed systems are linked by factors like modularity and that they do not need any water cooling system for exhaust heat. On the other hand there isn't any significant chance to store thermal energy, whereas hybridization with a natural-gas fired micro-turbine is under development.
Nowadays the best application seems in distributed power generation, better for stand-alone systems; unfortunately, even if technical feasibility has been already demonstrated, the road to economic maturity is still long, above all if coupled with substantial maintenance due to mechanical failures and HTF leaks (in Stirling engines hydrogen or helium).
From a merely financial point of view, all the aforementioned characteristics and the specific cost of about 10000 $/kW (Romero-Alvarez M., 2007) drive this technology out of market, especially because lacking of storage and hybridization make them competitors of PV systems, whose specific cost is roughly below 2000 $/kW (IRENA, 2012).

2.2.4. Central Receiver System

This system will be explained in detail in the next chapter, as it's the central subject of this work.

2.2.5 Energy Storage

Although solar energy is a variable source, CSP can be easily coupled with thermal energy storage: when the incoming radiation exceeds the nominal one, a fraction of energy is accumulated to be used during cloudy periods, or even during night. That makes the plant more cost effective, even if a greater capital cost has to be taken into account.
Thermal energy storage (TES) system consists of three parts: storage medium, heat transfer mechanism and containment system. The form in which energy is stored spaces from heat, sensible or latent, to reversible chemical reactions; system dynamics and longevity is assured by a number of requirements (Kuravi, et al., 2013):

1) High energy density in the storage material

2) Good heat transfer between the heat transfer fluid (HTF) and the storage medium

3) Mechanical and chemical stability of the storage material

4) Chemical compatibility between HTF, heat exchanger, and storage medium

5) Complete reversibility for a large number of charging/discharging cycles

6) Low thermal losses

7) Low cost

8) Low environmental impact.

Furthermore, the storage system must meet some criteria during the design phase, like nominal temperature and specific enthalpy drop in the load, maximum load, operational strategy, and integration into the plant. Such criteria actually depend on the function that the system has to accomplish. A small storage unit suits buffering and helps mitigate short fluctuations in solar insolation during cloudy transient. A second case is when peak power demand do not coincide with peak solar insolation, so that the TES collects energy during off-peak hours to discharge it when it's needed; alternatively, cumulated energy may extend the nominal operation mode even when solar radiation starts to be less intense. Finally, a large TES can improve substantially the capacity factor of the plant, if it collects enough energy to work for 24h, at least during the months which present the highest level of radiation over the year. This is why a TES system is usually defined in terms of equivalent hours at nominal power.

Fundamental subcomponent of any thermal energy storage system is the medium chosen to store energy, which determines the storage type as well. Sensible heat storage system achieves its aim by raising the temperature of a medium, without change phase; the heat stored depends strongly on heat capacity and thermal diffusivity. A number of research efforts are focused on latent heat storage, in which materials change phase at a temperature that falls within the upper and the lower limit of the solar field; due to its low volumetric expansion, the solid-liquid transition is typically used. Latent heat storage is almost a isothermal process and, being governed by the enthalpy of change phase, it may enable a smaller, lower-cost solution. The last, but not least, TES system is the thermochemical one: it can potentially store more energy than sensible or latent heat systems because of the heat of reaction; another advantage is that the storage medium is dissociated from the temperature range of the CSP system, so it can be kept indefinitely at ambient temperature, without thermal losses.

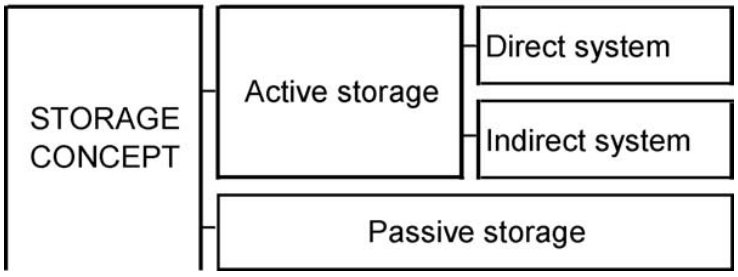

Figure 2-14: classification of different storage systems according the storage (Gil, et al., 2010)

TES concepts can be classified as active or passive systems. In an active system, the storage medium itself circulates through a heat exchanger where forced convection is the dominant phenomenon. If the storage medium is used also as HTF, the system is referred to as direct-active, otherwise it's called indirect.

The so-called "two-tank system" of figure 2-10 is a good example of direct (or indirect) active system: the heat is stored in a hot tank filled with molten salts, while the "cold" tank, is kept at a lower temperature by the HTF, before it absorbs concentrated radiation. Because of the temperature range and the affordable cost, mixture of nitrates took the lead among suitable materials; their outcome anyway is the high freezing point, which entails an auxiliary heating system. When this system is indirect, an intermediate heat exchanger must be installed, thus worsening the efficiency of the whole system. Currently this is the most common concept for storing thermal energy among CSP plants, from Andasol-1 to Gemasolar, benchmarks for parabolic trough and tower plants respectively. In Gemasolar case, the storage capacity reaches 15 equivalent hours, a record for CSP world.
The thermocline tank is another indirect active storage system, but with one single tank; its main advantage is clearly a cost reduction. Hot and cold fluids are hosted in the same containment, but are separated because of different densities (stratification). A filler material is inserted to aid in maintaining the gradient, while, at the same time, reduces natural convection between liquids. Anyway this represents the actual limitation factor for this concept.
For the CSP systems generating steam directly, a steam accumulator is an interesting option. A pressurized tank is filled by saturated steam and water; the discharging phase takes place by removing the steam, thus reducing the pressure. Depending on the pressure drop, a certain amount of energy is extracted. Although the system is pressurized, steam has low volumetric energy density, whereas a large pressurized structure has to face mechanical problems. This concept has been employed in the PS10 plant, helping to overcome cloudy transient with its 45 minutes of equivalent operation.

When the HTF passes through the storage material only for charging and discharging, the system is called "passive". It may employ solids such as rock, sand or concrete for sensible heat storage, or phase change materials (PCM). Usually pipes are incorporated in the storage material. Although very promising and cost-competitive, these systems are still under research or prototypal phase, and a satisfactory PCM hasn't been found yet.

Finally, chemical energy storage is supposed to absorb excess heat in an endothermic reaction. Feasibility of CH4 reforming has been widely demonstrated and dissociation of ammonia (NH3) has been investigated as well.

A small list of TES systems and their relative plants is reported below.

Table 2-1: four TES systems in commercial plants (Kuravi, et al., 2013)

Project	Type	Storage medium	T_{cold} (°C)	T_{hot} (°C)	Storage concept	Plant capacity	Storage capacity
Andasol-1, Granada, Spain	PT	molten salts	292	386	2-tank indirect	50 MWe	7.5h/1010 MWht
Archimede, Syracuse,	PT	molten salts	290	550	2-tank direct	5 MWe	8h/100 MWht

Italy							
PS-10, Seville, Spain	CRS	pressurized water	240	260	steam accumulator	11 MWe	50min/20 MWht
Gemasolar, Seville, Spain	CRS	molten salts	292	565	2-tank direct	17 MWe	15h/ 670MWht

2.2.6 Hybridization

In addition to thermal energy storage, another way to overcome the intermittent nature of solar source is hybridization with fossil fuels. In contrast to solar-only CSP plants, a hybrid plant can use the existing infrastructure of a conventional power station, alleviate fuel consumption and the connected CO_2 emissions; furthermore it increases revenue and experience, both technical and financial, in order to accelerate CSP penetration in current energy market. Finally, it's worth reminding that the countries which have the highest solar radiation level are commonly sites where fossil resources are extracted and processed.

A number of different approaches may realize the hybridization.
In many parabolic trough plants that run a Rankine cycle, from USA to Spain, backup gas-fired boiler are used when the temperature of the steam is below the nominal required by the steam turbines or during start-up phase. In Spain, this is allowed by the feed-in regulation, although it limits the annual share of fossil energy at 15% of the total energy produced. Solar hybridization with coal-fired plants is suitable for countries that have plenty of solar and coal resources, like China and Australia. The solar heat can work in parallel with the boiler or feedwater heaters, thus becoming attractive for repowering small-medium power plants (<300MWe).
ISCC, acronym for Integrated Solar Combined Cycle, plants are gas-fired combined cycle plants where concentrated solar heat is added to produce saturated o superheated steam in the heat recovery steam generator. Their greatest advantage is that a CSP subsystem enters in high-efficiency energy transformation process, but usually the solar share on annual energy is low, about 4÷15%. An example is represented by Hassi R'mel case, where a 150MWe-ISCC plant achieves a solar fraction reaches equal to 17% thanks to a 25 MW parabolic trough field (180000 m^2 of reflective surface).
Finally, an advanced integration between natural gas and CSP was realized in the SOLGATE and in the more recent SOLUGAS projects: solar heat is introduced to preheat the air discharged by the compressor of a Brayton cycle, thus lowering the fraction of fuel that has to be introduced in the combustion chamber (Buck, et al., 2002), (Quero, et al., 2013).

3 Central Receiver System

A typical central receiver system (CRS) consist in an array of two-axis tracking mirrors (heliostats) that reflect the direct incoming radiation on a central target, that can be a receiver or a secondary reflector.
It's a point-focus system and allows the collection of large amount of solar radiation without dealing with distributed thermal losses and HTF pressure drops as in parabolic trough collectors.
The heliostat field is nothing more than a Fresnel-type concentrator: since all heliostats are situated in the same plane they don't approximate one single parabola but each individual heliostat approximates a segment of a separate parabola (Pitz-Paal, 2007).It becomes necessary to space the mirrors, in order to keep high the amount of solar radiation focused even at low sun elevation, when the reciprocal shading and blocking effect between the heliostats would imply unacceptable reflection losses. The reason why the achievable concentration ratio of such a system (500÷1000) is lower than that of parabolic dish systems (1000÷5000) is that a CRS is an off-axis focusing system, as there will be always an average cosine factor different from zero at every time.

Due to the huge space required and the very high temperatures achievable (more than 1000°C), this concept appears as one of the most promising for electricity generation and thermo-chemical conversion of fossil fuels, while thermal storage demonstrated the possibility of 24/24 operation recently. Solar-to-electric conversion efficiency can reach high values because of the combination of these two factors, thus opening favorable scenarios for cost reduction.

The history of this kind of concentrating solar system dates back to the middle 80's, when several projects across Europe, USA, URSS and Japan started to consider this new form of exploiting solar energy, especially because of 1974 oil crisis. The "Sun rush" ended more or less at the beginning of the 90's but the American pilot plant Solar One, later converted in Solar Two, demonstrate the feasibility of such plant; in addition it set the path to Gemasolar (Solar Tres), that already reached the full 24h of operation thanks to the molten salt technology explored with the previous concept.

The list below remembers the central receiver solar thermal pilot plants in the 20th century (Behar, et al., 2013):

Table 3-1: central receiver pilot plants

Project acronym	Capacity MW	Country	Starting year
SSPS	0.5	Spain	1981
TSA	1	Spain	1993
CESA-1	1	Spain	1983
Solar one	10	USA	1982
MSEE/Cat B	1	USA	1984
Solar Two	10	USA	1996
THEMIS	2.5	France	1984
EURELIOS	1	Italy	1981
SUNSHINE	1	Japan	1981
SPP-5	5	Russia	1986

A CRS is made up of several subsystems:

- Heliostat field: the collector system of this technology.
- Receiver: this element is assigned to absorb the concentrated radiation energy and to transfer it to the HTF.
- Heat storage system: improves plant inertia, minimizing transient effects like cloud passages; the hours of equivalent operation define if the plant works as peak, intermediate or base load.
- Fossil fuel backup or hybridization type: a more stable output can require fuel contribution, especially for plant start-up; another option is to integrate the system in a conventional fossil power plant.
- Power block: it includes steam generator and turbine-alternator if Rankine cycle is the selected power process, or compressor-support combustion chamber-turbine when the CRS is coupled with a Brayton cycle.
- Master control, auxiliary systems and condenser, if needed.

Each point of the list presents a series of different alternatives that it's hard to find a standard system configuration, even more reminding the recent commercial stage.

State-of-art-review for CRS follows, where is underlined the relevant role played above all by the heat transfer medium, and relative receiver, adopted.

3.1 Heliostat Field

The collector system is basically divided into two groups: North (in northern hemisphere) and surrounding, depending on the relative position of heliostat field layout and the tower. The key element is the heliostat, a reflecting device formed by a support structure, two tracking motors, and a reflective surface.

Currently, complex software packages draw the heliostat pattern, as each optimization methodology deals with several independent variables to achieve the highest yearly optical efficiency. A typical specialized software deals with different optical losses for each reflective element across a number of iterations; the final layout is selected combining field efficiency with techno-economic constraints.

Being that the central theme of this work, heliostat description, field design and a review of collector system layouts is the topic of the next chapter.

3.2 Heat Transfer Fluid and Receiver

As the heliostat field also the solar receiver is a critical component of a CRS. The heat transfer medium adopted is strictly connected with the receiver and vice versa. Since the 1980 decade, when research facilities dawned, many receiver concepts have been analyzed, but still no one has demonstrated its primacy.

A perfect receiver would mimic a black body, reducing radiative losses as much as possible, it should withstand high thermal fluxes (> 1MW/m^2), even during transients, and high concentration ratios; at the same time, it must not be too expensive. Of course such receiver does not exist, so thermal efficiency and durability are the key variables; consequently the choice of the appropriate receiver is made on techno-economic basis and solar field layout. From a geometric point of view, cavity receivers are separated from external receivers as the loss mechanism changes. In a cavity receiver, concentrated radiation enter through an aperture, which limits radiative and convective losses; on the other hand, it requires more precise heliostat tracking to overcome spillage losses and it's suitable only for North (or South in southern hemisphere) field layouts.

The advantage of the external receiver type with an absorber arrangement of 360° is that it allows concentrated solar radiation to impinge from all sides whereas the acceptance angle of the cavity type is limited to around 60 to 120°. In surrounding heliostat fields, sunlight is collected on an external tubular receiver and the strategy adopted to solve partially the problem is to paint the tubes with a selective coating.

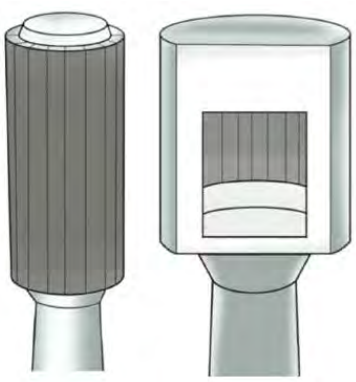

Figure 3-1: external and cavity tubular receivers (Ho & Iverson, 2014)

A further distinction regards the heat transfer fluid: water or molten salts or sodium flow in the tubular receiver, which presents a heat absorption method that has nothing to share with one projected to work with air (volumetric). Operating temperature and pressure are also determined by the HTF, so as the materials supporting mechanical and thermal stresses.

The subsequent graphic shows all the current classifications for a tower receiver:

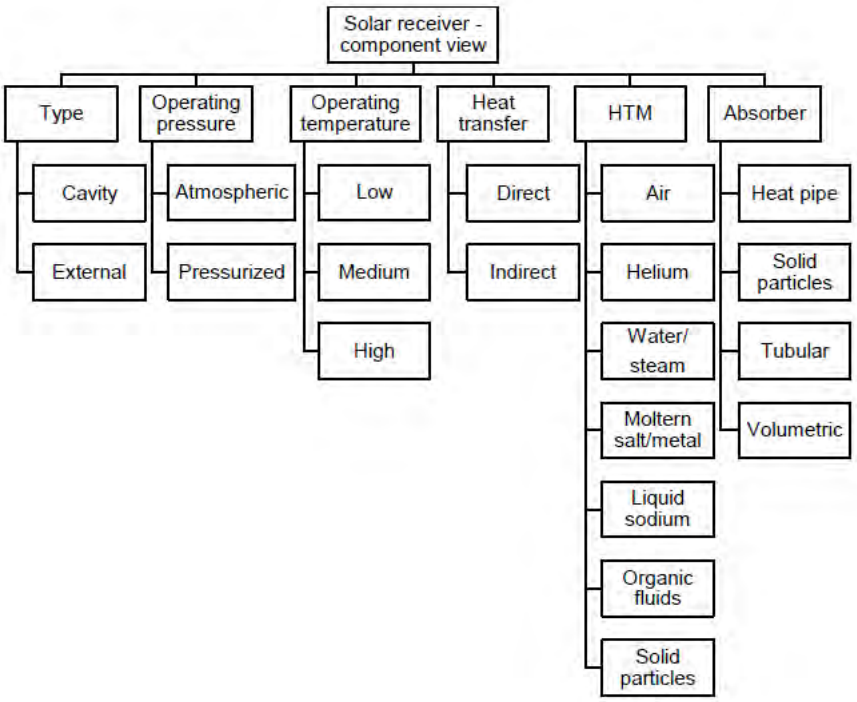

Figure 3-2: classification of solar tower receiver (Aichmayer, 2011)

Tubular receivers have been and are the most common since 1980: the heat transfer fluid enters in an array of darkened tubes and through multiple passes increases its enthalpy before being transported to storage and power block. Those systems have been tested and used with sodium, molten salts and for steam generation, for temperatures up to 500-600°C. Less experience has been cumulated in tubular gas receivers, employing air or supercritical CO_2 (Ho & Iverson, 2014).

In CRS like Solar One, PS10 and PS20, steam systems have been deployed; in PS10 facility, saturated steam at 40 bar and 250°C moves a turbine. Unfortunately problems such as the difficulty to rise up the steam pressure till the conventional level of about 13 MPa, the maximum flux limited to 0,6 MW/m^2 and the poor storage capability opened to new liquid HTF. The selection of nitrate salts and liquid sodium is due to their wider range of temperature and allowable flux. Molten salts can reach without drawbacks 540-565°C, undergoing 0,8 MW/m^2 fluxes, whereas liquid sodium enables even a flux higher than 1 MW/m^2; in addition both of them ease thermal storage because of the high heat capacity. The most significant limitations can be individuated, for molten salts, in decomposition at 600-630°C, high freezing point (220°C) and need for electric heating pipes; reactivity with oxygen, combined with leaking and corrosion, represents the hurdle of liquid sodium.

Solar Two receiver is still considered the technical reference for molten salt tubular external receivers. The 42-MW absorber consisted of a 6.2-m high and 5.1-m diameter cylinder, with 768 2-cm diameter tubes. Reported efficiency with no wind was 88% for 34 MW absorbed (86% with wind under 8 km/h). Peak concentrated solar flux was 800 kW/m^2 and average 400 kW/m^2.

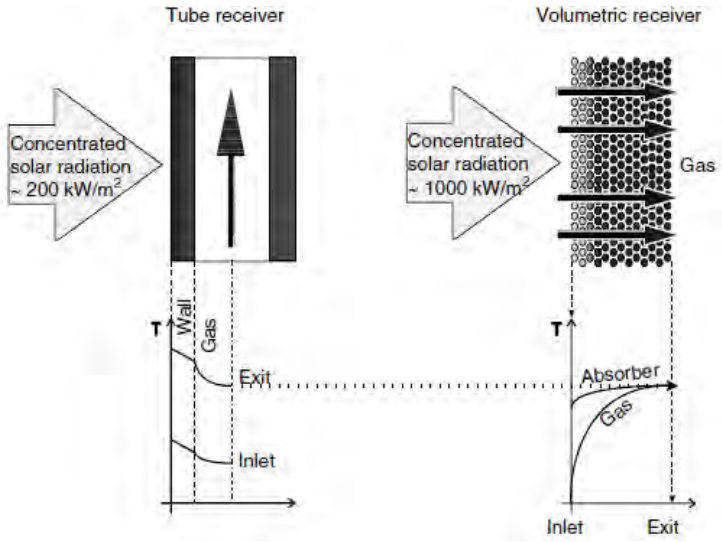

Figure 3-3: tubular and volumetric receiver schemes (Romero-Alvarez M., 2007)

In a volumetric receiver a porous material absorbs the concentrated solar radiation which is trapped inside the volume of the structure; then a fluid, like air, extracts the heat collected. The heat exchange exploits the volumetric effect, which means that the irradiated side of the absorber is at a lower temperature than the medium leaving the absorber.
The advantages of such a concept are many: air is a gas completely available in every site, it has no environmental and financial impact, it's non-toxic and doesn't change phase during operation. Due to the physical properties of air, there is no risk of decomposition at high temperatures and neither the need of trace heating; nevertheless it allows the use of 3÷5 hours of thermal storage in sand, rocks or concrete. Higher operative gas temperatures mean higher thermodynamic efficiency and pave the way for employing a Brayton cycle, thus abandoning the constraints of water as heat transfer fluid in a typical Rankine cycle and the condenser. Keeping in mind that CSP technology seems very appealing especially for the desert areas of the "Sun belt" countries; maybe this one appears the most interesting feature.
The challenges still unsolved concern absorber durability, mass flow stability and the specific cost of the receiver (Ávila-Marín, 2011).
The material that forms the porous structure sets the maximum outlet temperature of the gas; because of the extremely high radiative fluxes, metals and ceramics are accounted as the most appropriate. Metals can reach a maximum of 1000°C, SiSiC and SiC ceramics 1200°C and 1600°C respectively; above this limit alumina ceramics are compulsory, since their melting point is around the 2000°C.
Volumetric receivers are divided into two groups:

- Open-loop; the atmospheric air is heated up through a metal or ceramic volumetric receiver and then conveyed in a heat exchanger. The design of an open-loop receiver system may include an air return system that would improve receiver efficiency by using the cold air flow leaving the steam generator for two purposes: to cool the receiver support structure and to reuse the enthalpy of the return air. This was the design of the Phoebus-TSA project, where air flowing through a metallic absorber and a heat recovery steam generator fed a Rankine cycle. The 2,5 MWt air-cooled receiver heated up air till 700°C, producing steam at 480-540°C and 35-150 bar and reaching a mean thermal efficiency of 65% (Ho & Iverson, 2014).

- Closed-loop; concentrated solar energy impinges on a volumetric receiver where a quartz window is mounted in order to reduce convective and radiative losses. Such concept seems very promising as it would fully exploit the potential of the solar/Combined-Cycle combination, preheating the compressor outlet air before it enters the combustor of the gas turbine (Ávila-Marín, 2011). REFOS project, coordinated by DLR and PSA, led to a modular windowed volumetric receiver able to work at 1000°C and 15bar. Thermal efficiency of a 350kW with metallic absorber resulted between 63% and 75%. In addition, closed-loop volumetric receivers can be easily adapted to thermochemical processes, like methane steam reforming.

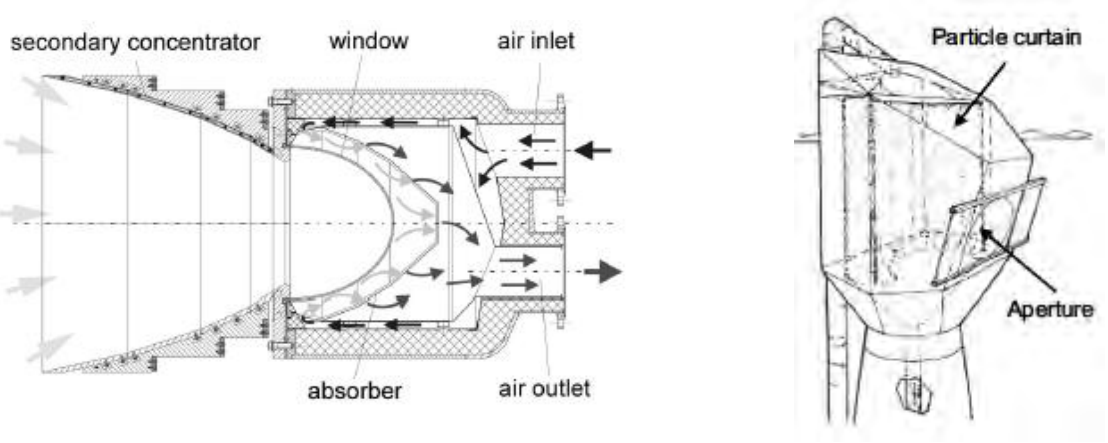

Figure 3-4: REFOS receiver module (Buck, et al., 2002) on the left, particle receiver (Ho & Iverson, 2014) on the right

The last type of directly irradiated receiver is particle receiver. In this case falling solid particles work as heat absorber and storage medium, thus avoiding the installation of a heat exchanger; as the particles are sand-like ceramics they can stand high fluxes, they are pumped from the cold storage tank at 360°C to the receiver. The outlet temperature is about 1000°C, and is able to heat a pressurized air flow till 995°C before it enters in the combustion chamber of a gas turbine cycle. Other application is under development at the US Department of Energy (DOE), where a falling particle receiver drives a water-splitting thermo-chemical cycle for hydrogen generation.

3.3 Power Conversion System

In the power conversion unit, thermal energy conveyed by the HTF is converted in electricity by a thermodynamic cycle. Nowadays Brayton and Rankine cycles have been implemented, but the goal for the near future is to experiment a solar combined cycle configuration in order to improve system efficiency.

Concept studies and commercial systems mainly differ in the way the two cycles are structured:

- Atmospheric air cycles
- Pressurized air cycles

- Direct steam cycles
- Molten salt cycles

As aforementioned, air as working fluid entails unquestionable advantages and the easiest way to capitalize on it is heating up an inlet flow in a volumetric atmospheric receiver. During the PS10 development, a parallel conceptual study was carried on to analyze an open-air system, especially because of the various experiments that took place in PSA during the previous years.
In Figure 3-6, the left blower regulates air through the receiver and the right blower to the steam generator. Projected receiver inlet temperature was 110°C and outlet 680°C. The hot air ducts are thermally insulated on the inside, permitting the use of lower-cost carbon steel for the ducts. Because of this inner insulation, the air speed may not exceed 33 m/s. Heat storage was not a high technical risk, being well developed for waste heat recovery in blast furnaces and other industries, like cement or textiles; concrete or sands could be employed for operation-stability storage (30 min). Steam (10.73 kg/s) would have been produced at 460°C and 65bar. The steam was supposed to run a Rankine cycle whose output were 11MWe gross and 10MWe net with 30% efficiency (Romero, et al., 2000).

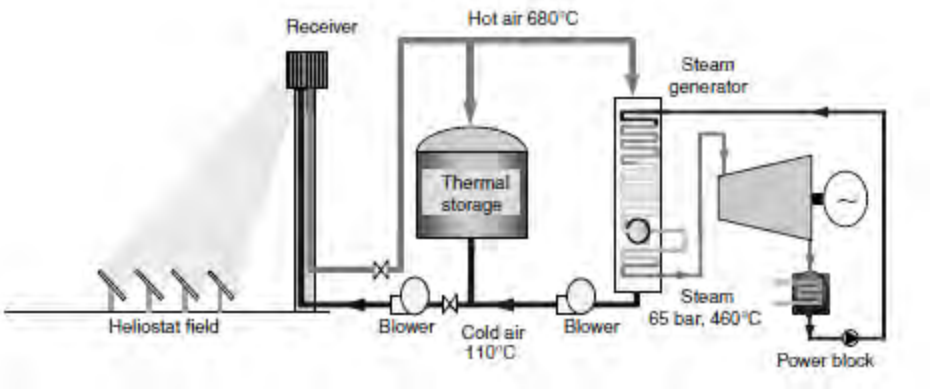

Figure 3-5: open-air volumetric receiver CRS concept (Romero-Alvarez M., 2007)

A second way is to adopt air as heat transfer and working fluid, installing a volumetric pressurized receiver; the aim of this configuration is clearly installing a power unit based on Brayton cycle, thus avoiding water consumption in the conversion system, dry condenser constraint and improving the specific power (per volume unit of the fluid). The high temperatures that air reaches in a volumetric receiver permit to modify and install a standard gas turbine. At least this is the conceptual base for the Solugas project built up in Seville. It consists in the first megawatt-scale demonstration of a solar-hybrid power system: pressurized air from turbine compressor is heated in the receiver, feeding the combustion chamber of a commercial Mercury TM 50 gas turbine modified to operate driven by solar energy. There, the air entering at 10bar and 800°C is heated further with natural gas to reach its nominal working temperature of 1150 °C.
The outlet enthalpy of the low-CO_2-concentration gas is enough for a Rankine bottoming cycle or cogeneration. During operation experience it has been demonstrated that the plant can be fully operative in 30 minutes, even if only 10 are needed when the gas turbine is working without solar integration.

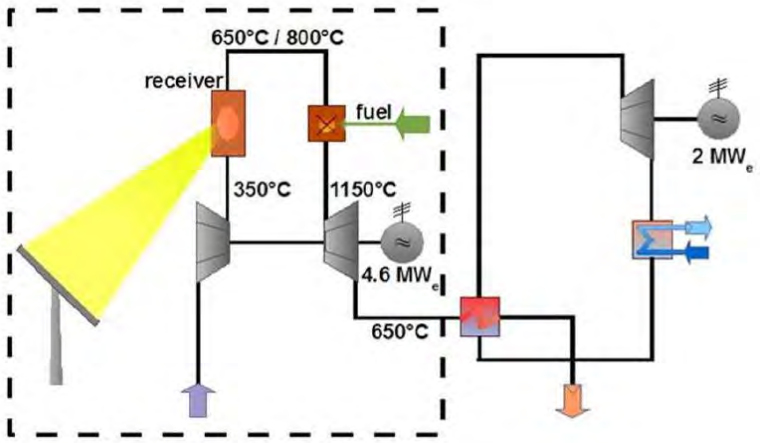

Figure 3-6: Solugas scheme (Quero, et al., 2013)

This system configuration appears extremely interesting; especially considering the experience developed with gas turbines and combined cycles all over the world. Moreover such solar system, i.e. solar hybrid tower plant in base-load operation, could be able to produce electricity at 7,3 €ct/kWh (Giuliano, et al., 2011). At this price, power generation would be competitive with a conventional (natural gas fired) combined cycle plant, whose LCOE is about 6 €ct/kWh.

Direct steam generation on the other side was adopted for the first commercial CRS in the world, the PS10 plant operative since 2007. The 11-MWe plant was designed to achieve an annual electricity production of 23GWh at an investment cost of less than 3500 €/kW. The project made use of available, well-proven technologies to produce saturated steam at 40bar and 250°C. The plant is a solar-only system equipped with saturated steam heat storage able to supply 50 min of plant operation at 50% load; it enables operation stability during transients like cloud passage, but it doesn't really improve the revenue of the plant. 624 heliostats (121m^2 each one), distributed in a north field configuration, focus sunlight onto a cavity receiver placed at the top of a 115m-high tower. Even if the steam turbine is working at low temperature, the nominal efficiency of 30.7% is relatively good. This efficiency is the result of optimized management of waste heat in the thermodynamic cycle. At the turbogenerator exit, the steam is sent to a water-cooled condenser, working at 0.06 bar. Out of the condenser steam is preheated with the turbine extractions. Afterwards, the steam from the first preheater is moved to a deaerator and is heated with steam from a different turbine extraction. A humidity separator is installed between the high- and low-pressure sections of the turbine to increase steam quality in the last stages of expansion. Then the third and final preheater with steam from the receiver preheats the steam once more. As a result, the water temperature is raised to about 245ºC and is sent to the receiver again. The combination of optical, receiver, and power block efficiencies leads to a total nominal efficiency at design point of 21.7%. Total annual efficiency decreases to 15.4%, including operational losses and outages. The LCOE of the PS10 plant is about 23 €ct/kWh.

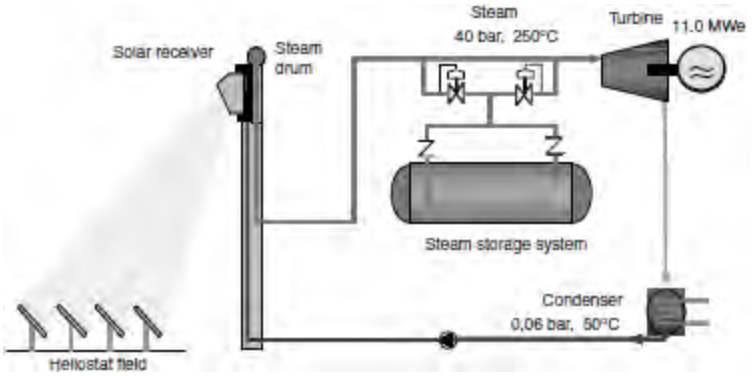

Figure 3-7: PS10 scheme (Romero-Alvarez M., 2007)

Less than a decade after the PS10, another milestone CRS was built close to Seville: located in Fuentes de Andalucía, Gemasolar is the first commercial-scale plant in the world applying central tower receiver and molten salt heat storage technology. Inspired by Solar Two experience, this plant consists of 2650 heliostats, 121m^2 each one, that concentrate solar radiation onto a 120MWt receiver mounted on a 140m-high tower. Molten salts (mixture of 60% sodium nitrate and 40% potassium nitrate) proceed from the cold storage tank at 290°C and are heated up till 565°C in the external tubular receiver; then they pass through the hot tank and finally are pumped to the power block. There, a solar steam generator produces superheated steam at 542°C and 105bar, which drives a 19,9MWe (gross) Siemens SST-600 two-cylinder reheat-steam turbine. A wet-cooling system takes the steam back to liquid. We can find Gemasolar in the public eye because of its molten salt thermal storage: thanks to the 15 equivalent hours of storage the plant can produce electrical power 24 hours a day for many months of the year, mainly in midsummer, reaching an annual capacity factor of 75%, typical of base-load plants. Even so, several efforts have to be done in order to reduce the LCOE, assessed at 0,24 €/kWh (Augsburger, 2013).

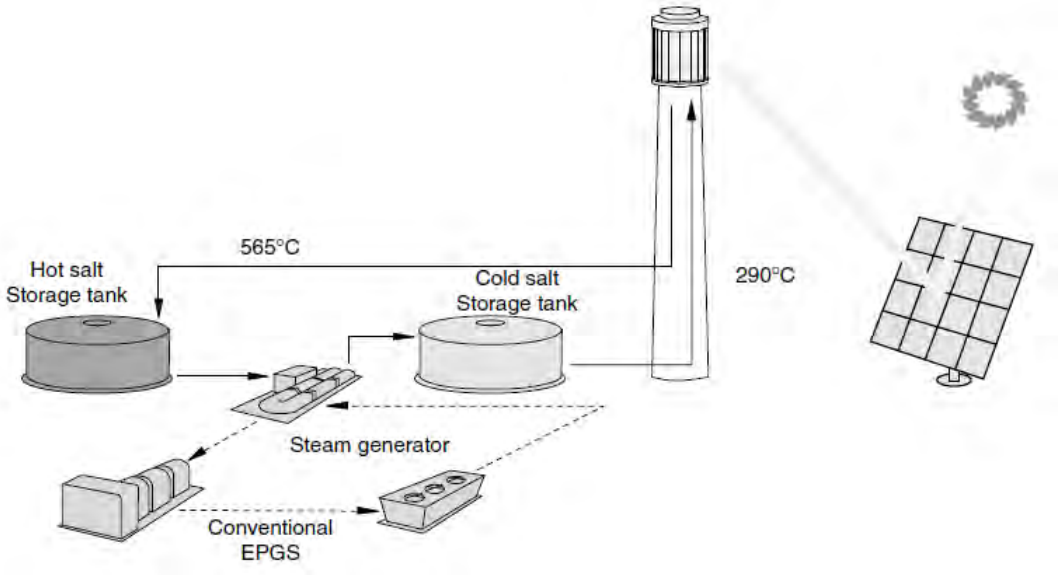

Figure 3-8: Solar Two scheme (Pacheco, et al., 2002)

3.4 Innovative Central Receiver System Concepts

In addition to the variable-geometry solar field studied herein, especially two alternative CRS might present a number of advantages compared to the classical configuration that sees one tower-top receiver.

In a beam-down CRS, a secondary mirror is inserted at the top of a tower, redirecting the concentrated solar radiation downward to a ground-level receiver. Such mirror has a hyperboloidal shape, where the upper focal point coincides with the aim point of the heliostat field, while the lower focal point stays at the entrance of the receiver concentrator. This system is already used in astronomy and is called Cassegranian system, although many important differences exist.
The convenience of the beams-down CRS lays in the fact that all major hardware are located at ground level: this eliminates long vertical piping, eases the installation of the receiver and maintenance operations, makes the tower lighter and less expensive. On the other hand one major drawback affects this concept. The elevated hyperbolic mirror reflects the image from a generic heliostat, but it turns out to be magnified according to the ratio between the image diameter at the second focus plane at the ground level and the image diameter at the aim point of the heliostat field (Segal & Epstein, 1999).
Because of the enlarged dimensions of the reflected image at the ground, the flux concentration drops, so a large compound parabolic secondary concentrator is required. Nevertheless, if this device seems to solve the low-concentration problem, the receiver has to face increased convection losses due to the large area of the apertures.

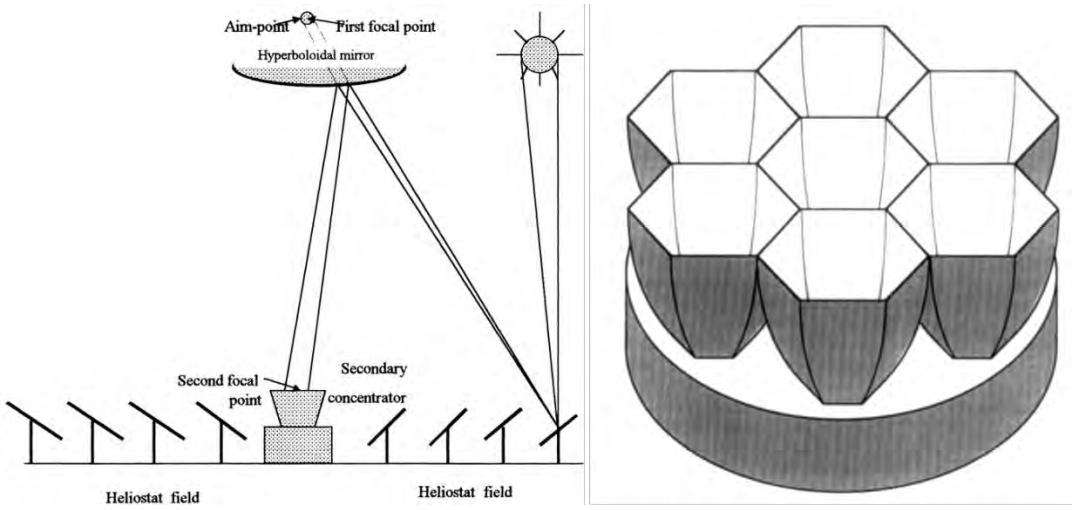

Figure 3-9: right, beam-down CRS scheme (Segal & Epstein, 1999); left, secondary concentrator detail (Yogev, et al., 1998)

The multi-tower solar array (MTSA) concept consists in several CRS standing close to each other that share a part of the entire heliostat field. It means that the mirror density is strongly increased, providing an efficient usage of ground area. Figure 3-11 illustrates the geometry of the collector system.
In order to waste the least amount of incoming radiation in the overlapped fields, the heliostats close to a tower have only one aiming point, whereas in the furthest regions from the receiver (in the middle of the square in mentioned figure), they could be alternately oriented to two, three or even four different targets. The strategy is effective in enhancing

cosine and blocking efficiency.
Such system turns out to be modular in the sense that many repetitive unit cells form the final pattern, but, as explained, it substantially differs from other modular approaches, where some different CRSs are simply "packed" together to work alone or in series. In this case, the surplus value consists in an active aiming strategy able to maximize the high land coverage. Another notable result is that a MTSA made up of small-size towers (< 10m) and heliostats (< $5m^2$) could be settled in an urban environment, over large parking or on big flat roofs (Schramek & Mills, 2003).

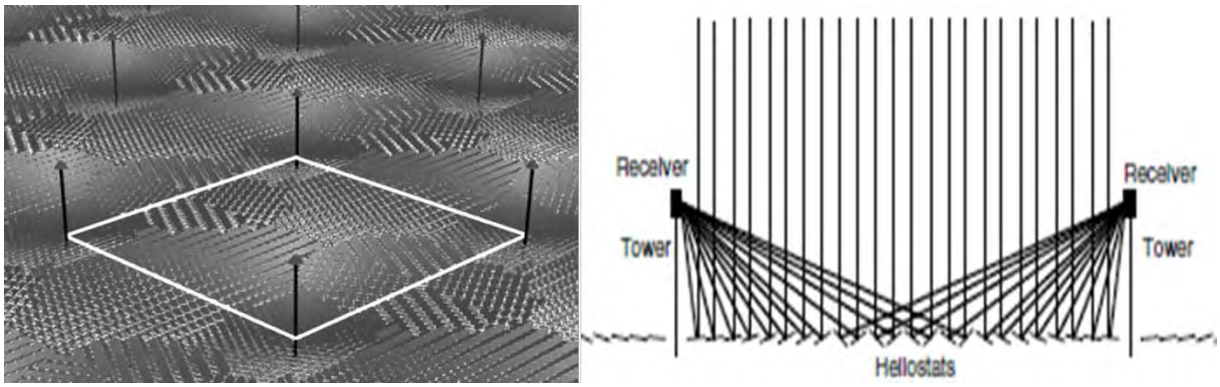

Figure 3-10: MTSA scheme (Schramek & Mills, 2003)

4 Heliostat Field

A heliostat field consists of a large number of tracking mirrors, called heliostats, each one approximating a segment of parabola. It's a critical subsystem in a CRS as its cost can reach 30÷50% of the total initial investment, whereas its share of energy and exergy losses is assessed at 30÷40% of the entire plant (IRENA, 2012).
In almost all the reports written during the last years, the need for increasing the field energy performance and, in parallel, reducing the cost of heliostats is particularly stressed. In a scenario in which both the target are met, the positive effect on the LCOE of a solar tower plant would be twice, because of capital cost reduction and increased collection of energy.

Current research is focusing on both this aspects, looking for new low-cost heliostat design, developing more and more precise computer tools for field simulation and optimization, and exploring innovative layouts.

4.1 Heliostat

A heliostat is defined as an apparatus containing a movable mirror, used to reflect sunlight in a fixed direction.

First developments date back to 1975, when research on CRS begun. In six years the pedestal-mounted heliostat appeared the winner concept, later implemented in the Solar One pilot plant. For second-generation studies, optimization and cost analysis showed that the best way to reduce cost was to increase heliostat size to $100m^2$ and benefit from economy of scale. Several heliostats were designed in those years: beyond the pedestal mounted one, many evaluations have been carried on for the bubble-enclosed membrane, ganged and carousel ones. McDonnell Douglas' and Martin Marietta's designs were judged the best on cost and performance bases; each Martin Marietta heliostat consisted of twelve glass mirror modules and the total reflective surface of $39m^2$ was mounted onto a torque-tube/truss structure. Current large glass/metal heliostat design is still an evolution of those first-generation concepts.
In the mid-80s a new design was investigated: after few years Sandia proposed a large circular stretched-membrane concept ($148m^2$), first with a polymer film glued to the metal membrane, then with a thin glass mirror. This design had easy assembly, as made up of very few parts, low-weight because of high stressed components and finally it provided an active focusing on the image thanks to a simple vacuum system able to adjust the focal length. Even if significantly cheaper, the polymer film suffered from the quick degradation due to UV damage.

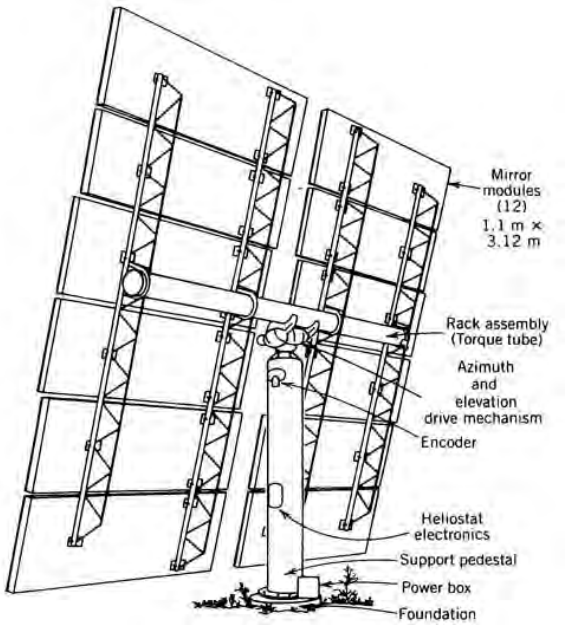

Figure 4-1: heliostat scheme (from http://www.powerfromthesun.net/Book/chapter10/)

Looking at such device we can distinguish the concrete foundation where the pedestal and the support structure are positioned. The reflective surface is usually the sum of several mirror facets, kept together by the steel frame, and is moved by a servomechanism that tracks continuously the Sun.

The basic arrangement of materials in a facet forms a sandwich-type structure in which are superimposed a transparent protective layer, a layer of reflective material, and a protective layer on the back side; everything is mounted onto the structural support material with an adhesive (Mar & Swearengen, 1981). Such heliostat is called glass/metal. Alternatives incorporate silvered polymer reflectors or thin film glass in order to reduce weight and cost. From a geometrical point of view, a further distinction regarding the reflective surface is possible. If the intensity of the reflected rays aimed to the target hinges on mirror reflectivity, the size of the image sent is determined by the position of the heliostat in the field, by the errors forming a degraded beam quality, and also by the shape of the mirror. A flat heliostat simply projects an image of the Sun from each point of its surface: taking into account the divergence of the reflected ray, if the heliostat is size is comparable or larger than the projected solar image, then the size of the reflected spot increases. This means the intensity is spread over a larger area, thus decreasing the concentration ratio. A possible solution is obtained by cutting the mirror in facets and curving each one to improve focusing. This operation, known as canting, is effective because each facet approximates a segment of a parabola that has the receiver in its focus. However, it should be remembered that due to cost reasons it is not possible to drive mirror facets individually. Once the facet is canted, its shape is fixed, whereas the heliostat changes azimuthal and elevation angles continuously. So when the angle of incidence is zero the size of the image at the receiver is minimum, but when the angle of incidence is greater than zero the canting leads to astigmatism, the dominant off-axis aberration (Igel & Hughes, 1979). Effectively the focal point is modified by the angle of incidence ϑ of the sunlight on the mirror, so in the transverse direction the focal length f is reduced by $\cos\vartheta$ and in the sagittal direction increased by $1/\cos\vartheta$, forming two line foci with a circle of least confusion between them near f (Vant-Hull, 2012). Several canting methods have been proposed:

- on-axis canting, i.e. ideal focusing alignment of all facets when both sun vector and target vector are perpendicular to heliostat mirror area;
- off-axis canting, i.e. ideal focusing alignment of all facets for a given sun vector defined by canting date and time;
- parabolic canting, i.e. alignment of all facets such that facet center normals are parallel to the corresponding surface normal of a paraboloid with central axis normal to the heliostat, located in the mirror area center and pointing toward the sun;
- target-aligned canting, i.e. ideal focusing alignment of all facets for a given sun vector (time instant), assuming spinning-elevation tracking. (Buck & Teufel, 2009)

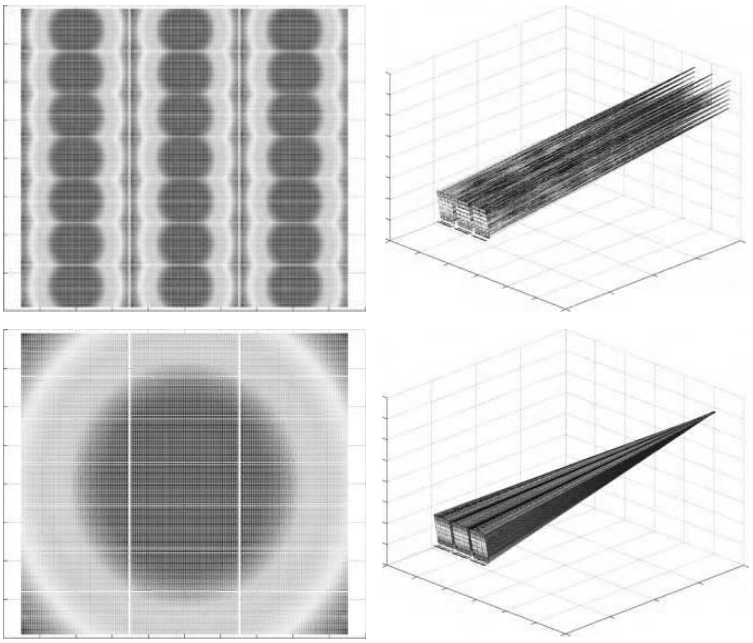

Figure 4-2: up, flat heliostat and correspondent ray-tracing, down, heliostat after canting and correspondent ray-tracing (Romero-Alvarez M., 2007)

There are two major sun-tracking methods widely implemented: Azimuth-Elevation (AE) and Spinning-Elevation (SE). In AE tracking method, the azimuth axis of the heliostat points towards the Zenith, while elevation axis is perpendicular to the first axis and tangent to the heliostat frame. In SE tracking method, one of the tracking axes of the heliostat points towards the target, namely spinning axis, in order to maintain the heliostat normal within the tangential plane; the elevation axis is perpendicular to the first one and tangent to the heliostat frame in order to adjust the heliostat normal within the tangential plane. This is made until the normal bisects the sun position vector and the target position vector (Chong & Tan, 2012). SE method consumes less power and reduces the radius of the solar image, but the AE method lasts as the reference, because of its lower cost.

The two-axis drive plays a key role in the correct plant operation, as it sets the alignment of the heliostat with respect to the aimpoint. A typical drive must be resistant enough to support the weight of the structure plus the wind loads; moreover, it must be rigid enough to avoid vibrations, enable extremely slow movements, with high reduction ratios, and at the same

time fast return to stow position if dangerous weather conditions occur. The positioning, computed by encoders, should be the most accurate as possible, thus ensuring a performant focus-defocus operation. Finally, other required characteristics are low-cost, resistance to outdoor conditions and long life time

The tracking system may be closed-loop or open-loop (active or passive respectively). A closed-loop tracking system uses photo-sensors to detect Sun's position and accordingly assign the collector's position. An open-loop system computes Sun's position through an algorithm. A closed-loop system gives the opportunity to automatically adjust heliostat position even during cloud transient with the help of the photo-sensors. On the opposite, a open-loop system can store Sun's position, and the relative collector one, for several years.

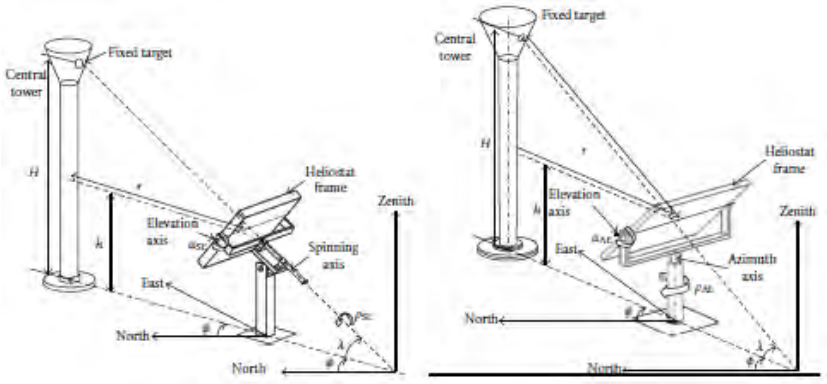

Figure 4-3: up, Spinning-Elevation (left) and Azimuth-Elevation (right) tracking methods (Chong & Tan, 2012); down, different size heliostats

Nowadays heliostat market is living an expansion period, as renewed attention is dedicated to CRS in the world. In the last years (2007-2013) the traditional dogma of bigger heliostat/lower cost has been challenged by several companies and research institutes, which resolved that optimal size could be even comprised in the range between 1.14 and 15 m^2.

Two sizes are currently dominating the market: large (> 115m^2) and small (< 20m^2). Among the first group the leader companies are the Spanish Abengoa and Sener. Abengoa installed its Sanlúcar 120 heliostat in PS10 and PS20 plants; on the other hand Sener supplied 2650 heliostats for Gemasolar plant.

Table 4-1: Sanlúcar 120 heliostat characteristics (Noone, et al., 2012)

Name and company	Sanlúcar 120, Abengoa Solar
Width	9.45 m
Length	12.84 m
Ratio of reflective surface	91.6 %
Reflectivity	0.95
Slope error	2.9 mrad
Materials	Glass/metal
Tracking error	1 mrad azimuthal, 1 mrad elevation
Facet canting	On-axis parabolic
Water usage for cleaning	0.275 l/ m^2

Smaller size was selected by BrightSource to cover more than 2600000m^2 of land for the Ivanpah Solar Electric Generating System. The 15m^2 heliostat is the result of a cost-reduction study that led to a fast and cheap fabrication: a single design has been chosen for all focal lengths and a new assembly line was patented. It's called FAST (Flexible Assembly Solar Technology) and its daily heliostat production is around 500, i.e. 1.7 heliostats per minute. In addition, the facility is on-site so far transportation is no longer needed to bring the mirrors to the plant. Reducing heliostat size and weight means also that concrete foundation can be saved; therefore plant construction is even faster, cheaper and less invasive for the environment.

The same idea was taken to the extreme by eSolar, the American company that bet on ultra-small heliostats to break down costs and ease installation. The 1.14 (or 2.25) m^2 mirrors are assembled in a uniform pattern of hexagonally packed heliostats; this allows a single design for the heliostat support structure to be used throughout the field (Schell, 2011), without ground penetration. The land usage is very high, thus offering a compact system that requires less space than others to achieve a fixed output.
Among the many advantages of this solution, it's worth pointing out that a small-heliostat field can be modular, offers better resistance to wind loads and doesn't need concrete foundations. Moreover maintenance is less expensive and the small size favors mass production.

The reason why so many efforts have been concentrated in heliostat R&D is that solar field represents more or less the 40÷50% of the total installed system cost (Kolb, et al., 2007). A cost-competitive CRS would be the turning key to slowly approach grid parity in some areas of the world, and this seems possible above all by reducing heliostat cost, without forgoing performance.

Usually the whole cost is allocated into three categories of costs:

1. Constant costs per unit area

2. Size-dependent costs
3. Fixed costs for components employed

Mirrors, for example, are part of the first category; in the second are taken into account structure, pedestal, drive units, while encoders or processers belong to the third cost entry as they don't rely on mirror size, neither on production rate (Blackmon, 2012). O&M is the only critical issue, but it could be seen as a parameter related to a reasonable percentage of the LCOE of the plant.
The reference for heliostat economic analysis is the famous "Heliostat Reduction Study" (Kolb, et al., 2007), where a Sandia research group drew up the cost breakdown for a 148m^2 ATS glass/metal heliostat, considering economy-of-scale factor as well.

Table 4-2: ATS heliostat cost allocation (Kolb, et al., 2007) revised by Blackmon (Blackmon, 2012)

Item	Cost/m^2 for 5000 h/y (2006 USD)	Cost/m^2 for 50000 h/y (2006 USD)
Gear drive	48.65	27.11
Mirror module	26.50	23.06
Torque tube assembly	11.85	10.78
Truss assembly	7.43	6.75
Cross bracing	4.04	3.68
Controls and cabling	2.09	1.90
Drive motors and limit switches	2.67	1.78
Pedestal	18.66	16.96
Fabrication and direct cost	121.89	92.02
Foundation	2.56	2.33
Field wiring	8.14	7.40
Field assembly and checkout	6.97	6.34
Installation cost	139.56	108.09
Overheat/profit (20%)	27.91	21.62
Total installed cost	167.47	129.71

A further refinement for this cost analysis was realized by Blackmon, who divided the cost items into the aforementioned categories:

Table 4-3: ATS heliostat cost allocation into three cost categories (Blackmon, 2012)

Item	Cost/m^2 for 5000 h/y (2006 USD)	Category 1 (2006 USD)	Category 2 (2006 USD)	Category 3 (2006 USD)
Mirror module	26.50	26.50		
Support structure	23.32		23.32	
Drive	48.65		48.65	
Drive electrical	2.67		1.33	1.34
Controls and cabling	2.09		1.33	1.34
Pedestal	18.66		18.66	
Field wiring	8.14	2.71	2.71	2.71
Foundation	2.56		2.56	
Field alignment/checkout	6.97	3.49		3.49
Total installed cost/area	139.56	32.70	98.28	8.58
Overhead/profit (20%)	27.91	6.54	19.66	1.72
Total installed price/area	167.47	39.24	117.93	10.29
Percentage on Total installed price/area	100%	23.4%	70.4%	6.1%

It should be underlined the share of the size dependent costs on the total costs. The 70.4% is attributed to the weight of loaded structure and mechanical hardware; the result makes sense, as the larger the heliostat is, the more it needs appropriate foundations, installation and mechanical resistance, to bear wind loads.
From the three cost categories we can get the idea that lies behind the small size heliostats. The size dependent costs can be considerably lowered, even if more wiring and a continuous steel structure is required. Furthermore, small heliostats improve the system cost of the plant with a given receiver, working at a given temperature: the image sent is smaller than the one that larger heliostats would send. The spillage is lower; the receiver would present a smaller area, thus radiative and convective losses would be lower as well.

4.1.1 Mobile Heliostat

In the Variable-Geometry Test Facility at the CTAER in Tabernas (Almería), the standard concept of heliostat has been challenged, due to the innovative features of this solar field. All existing tower plants work with ground-fixed heliostats and fixed receiver, but a variable-geometry field requires mobile elements.
Mobile heliostats, called also "heliomobiles", are arranged into concentric rails, where they move around the tower in an automated way to follow the apparent movement of the Sun during the day.
Each heliomobile is made up of 56 canted facets for a total gross area of 120m^2; the total width is 12.88m and the total length 9.485m. The ensemble of mirror modules is supported by a steel structure consisting in a torque tube, directly connected to the drive system, and several truss type beams. Until now, it seems that a heliomobile doesn't differ from a conventional heliostat, but looking to the pedestal, the reflector doesn't lean on a concrete

foundation, but on a mobile platform. The entire system is operated via wi-fi in remote control.
Control and power supply systems are other two innovations introduced in this test facility; in a traditional solar field, each heliostat communicates with the control system and receives power through wires. In a variable-geometry field, this would be impossible because of the dynamics of the reflectors, so electric supply comes from a power string that stands in front of each row.

Figure 4-4: heliomobile details at CTAER. Up left, mobile platform andwi-fi control unit; down left rest position and rail; right, heliomobile under testing, fed by the power string.

The dynamic tracking mode is new as well: an electric motor unit drives the reflector on the rail, while the braking mechanism is hydraulic. Even in this case, extremely high precision is required like a passive security system that must prevent collisions between heliomobiles. Each platform is equipped with a laser sensor and a reflector able to redirect the laser beam of the closer heliomobile back to its own sensor. In other words, when a heliomobile approaches another one, the sensor sends laser beams and once the security distance is reached, the beam intercepts the reflector of the second heliomobile. In the moment in which the beam goes back to the sensor, the distance limit is achieved and the movement is stopped.

The optical properties are given by the reflectivity and cleanliness, the slope error of the overall shape, and the tracking error. The reflectivity ρ is the reflectivity of the mirrors when they are clean, while the cleanliness factor is the share of reflected sunlight that is not absorbed or scattered by dirt deposits on mirror surface. The slope error includes the errors of facet curvature, mirror waviness, facet alignment (canting) and gravity effects. It is defined by

the standard deviation σ_{slope} of a Gaussian distribution, in [rad] around the axis of reflection. The tracking error includes computational errors such as the Sun position calculation and encoder bias. Hardware errors such as non-perpendicularity of elevation-to-azimuth axis and the azimuth-axis tilt of the drives. The standard deviation σ_{track} stands for these errors. A detailed description of the aforementioned errors is given during the explanation of the CRS optical losses.
The assumed properties of the heliomobile are reported in the table below.

Table 4-4: heliomobile properties

Width	12.88 m
Height	9.485 m
Pedestal	6 m
Reflectivity	0.95
Slope error	2.9 mrad
Tracking error	1 mrad in elevation, 1 mrad in azimuth

4.2 Heliostat Field Layout

In a CRS the heliostats are arranged in a field layout. A field can be characterized by two factors: the geometrical shape and its position with respect to the tower. Field layout is calculated with complex optimization algorithms, as they must deal with the trade-off between cost and efficiency, both strongly discontinuous functions.

4.2.1 North (South) vs Surrounding

This first category is used to distinguish the arrangement of the heliostats. In a North field configuration[1], heliostats are positioned only in the north side to reflect radiation to the southward direction at the aiming point; on the other hand, in a surrounding field the mirrors cover the land all around the tower.

The decision about which type of field should be more or less appropriate relies on latitude, on desired power level and the central receiver type. Clearly, polar fields are equipped with a cavity receiver; its design imposes the acceptance limit angle, which is a constraint in field optimization. This kind of receiver, indeed, limits thermal losses reducing the aperture area, thus approaching black body condition. The acceptance angle, seen by the receiver, is around 120-140 degrees.
A North field is preferred the more the latitude increases and the smaller the power is. For an equivalent power level, the last row of heliostats would be farther, degrading unacceptably the interception factor and softening the intensity of the reflected beams because of atmospheric attenuation.
As the latitude decreases from North Pole, the Sun will stay for more time during the year at higher elevations, not only in South, but also in West and East sides. Surrounding layout is chosen to take more advantage of this solar apparent movement. This kind of field must be

[1] South field in the southern hemisphere

coupled with an external receiver that allows a greater energy collection if compared to a cavity receiver.

Figure 4-5: left, PS10 north field (www.nrel.com); right, Gemasolar surrounding field (www.torresolenergy.com)

A north field configuration is widely adopted for research facilities, like the CESA 1 in Plataforma Solar de Almería, the Jülich Tower owned by DLR in Germany or the Sierra Sun Tower by eSolar in Lancaster, California.
Surrounding field is preferred for larger power plants, where the power at the receiver is considerably higher; examples are the Gemasolar plant in Seville (17,7MWe) and of the new Crescent Dunes Solar Energy Project in Tonapah, Nevada (110MWe).

4.2.2 Field Geometry

Heliostat fields can additionally be grouped according to their geometrical shape: grid, circular and spiral.

The grid layout is probably the most simple: heliostats are positioned in a N-S/W-E grid, aiming to the receiver. Normally the rows are staggered to limit the reciprocal shading and blocking effects between heliostats, and the distance between rows may increase as the distance from the tower increases as well.

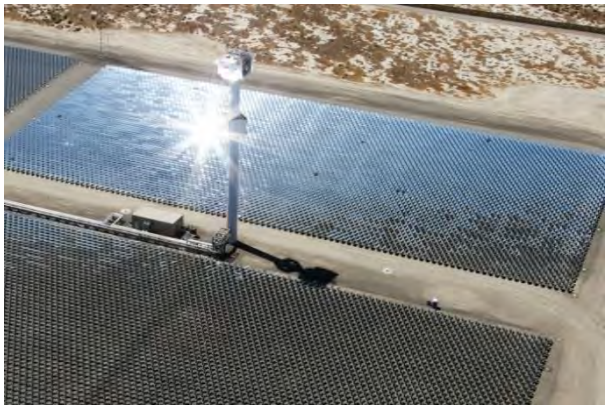

Figure 4-6: grid layout in the Sierra SunTower by eSolar (www.solaripedia.com)

In the other two layouts the tower stands in the geometrical center of the field.
In a circular field, mirrors are arranged along concentric circles and they are radially staggered, in order to minimize shading and blocking losses. When the circular grid is radially staggered, no heliostat is placed in front of another heliostat in adjacent rings along the path to the tower. The azimuthal spacing in a ring depends upon the divergence of the distribution axes that are determined by the azimuthal spacing in the previous ring. This, at least, is valid until the azimuthal spacing assumes values that lower too much the mirror density. Adding a new ring, it should be considered the possibility to start with a new azimuthal separation angle, in order to keep maximizing the mirror density (Siala & Elayeb, 2001). Normally, radial separation increases as the distance from the tower grows.

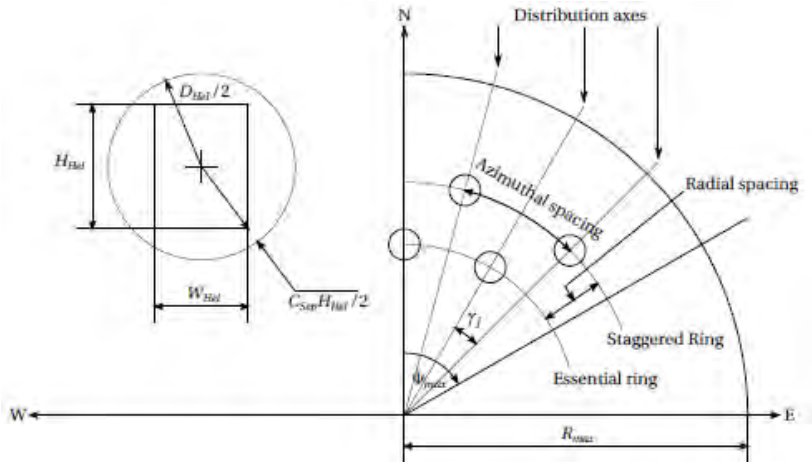

Figure 4-7: radially staggered circular layout (Siala & Elayeb, 2001)

Nowadays, all existing solar tower plants adopt the circular radially staggered field.

The last type of geometrical shape is the spiral. This new pattern was introduced in 2012 and still it has not been applied to any real solar field. Inspired by spiral patterns of the phyllotaxis disc, its advantage is that the mirror density function is continuous (Noone, et al., 2012). On the contrary, in a radially staggered pattern, the transition from high to low density is discontinuous, as explained before. This new characteristic allows maximizing the reflection of the incident sunlight where the efficiency of heliostats is higher, i.e. right in front of the tower. This arrangement entails that no heliostat shares with another one the same polar position from the tower; contrary to what one may think, the lack of symmetry hides favorable consequences in reducing shading and blocking interactions, even if the average mirror density in the field is higher than in an equivalent circular radially staggered field. The redesign-PS10 study showed that is possible to both reduce the land area of the plant and the number of heliostats for fixed energy collected. By reducing the capital cost of the plant at no additional costs, the effect is a reduction of LCOE (Noone, et al., 2012).

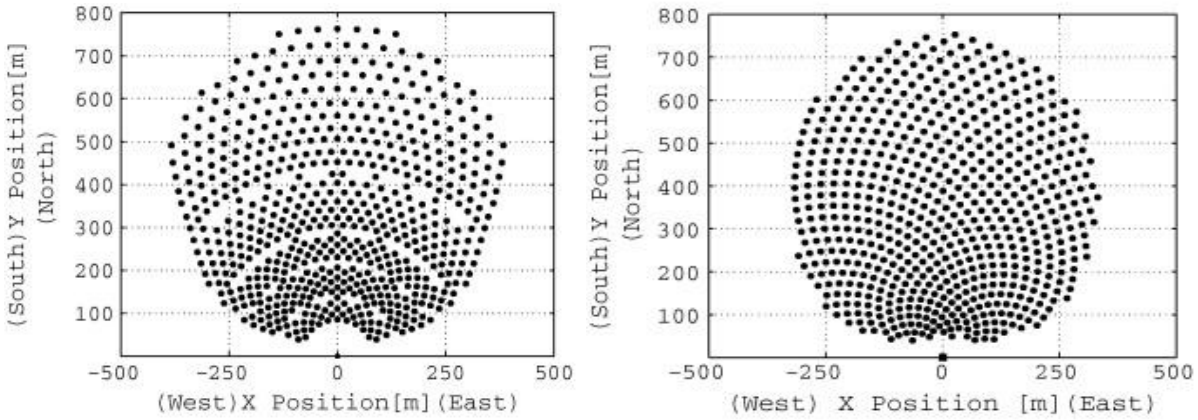

Figure 4-8: left, original PS10 heliostat field; right, redesigned PS10 heliostat field using phyllotaxis spiral heuristic (Noone, et al., 2012)

The variable-geometry solar field represents a new concept in CRS world. Its main characteristic is that mirrors adopt different positions throughout the whole day in order to redirect the direct solar radiation and to achieve the least optic loss possible. In other words, the cosine of the angle of incidence (the angle between the solar ray and the normal to the reflecting surface of the heliomobile) is kept as close to 1 as possible at each moment.
This is made possible by the dynamics of the heliomobiles, which change their location on the rails according to the sun position: during the morning the solar field will lies on the West side and rotates progressively towards the East side during the afternoon, at the same angular speed of the sun.
Coupling this system with a rotating receiver improves field efficiency even more, as the system eases a better interception of the whole reflected beam.

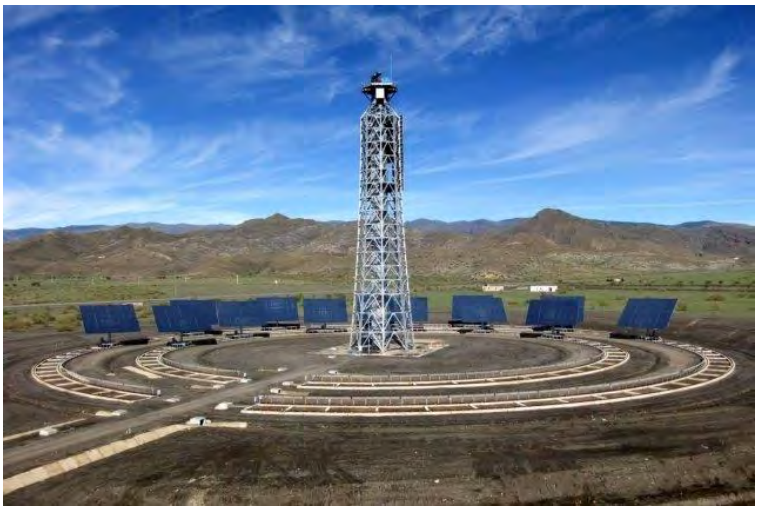

Figure 4-9 Variable-geometry solar field at CTAER (Centro Tecnológico Andaluz de Energías Renovables) (www.ctaer.com)

Currently only two rails have been placed, six mirrors in the first row, seven in the second one; but the complete field will count 119 heliomobiles so that the designed power conveyed to the receiver will be equal to 8MWt.

4.3 Heliostat Field Efficiency

The heliostat field efficiency, also called optical efficiency, is defined as the ratio between the concentrated radiation power directed within the boundaries of the receiver and the total incident power on the heliostat field:

$$\eta_{field} = \frac{\dot{Q}_{receiver}}{\dot{Q}_{solar,incident}} = \frac{\dot{Q}_{receiver}}{DNI\ n_h\ A_h}$$

where DNI is the beam (direct) normal irradiation, n_h is the total number of the heliostats in the field, and A_h the total area of the heliostat.
This efficiency is the product of several factors; the energy losses that affect every heliostat are distributed into reflectivity, cosine, shading and blocking and atmospheric attenuation losses. In addition, the optical errors associated to the reflective element lead to spillage losses.

<u>*Cosine losses*</u>: it's the major loss factor in CRS. In such system mirrors cannot always be aligned normal to the incident solar rays; the tracking mechanism rotates the heliostat plane so that its surface normal bisects the angle between the sun rays and the reflected ray, directed to the aim point. Because of Snell's Law of Reflection, the apparent area of the mirror, seen from the sun, is reduced by the cosine of one half of this angle.

$$\eta_{cos} = \cos\theta = \vec{s} \cdot \vec{n} = \vec{r} \cdot \vec{n}$$

where $\vec{s}$ is the solar vector, $\vec{n}$ the surface normal vector, $\vec{r}$ the reflected ray vector, and θ the angle between $\vec{s}$ and $\vec{n}$ (or $\vec{r}$ and $\vec{n}$).

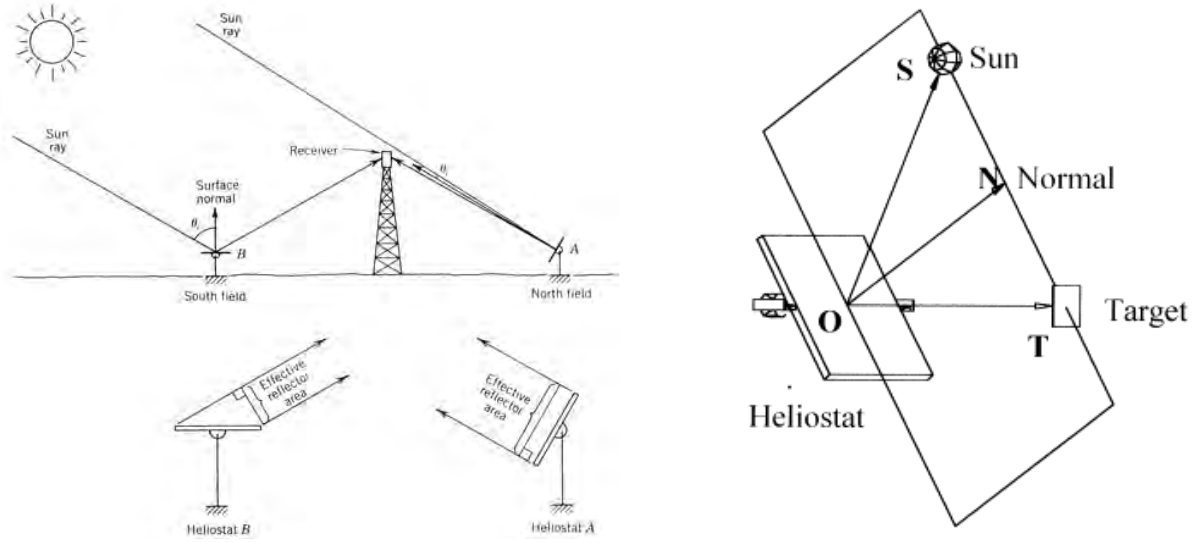

Figure 4-10: cosine losses for two different heliostats in the field (www.powerfromthesun.com) on the left, Snell's Law of Reflection on the right (Chen, et al., 2001)

The reduction of the projected area directly reduces the concentration ratio offered by the mirror.
In large solar fields heliostats are spread over long rows (straight or circular), so cosine losses are greater for that elements that are less aligned with the receiver and the Sun.

Throughout the day, the cosine efficiency evolves so that west-side heliostats roughly undergo minimal losses in the morning and maximal losses in the afternoon, and vice-versa is valid for east-side heliostats. This is the reason why a variable-geometry field can achieve a better collection of energy, when compared to a static one, either circular o spiral.

Shading and blocking losses: shading is a secondary geometrical loss, caused by the shadow casted by neighboring heliostats and/or the tower on the analyzed heliostat. The shading efficiency for the *i-th* heliostat is defined as:

$$\eta_{sh,i} = 1 - \frac{A_{shaded}}{A_h}$$

A_h is the total reflective surface and A_{shaded} is the shaded area. The energy loss is due to the amount of solar radiation that doesn't impinge on the shaded area.
As heliostat orientation varies during the day, its vertices and the shadow projected move as well, so the exact instantaneous evaluation of this efficiency for the whole field is computationally expensive, being thousands of heliostats in large solar tower plants. Shading happens when Sun is low in the sky and mainly affects the central part of the field, where the mirror density is higher.

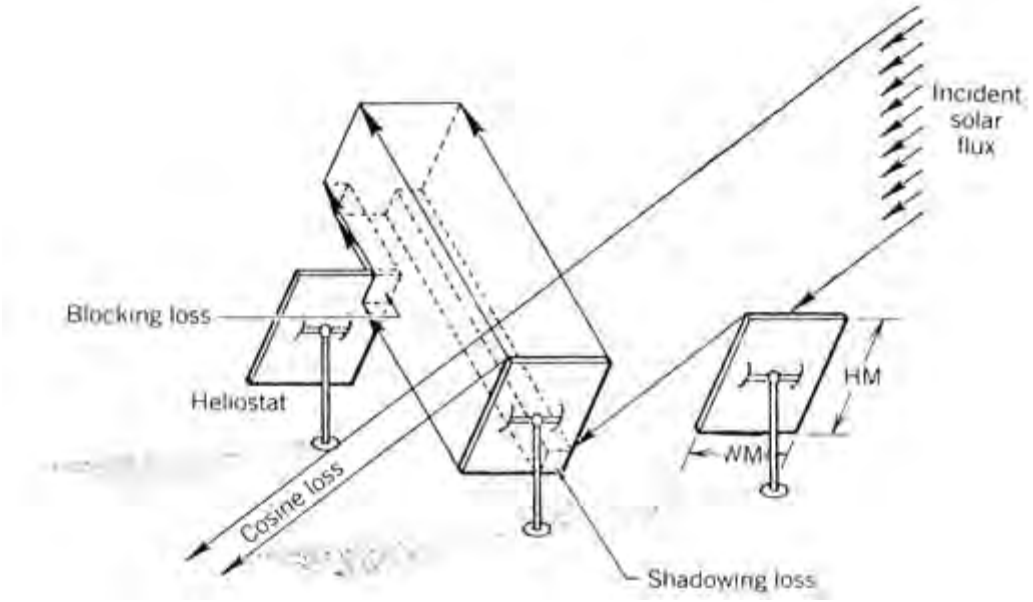

Figure 4-11: shading and blocking scheme (www.powerfromthesun.com)

Blocking occurs when the sun rays reflected from one heliostat toward the receiver are blocked by a neighbor on a front row. The blocking efficiency for the *i-th* heliostat is defined as:

$$\eta_{bl,i} = 1 - \frac{A_{blocked}}{A_{h,net}}$$

$A_{h,net}$ is the total reflective surface free from shading and $A_{blocked}$ is the blocked area. The energy loss is due to the amount of solar radiation that impinges on the backside of the front heliostat.

Unlike shadows, the beam formed by the rays reflected from one heliostat to the receiver tends to keep the same pattern regardless the time and the day considered. During field design there is the chance to limit blocking by choosing a defined azimuthal and radial spacing (Siala & Elayeb, 2001); however, as shading, blocking uses to arise in the zones with the highest mirror density.

The final shading and blocking efficiency for the heliostat *i* is so:

$$\eta_{s\&bl,i} = \eta_{sh,i}\,\eta_{bl,i}$$

Atmospheric attenuation losses: these losses account for the fraction of the reflected rays that suffers for attenuation along the path to the receiver. Not all the sunlight intensity that impinges on the heliostats arrives to the receiver, a part is scattered and absorbed by the atmosphere.
Scattering takes place over the whole spectral range and it consist in an elastic deviation of the photons from their trajectory; small particles, with a diameter smaller than the wavelength of the light, are responsible for this phenomenon. On the other side, gas molecules and aerosols, concentrated in the first 5-6 km from the ground, cause relatively high absorption of solar radiation.
Scattering and absorbing species along the path to the receiver determine a variable behavior of transmittance and radiance in the atmosphere. In order to evaluate the atmospheric attenuation, a spectral atmospheric transmission model is necessary; once it is obtained and verified, it becomes possible to estimate the attenuation percentage as function of the slant range and the visibility.

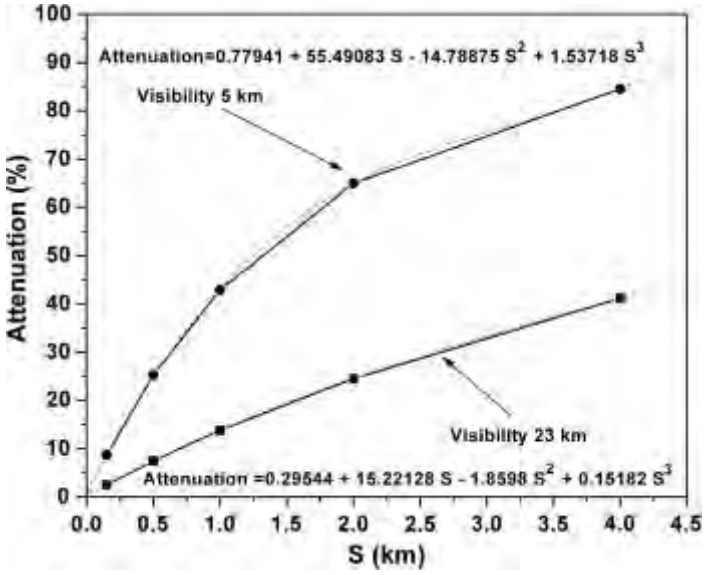

Figure 4-12: Attenuation loss of solar reflected irradiance on slant range distance at sea level and on top of 100m tower (MODTRAN) (Ballestrín & Marzo, 2012)

Atmospheric attenuation has a low impact on system performance, but only during clear-sky days; otherwise it can reach not negligible shares of the total losses, especially if the content of water vapor is high. Anyway, in the countries of the so-called "Sun belt", where CSP could free its potential, this eventuality is less frequent. Figure 4-12 shows how this kind of energy loss concerns above all the heliostats placed far away from the receiver.

Reflectivity losses: a generic mirror doesn't reflect the whole solar radiation that impinges on it, a part is absorbed and another transmitted. Heliostat reflectivity ρ is defined as the ratio between the reflected and the incoming solar radiation intensity and is a property of the material.

Reflectivity can vary from 97% for a well-protected front-surface silvered mirror to 95-96% for a second-surface mirror employing water-white glass, to 85-90% for thicker, high-iron glass (Vant-Hull, 2012).
Even if it may seem a high value, it should be considered that heliostats are continuously exposed to atmospheric conditions, which deteriorate the reflectivity at a 2%-per-month rate, mainly because of dust. Cleaning equipment and strategy must be accurately chosen in order to reach the desired trade-off between the costs of scrubbing and washing and the one associated to this kind of energy losses.

In a solar field made up of large heliostats, trucks carrying water and a brushing rig are required, while for small-size heliostats the procedure is easier and more automated (less costly).

Optical errors and spillage losses: the concentration ratio that a generic concentrator can achieve is limited by some optical errors due to imperfections ranging from the scale of microns up to centimeters. Another source of error is optical aberrations, which must be computed when a canted surface is analyzed.

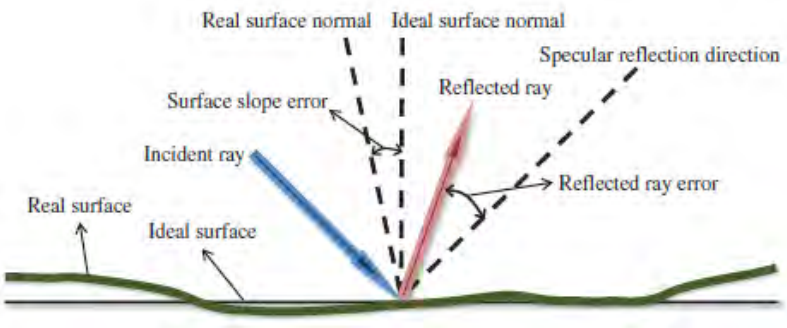

Figure 4-13: geometry of reflection according to the principles of Snell (Lee, 2014)

Snell's Law of Reflection states that for a specular surface the reflection angle equals the angle of incidence. In a real mirror with intrinsic and constructional errors, the reflected ray distribution can be described with "cone optics". Because the reflective surface area of typical solar concentrators is very large, it is often assumed that reflected ray errors statistically follow Gaussian distribution.
The sum of the variances of individual reflected ray errors results in a total variance σ^2, and the standard deviation (SD) σ, is regarded as a representative parameter of optical performance of solar concentrators (Lee, 2014).

Specularity error, σ_{spec}, is defined locally on a surface as the standard deviation of the distribution of reflected ray angles at a specified incident angle. It's a microscopic error intrinsic to the material and depends on the fabrication process; it can be measured at the laboratory with mirror samples.
Slope error (σ_{slope}) refers to errors in the surface normal vector that are caused by topographical deviations in a larger scale than the solar spectrum. The larger is this error, the

more the focal spot is spread and the lower concentration ratio is reached.
As the reflected surface is usually split into several facets, mechanical (wind, gravity) and thermal (air temperature) loads can modify the geometry of the heliostat structure, or some mirror elements may get an incorrect orientation. The shape error, σ_{shape}, represents these deviations.
The tracking system is a source of error as well. The heliostat is not always focusing correctly to its aim point and the resulting error is time-variant, thus tracking error σ_{track} is applied to both azimuthal and elevation drives.
Shape and tracking errors are categorized as macroscopic errors: they are characteristic of the concentrator and the construction process.
Since all the errors mentioned are modelled as a normal distribution of deviations, the overall optical error is their convolution and, for the central limit theorem, it follows Gaussian distribution as well:

$$\sigma^2_{concentrator} = \sigma^2_{spec} + \sigma^2_{slope} + \sigma^2_{shape} + \sigma^2_{track}$$

Moreover, Sun is not a radiative point source, so an additional term must be added, if its shape and intensity is modelled through a simplified normal distribution. The subtended solid angle is 32°; which implies an angular radius of 4.653mrad (σ_{sun}).

$$\sigma^2_{c,total} = \sigma^2_{sun} + \sigma^2_{spec} + \sigma^2_{slope} + \sigma^2_{shape} + \sigma^2_{track}$$

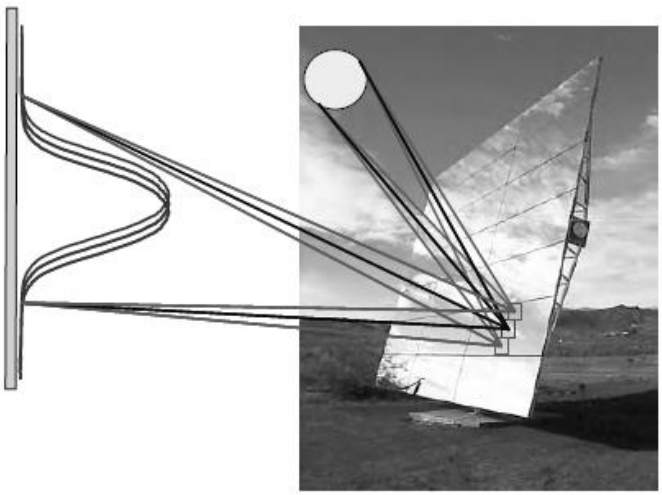

Figure 4-14: effect of errors on the reflected image of the heliostat (Romero-Alvarez M., 2007)

The final convolution of errors leads to an unacceptable spread of the focal spot when the distance of the heliostat from the tower increases. The degradation of the image sent to the aim point can be recovered cutting the mirror into facets that are later curved and brought back together in order to reproduce the segment of a paraboloid, or a cylinder or a sphere surface. This operation has been already explained, is referred to as canting and the focal length is equal to the slant range.

$$f = r/2$$

f is the focal length and *r* the curvature radius for a spherical symmetric heliostat.

Actually even this strategy becomes a source of degradation of the image, known as astigmatism, an off-axis aberration. The two curvature radii, indeed, make possible an effective reduction of the spot when the angle of incidence is close or equal to zero. When the incidence is non-normal ($\cos\theta < 1$), which is the usual operating condition, tangential and sagittal fans of parallels rays must be distinguished. The tangential ray fan consists of parallel rays in a plane defined by the sun, the target and the heliostat. A sagittal ray fan lies in a plane perpendicular to the tangential plane (Zaibel, et al., 1995). The focal length in the tangential direction is reduced by $\cos\theta$ and in the sagittal direction increased by $1/\cos\theta$.

$$F_{tang} = f \cos\theta$$

$$F_{sagit} = f / \cos\theta$$

The focal point is substituted by a two line foci with a circle of least confusion between them near *f*.

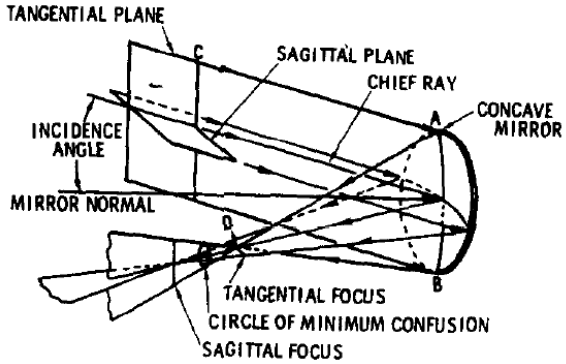

Figure 4-15: astigmatic foci of a concave mirror at oblique angle of incidence (Igel & Hughes, 1979)

The rays are spread over a larger area and the flux density drops; it appears clear that the larger is the angle of incidence θ, the larger is the image sent to the receiver plane.

The sum of optical errors and astigmatism leads to an energy loss called spillage: the overlapped images projected by each heliostat are deformed, so a part of the final global image spills out of receiver boundaries. Large receiver apertures allow low spillage loss, but on the other side, an excessively large receiver generates unacceptable radiative and convective losses. Generally a minimum flux spillage is tolerated for an optimized collector system (Lovegrove, 2012).

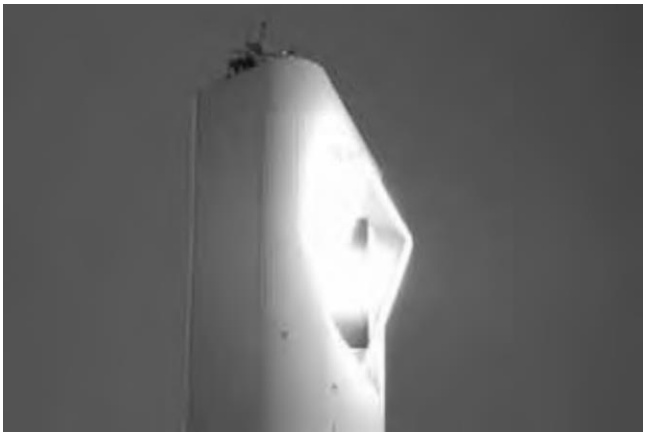

Figure 4-16: spillage loss at PS10 receiver

The efficiency breakdown of the PS10 heliostat field is shown in the table below, as well as its Sankey diagram.

Table 4-5: unweighted yearly PS10 heliostat field efficiency (Noone, et al., 2012)

Unweighted yearly heliostat field efficiency	
η_{cos}	0.8283
$\eta_{sh\ \&\ bl}$	0.9255
$\eta_{interception}$	0.9926
$\eta_{atm\ att}$	0.9498
η_{refl}	0.8800
$\eta_{opti,year}$	0.6401

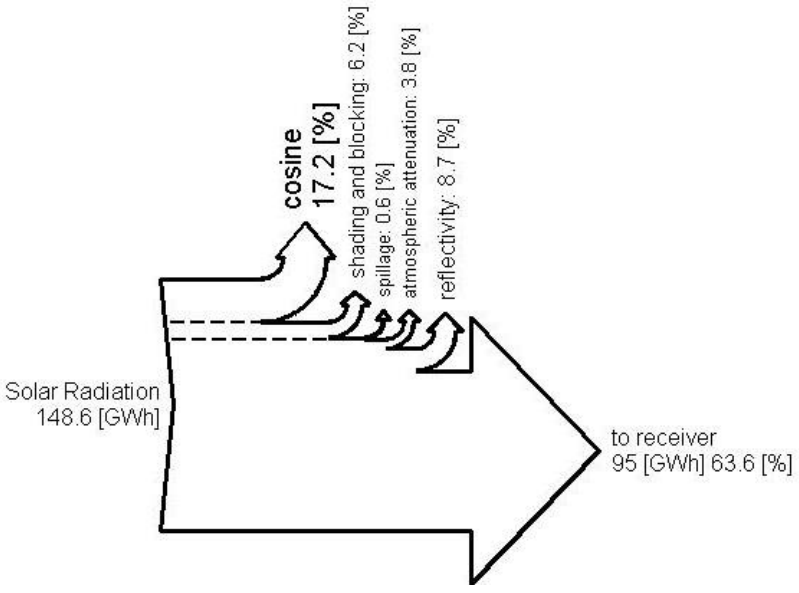

Figure 4-17: PS10 heliostat field Sankey diagram (graphic tool by J. Spelling)

5 Computer Codes for CRS

A number of software has been created for modelling and simulation of CRS systems; they space from the analysis of individual components of the various subsystems to optimization and general design of the entire plant.
Generally these codes can be grouped according to their function (optimization or simulation) or to their development period, dividing the tools of the 70s-80s from the latter ones, or either to the way they calculate the flux concentrated at the receiver.

The most important difference among these codes can be resumed in the trade-off between computational time and result accuracy.
Evaluation codes are able to estimate the energy sent by every single element of the field at the receiver with high precision, as their goal generally is to obtain the image of the reflected solar disk on the focal plane. The optical system must be described in detail, so as the sun shape and, sometimes, the atmospheric properties, such as molecular and aerosol scattering and atmospheric refraction: this allows a good prediction of the time-variant shape of the solar spot.
Two approaches are generally followed: ray-tracing or convolution techniques.

In classical Monte Carlo ray-tracing methods, a bundle of rays from a hypothetical sun plane impinges on each reflective surface and is redirected toward the receiver plane; if a surface is shaded it won't reflect any ray, while only the rays that are not blocked are conveyed to the aiming point. A statistic law for the error distribution is applied to determine the trajectory of the ray, which may not reach the focal plane due to defects of the facet, incorrect curvature, mounting or tracking.
Precision and requested time increase with the number of rays; the final flux distribution is obtained by summing the specific energy contribution of each ray impacting the different parts of the receiver plane.

In convolution-based codes, specular, shape, slope and tracking errors are modelled as normal Gaussian distributions. The final cone error associated to each reflected ray is the convolution of these errors. Together with the sun shape distribution, it is inserted into an analytic function able to reproduce the flux distribution in the receiver plane (Collado, et al., 1986).

Ray-tracing codes need more computational resources, but, being more flexible, they allow a complete optical analysis; nevertheless, reproducing the real interactions between photons and surfaces, the result accuracy doesn't decrease when the heliostat field is small. This situation bares the limit of convolution-based software.

Optimization codes rose to design the heliostat field that maximizes a given objective function, which uses to be the LCOE or the energy at the receiver. Several optimization algorithms have been tested, ranging from classical gradient-method to evolutionary ones. Such tools employ a simplified optical calculation based on a convolution technique because a typical field optimization searches for the best objective function through hundreds or even thousands of simulations, changing some parameters each time. Ray-tracing methods clearly appear unsuitable as still far from meeting the speed needed to contain computational time within acceptable bounds.
Finally, it should be reminded that in LCOE-optimization codes, the major source of

uncertainty is not represent by the simplified optical model, but by the polynomial approximation of the power block or storage.

5.1 Evaluation Codes

HELIOS: it's a first generation FORTRAN77-code, written in 1977 to analyze the experiments at the Sandia heliostat field facility. To evaluate the solar flux density in fields ranging from 1 to 599 heliostats (or cells with multiple heliostats), it uses an analytic convolution method when normal Gaussian distribution is assumed, otherwise the errors associated to independent distribution are convoluted by the means of Fourier transformations. Its most important characteristics are flexibility, low calculation time and accuracy, so that it has been applied not only to CRS but also to parabolic through collectors and dishes; on the other hand such flexibility is paid in terms of required knowledge about optics and solar radiation. The code takes into account shadowing, blocking, solar vector geometry, reflectivity, shape of the mirrors, facet orientation, but the input via user-specified text makes it hard to use for an unexperienced user. At the same time, post-processing software like Excel, Matlab or Mathematica is the only way to visualize the flux distribution Nowadays HELIOS is actively managed only by Sandia staff and, as other first generation codes, validates the optical model of new software and tools.

MIRVAL: is a Monte Carlo ray-tracing program that was developed for optical characterization of the four heliostat types proposed for the Solar One plant. The output is a detailed text, as also this FORTRAN code considers shadowing, blocking, tracking error, distribution of incoming rays, atmospheric scattering and absorption, and reflective surface shape; in addition three receiver configurations can be selected. Again, there is no visual interface, so software for post-processing is needed, as well as attention when inserting the parameters to run the simulation. Although the input is via specified-user text, it's considered simpler than HELIOS and has been updated at the DLR. In this European version, called *SPRAY*, new geometries and concentrators have been introduced, but the code is no longer freely available as MIRVAL was.

SOLTRACE: is a ray-tracing software developed in 2003 by NREL (National Renewable Energy Laboratories) which is able to model and analyze complex optical systems. These are organized in stages in a global coordinate system: each stage is composed by elements with their own physical and geometrical properties, including shape, slope and specularity errors beside reflectivity and transmissivity. The code offers a good degree of freedom in defining the sun shape distribution: pillbox, Gaussian and user-defined are the available options, although atmospheric attenuation and tracking errors remain excluded.
Flux maps and performance graphs may be displayed and saved; the feature, together with a friendly graphical user interface and the free download, makes SOLTRACE one of the most interesting tools presently. Unfortunately the complete description of the element and the stages pass through the definition of the center, the aperture, the normal direction, the curvature of each element in the stage coordinate system, and the definition of the stage coordinates within the global coordinate system. This implies a detailed calculation of the position of each concentrator (center and vertices) before running a simulation. Furthermore, as the input phase is not adequately supported by the view of the stage, this may lead to some errors, especially for systems formed by a large number of elements.

TONATIUH: this software is an open source ray-tracing code that enables visualization of the analyzed system thanks to a 3-D interface. It's a second generation code written in 2005 by CENER and the University of Texas and allows an easy simulation of a number of different concentrators and secondary optics, including beam-down configuration and every type of canting. Organized in stages as SOLTRACE, TONATIUH differs substantially during the input phase: once defined the concentrator and its location in the global coordinate system, the orientation of the element changes automatically according to the sun position, thanks to the "tracker". Those are no more than a built-in function that adjust concentrator position without any intervention of the user.
Optical errors are treated as probability functions, except tracking errors that are neglected; two sun shapes can be selected (Buie or Pillbox) and six different atmospheric attenuation models have been implemented. In this case no flux map is provided, so external software is required to follow out the analysis. A secondary drawback is code stability, not always guaranteed if the number of rays traced is very high.
In conclusion, this software can aim to a brilliant future: it's easy even for non-experienced users, freely available and continuously updated, but still need some improvements and, above all, a user guide.

STRAL: the name stands for Solar Tower Ray-tracing Laboratory. This code has been presented in 2009 and it's probably the most advanced code, not as much talking about the optical model, but rather because of the several connection possibilities with external software.
Developed in a C++ environment by the German Aerospace Center (DLR), it makes use of the complex architecture of today's single and multicore CPUs in order to take advantage of parallel computation. The real turning key is represented by its new Monte Carlo ray tracing approach: each reflective surface is divided in a number of subareas, each one characterized by its normal vector, depending on the chosen shape geometry. Then, a bundle of sunrays is generated and each sunray is deflected from the main direction of the sun vector, according to the given sun shape distribution. The reflected ray of each single subarea of the raster is calculated as a combination of the corresponding local normal vector $\vec{n}$ and a sun ray $\vec{s}$, which is randomly selected from the initially generated bundle of sun rays (Belhomme, et al., 2009). In this way the number of generated rays is reduced and those which would have impinged on the ground (sometimes more than the 60% of the total number of rays) are not created.
This software is equipped with a user-friendly GUI and visualizes the flux performance maps on screen; moreover it can communicate with finite-elements software used during the heliostat design, thus checking the best alternative. An aiming point optimization strategy was implemented as well, thanks to STRAL modularity (Belhomme, et al., 2014).

Beside those codes, some more are available, but less described and cited in scientific literature: FIATLUX, ASAP, SOLFAST, TIESOL and CRS4-2 enter in this group.

5.2 Optimization Codes

DELSOL: it's a first generation code, and the first release dates back to 1978, as it was developed for Solar One field design by the University of Houston. Written in FORTRAN, the input is via user-specified text and a good knowledge of the code is required not to chance upon language errors.
System Advisory Model (SAM) is well-known software created by NREL for performance

and design calculation of renewable energy systems and includes an adapted version of DELSOL in the CRS section.
The optimization is dedicated to large CRS dedicated to power generation, as many assumptions are taken to speed up the computational time: the field is divided into several cells, each one with its own mirror density, whose position is defined by the azimuthal and radial distance from the tower. During system optimization, DELSOL not only compares different systems, but also defines the heliostat field to meet the required power level. Indeed, at every step, the configuration of tower, heliostat size and receiver dimensions may lead to a different number of mirrors as field efficiency depends on those variables; the number of heliostats required varies to reflect the difference between the fields created.
DELSOL must recalculate the zone-by-zone annual average and design point optical performances at each new tower height and receiver size to find the requested design point power. The code does this by "scaling" the results of a detailed initial performance calculation. The initial performance run calculates heliostat images for each zone for each time step, and from that information calculates an annual average heliostat image for each zone. This is later scaled with the tower height during the optimization and combined with the design point efficiency to calculate the design point power, and with the annual average efficiency to obtain the annual energy. The field is built up by allocating the heliostats in the zones within the field boundaries; the zones are filled starting with the one having the highest annual yearly insolation. The code in addition leaves the chance to optimize even the heliostat density of every zone.
Finally, the searching algorithm finds the best system design, coupling the optical and thermodynamic performances with a cost model of every component, looking for the minimum LCOE.
DELSOL simulates the effects of cosine, shadowing, blocking, atmospheric attenuation, spillage and flux profiles. The prediction of the image at the receiver is realized thanks to an optical model based on an analytical Hermite polynomial expansion/convolution-of-moments method. The software takes into account flat, focused or canted heliostats with round or rectangular shapes; external, multiple aperture cavity, or multiple flat plate receivers; and variable aiming strategies (Kistler, 1986). The optical result is then combined with the efficiency of the other component of the plant to calculate the LCOE.
On one hand DELSOL appears a really powerful code especially because of its speed: a short time is enough to obtain a first field configuration. Energy and cost assessment have been validated with different case studies, including the one of Gemasolar (with SAM). On the other hand it has been recognized that the "scaling" operation and the simple optical model doesn't work properly with small fields. The accuracy of the Hermite method increases as the error sources of heliostat performance and/or their effect on the flux profile become larger. Specifically, DELSOL becomes more accurate in predicting the flux and spillage when:

- the magnitude of errors increase
- the slant range increases
- the size of the heliostat is reduced (either physically or effectively by focusing or canting).

Besides that, although the cost model is very detailed and well documented, it reports cost functions of 1980s, when the leading trend was bigger heliostat/less cost. Therefore a revision

seems necessary to include properly in the optimization search even the new fields made up of small heliostats.

In 2002 CIEMAT, AICIA and Solúcar released an adaptation of DELSOL for Windows, called WINDELSOL. The most interesting features are the user-friendly interface and the output window that shows a qualitative result of field optimization. However it can't assess annual simulations for existing or projected facilities, as heliostat coordinates are not user-defined, and its optical model is equal to DELSOL one, thus being not accurate for small plants.

HFLCAL: this code (Heliostat Field Layout Calculations) was developed for the GAST hybrid concept. In 1994 the German Aerospace Center (DLR) bought it and added a GUI, which is partially the reason why this software became so widespread in Europe among research facilities.
It calculates the annual production of a CRS plant depending on heliostat, tower, receiver and cycle configurations which makes it really flexible. The field can be optimized according to two criteria: maximization of the electricity produced per heliostat or minimization the cost of produced electricity. To do that, it adopts two optimization methods, the Powell's conjugate direction method and a genetic algorithm, which lead to a fast solution of the problem, even if sometimes it's just a local maximum/minimum. The user can choose to employ one method or the other or even their combination.
The optical model is obviously simplified, and the flux distribution of each heliostat is approached by a circular Gaussian distribution resulting from the convolution of four distributions: the first relative to the sun shape, the second accounting for the slope error, the third for tracking error and the fourth for astigmatism. The assumption of circular distribution, as for DELSOL, is a correct approximation the higher is the number of heliostats and the higher is the error magnitude, as the total modelled cone error converges to the real one for the Central Limit Theorem. About astigmatism, it's worth pointing out that in this way there is no chance to reproduce adequately a asymmetric aberration, which often occur with the heliostats with the highest azimuthal distance from the tower. In fact, comparisons with experimental measures and ray-tracing programs demonstrated that HFLCAL is able to predict with high precision the total energy collected at the receiver, whereas the maximum flux and the flux distribution are less accurate.
As this software is not free, it's impossible to modify the source code, neither to study it, so no information is available about the power block and the energy storage modules. The only available option is to custom the economic and the receiver modules in order to introduce user-defined functions.

YNES: in order to draw the field layout, YNES employs a completely different approach, compared to the others codes, and it should be better defined as a refinement code. It takes as input a heliostat field generated by other software like DELSOL and starts the optimization procedure applying its so-called heliostat growth method (HGM).
The first step consists in calculating the Yearly Energy Available from a TMY data, as the product of cosine, atmospheric attenuation and spillage factors for the whole field; the collector subsystem is organized in a grid, whose points are the vertices of 1mx1m squares. The result is the Yearly Normalized Energy Surface (YNES) that represents the yearly energy usable at every point of the aforementioned grid, without accounting for shading and blocking, that doesn't depend on the position but only on the interactions between neighboring mirrors.

The first heliostat is placed where the YNES is maximum, in the point closest to the tower. Later, yearly normalized shading and blocking are added to the affected points and the successive heliostat is positioned. The procedure is repeated for all the heliostats in the field, eased by some simplifications during the calculations of shading and blocking effects. Finally, a weighting factor penalizing excessive widening of the field is introduced.
To stress the goodness of this method, a field obtained by WinDelsol and its modified version by YNES were compared, showing that such refinement allows a higher annual efficiency (>3% in the case study) (Sánchez & Romero, 2006).
A similar methodology was developed by the German Aerospace Center (DLR) and implemented in the ray tracing software SPRAY, derived from MIRVAL. The refinement enhances field performance and it appears very interesting above all for small fields, that the most of optimization codes penalize because of optical simplifications (Buck, 2014).

MIT CODE: it's one of the most recent codes, was written in 2011 at the Massachusetts Institute of Technology and is exclusively dedicated to heliostat field optimization, as it doesn't consider any other part of a typical CRS plant.
The model proposed for the calculation of heliostat optical efficiency accounts for cosine losses, shading and blocking, receiver interception, atmospheric attenuation and heliostat reflectivity. The most interesting feature of this code is the new biomimetic pattern proposed for the field and the discretization of the heliostat surface for flux and spillage calculation. The flux calculation is more accurate than in DELSOL or HFLCAL, because, although the error components are the same, the surface normal of each facet determines the direction of the reflected ray as a function of its own orientation. Thanks to this smart idea, the code is able to reproduce a really good approximation of the astigmatism effect for focused heliostats and to reduce the time needed for shadowing and blocking evaluation.
Two types of pattern can be optimized: radially staggered or biomimetic. The first depends on two parameters which control the distance between successive rows and when the rows must split. Nominal values for radial and azimuthal separation are taken from DELSOL, and are function of the angle formed by the position of the heliostat center on the ground and the receiver aperture altitude. The second pattern is far more innovative and is inspired from spiral patterns of the phyllotaxis disc, that is, for example, the configuration of florets on the head of a sunflower. The advantage is that the transition from high to low mirror density is continuous, and where the density is higher, i.e. close to the tower, shading and blocking losses are kept within acceptable values. The resulting field is more compact and needs fewer heliostats than a radially staggered one to reach the same power conveyed at the receiver. The optimization process depends again on only two parameters. For both the field types a gradient-based optimization method is used; the process consists in generating a pattern much larger than the expected size (five time larger); then the candidate locations are sorted by their individual efficiencies. The n heliostats that compose the field are evaluated with all their efficiency factors and the annual weighted efficiency is calculated. The process is repeated for the times required by the optimization algorithm to find a number of points on a Pareto curve, to finally choose the better trade-off between annual efficiency and field area (Noone, et al., 2012).

NSPOC: it's a tool for optimization of CRS plants based on the ASPOC code developed within the GAST project (1982-86). It looks for the best configuration of heliostat positions, tower height, receiver size and inclination, and field shape (circular or non-circular, single-tower or multi-tower). It has been written in FORTRAN77 and it doesn't have any GUI, neither for input nor for output data; it means that there is substantially no difference between

user and developer, as a good knowledge of the code is required to compile the input text. This software optimizes the field layout by the means of multiple evaluations of plant configuration: cosine losses, shading and blocking, atmospheric attenuation, spillage are combined with receiver and power block efficiencies.
The optical model behind NSPOC is quite similar to the HFLCAL one, so that the errors associated to each heliostat are treated as circular Gaussian distributions; sun shape and slope error are taken into account, tracking error is not. Astigmatism for canted mirrors is modelled as well with a circular normal distribution and this doesn't allow appreciating the asymmetry of the heliostat image directed to the focal plane, thus lowering the accuracy of the calculated maximum flux and the flux distribution.
As the variable geometry field analyzed is obtained from an adapted version of NSPOC, the optimization method is briefly described, following the same path traced by the authors.
The optimization procedure requires multiple evaluation of the objective function (LCOE or maximum energy at the receiver) and, because of the CPU cost, the variables that determine the final plant layout are reduced to 11, while the inputs needed are just seven more the environment data.

The input parameters do not vary throughout plant optimization, they are related to heliostat size and their optical properties, geographic, insolation and temperature data of the site where the plant will be built and:

a) σ_H: heliostat optical error

b) L_H: heliostat length

c) W_H: heliostat width

d) ϕ: plant latitude

e) β_{N-S}: north-south slope of the terrain

f) β_{E-W}: east-west slope of the terrain

g) DNI: insolation model

h) T: ambient temperature

The variables are grouped in collector field variables (8) and receiver variables (3).
Starting from the first group, and imagining a circular field, the distance of the *n-th* heliostat in the first row from the the tower is given by:

$$R_n = a_0 + (a_1 + 1)R_{n-1}$$

$$R_0 = R_{base}$$

1) a_0: initial spacing between heliostat rows [m]

2) a_1: increasing spacing between heliostat rows

R_0 is the distance between the first line and the tower and the distance between any couple of lines must be greater or equal than the minimal distance R_{min} that depends mainly on heliostat size.

If the shape of the lines is not perfectly circular there is the chance to introduce an additional increment that is expressed as function on the azimuthal position of the heliostat:

$$\Delta R = \begin{cases} d_\theta \theta & for\ 0 < \theta \leq \pi \\ d_\theta\ (2\pi - \theta) & for\ \pi < \theta < 2\pi \end{cases}$$

3) d_θ: correction of the radial distance with the azimuthal position

θ is the azimuthal separation between a heliostat and the north axis (zero azimuth) and when $d_\theta < 0$ heliostats are more compact in the southern part of the field.
Inside each line, the azimuthal separation must be calculated as well between successive heliostats, remembering that it varies according to both azimuthal angle and radial distance. Let's focus first on the first line: being D_α^1 the azimuthal distance for the heliostat that lays in the north axis, and indexing the other heliostats with α = 1,2,.., the azimuthal distance is calculated as:

$$D_\alpha^1 = D_{\alpha-1}^1 + e_\theta \theta$$

4) e_θ: variation of the azimuthal distance with the azimuthal angle

This is valid only for the first line, the remaining lines are plotted introducing the condition of radial staggered positions, so that for the azimuthal angle of the first heliostat in the n^{th} row is the average of the azimuthal position of the two heliostats in front of it.
To avoid an excessively fast widening of the heliostats after few rows, it's worth adding an extra space between two consecutive lines and starting again the rule of formation. The lines in which this happens are called transition lines. Heliostats between two transition lines belong to the same group. The distance between two groups is given by:

$$\Delta = (1 + a_0 + a_1 R)\delta + \varepsilon$$

5) ε: extra distance for transition lines [m]

6) δ: increment of distance as a function of tower distance

Once a group ends, the azimuthal rule of formation in each line of the new group must start again. For the group *j*:

$$D_\alpha^j = D_{\alpha-1}^j + e_\theta \theta$$

It appears clear that the distance values of the different groups must be controlled by a relation between the first elements of the considered group and the previous one:

$$D_0^j = (b + 1) D_0^{j-1}$$

7) b: parameter for increasing azimuthal distance of the first row of every group

8) D_0^1: initial azimuthal distance in the first line of heliostats

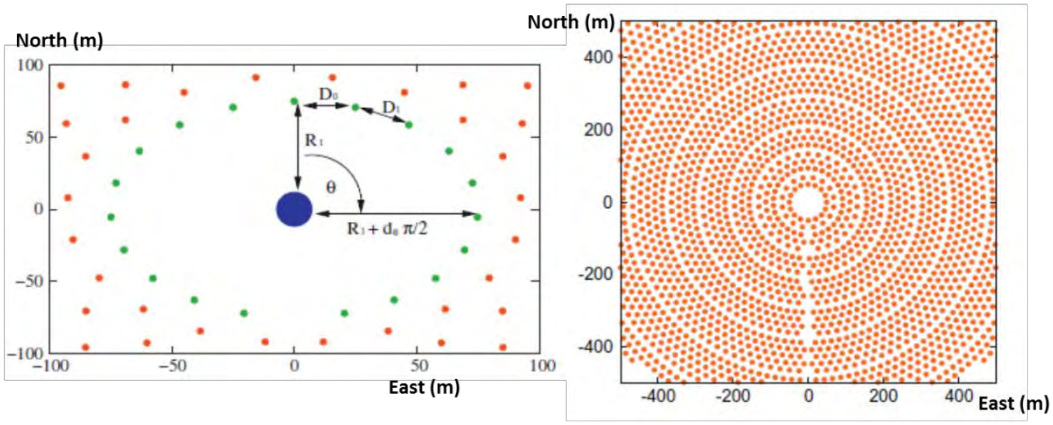

Figure 5-1: left, azimuthal distance for the first line of a non-circular field; right, view of groups and transition lines for a large circular heliostat field (Ramos & Ramos, 2012)

The final layout of the field depends also on the receiver chosen. With a cavity receiver the field will be polar-like and the remaining optimized variables are:

9) h_T: tower height

10) r: aperture radius

11) γ: aperture inclination

otherwise a circular field has to be matched with a cylindrical receiver, so receiver radius and receiver height substitute aperture radius and its inclination (Ramos & Ramos, 2012).
Receiver and cycle efficiencies come from a polynomial function whose coefficients have been determined by fitting data: this allows a rapid estimate of daily and yearly energies from clear sky and TMY insolation data.

Due to the non-linear nature of the objective function and the high computational costs, the optimization algorithm must be fast and able not to stop in local minima/maxima. For this purpose an optimization algorithm has been written specifically: the NSPOC algorithm is a variant of Powell's conjugate direction method. Starting from an approximate value of the vector of optimal variables $\overrightarrow{x^{(0)}}$, the algorithm performs a line search along the first direction x_1 until an optimum is found with precision ε; then the algorithm repeats the search for the eleven variables. In other words the method reaches to the optimum in a "zig-zag" way, taking advantage of the fact that the objective function doesn't have to be fully evaluate at each step; for example, for a field configuration different tower heights and aperture inclinations may be tried without computing other times shading and blocking effects.
The authors compared their optimization code with two robust global optimizers, respectively a combination of two methods coded in the MINUIT library and a genetic algorithm.
In the first case a Monte Carlo search that has a good ability to jump over local minima/maxima is coupled with a quasi-Newton method, while in the second the process of natural evolution is mimicked by creating a "population" and implementing natural-inspired mechanisms as crossover, mutation and natural selection. In this way genetic algorithms are considered able to explore a large solution space, thus appearing more likely to converge towards a global optimum. A detailed description of this algorithm is explained in the next chapter.
Trying the three different algorithms with two different plant configurations (900 and 3000

heliostats) the NSPOC algorithm resulted always to be the one able to find the best value of the objective function in the lower time.

6 Developed Code

From the previous review of existing codes for field optimization, it has emerged that there isn't any tool dedicated to design and simulation of a variable-geometry field. Actually the only chance would be an option in WinDelsol, but it doesn't give any further possibility to modify the field created, neither to assess annual performance of different or modified field configurations.
Secondly, the available optimization codes have been written with large CRS in mind, so shading and blocking calculation is usually affected by quite different approximations because of the number of iterations that would require the exact evaluation of this efficiency factor. About this topic, one should remember that such codes don't account either for tower shadow, which has a limited impact in plants with thousands of heliostats, but may have a great influence in small fields (less than 100 mirrors).

Because of the aforementioned reasons, a simple and fast code has been developed in order to assess instantaneous and long-term performance of every polar field, but in particular of the small variable geometry facility analyzed. Such code has been integrated later with an optimization code to evaluate, in principle, the best position for the heliomobiles to be implemented in an open-loop control system.
The model evaluates cosine, shading and blocking, atmospheric attenuation, reflectivity and spillage losses; the shadow cast by the tower is included.

As we are speaking about a small field, the factors mainly involved in the reduction of the optical efficiency are geometrical, if the field doesn't widen over the acceptance angle of the receiver and the mirrors are canted correctly. That said, this code focuses on cosine and shading and blocking losses rather than spillage evaluation, so the so-called "geometrical factor" is calculated precisely thanks to vector and matrix calculations. On the other side the interception efficiency is assessed from a statistical point of view and the atmospheric attenuation factor is expressed as a polynomial function of the slant range between the rotational center of the heliomobile and the aim point. Reflectivity is supposed to be constant, as a correction for dust and dirt depositions is applied with the cleanliness factor.

The code is written in Matlab® because of the flexibility provided by a number of integrated tools which can be easily called during each run.
Matlab® is a high-level language and interactive environment that enables any user to enter in the world of technical computing; beside built-in functions dedicated to linear algebra, statistics, Fourier analysis, numerical integration and optimization, it can communicate (data import/export) with external applications such as Microsoft® Excel®.
The name stands for "MATrix LABoratory"; the first word suggests the advantage that characterizes this software: while many other programming languages mostly work with numbers one at a time, it is designed to operate primarily on whole matrices and arrays in order to reduce computational time. In addition, the user can develop his own functions, i.e. scripts that perform computational tasks, and call them wherever he wants. This represents a second strength as it gives the possibility to create a script somehow modular.

6.1 Simulation Tool

This section describes the structure of the simulation/evaluation part of the code, which is made up of a central body and several functions.

First of all it's worth introducing the reader to the structure of the model, as it moves between four coordinate systems:

1) Tower system: it's a right-handed coordinate system whose center is located in the center of the tower base. The x axis lays in the direction West-East (East positive), the y axis in the direction South-North (North positive), and z axis points towards Zenith

2) Heliostat system: it's a right-handed coordinate system whose center is located in the rotational center of the heliostat. The x axis is parallel to heliostat horizontal side, the y axis parallel to the vertical side; the z axis lays on the surface normal direction and is positive oriented toward the outgoing direction

3) Sun system: it's a right-handed coordinate system whose center is located in the center of the tower base. The z axis lays on the sun vector and is positive oriented towards Sun, while the other two unit vectors are calculated in order to complete a orthonormal base

4) Reflected ray system: it's a right-handed coordinate system whose center is located in the rotational center of the heliostat. The z axis corresponds to the reflected ray unit vector of the heliostat considered, while the other two unit vectors are calculated in order to complete a orthonormal base

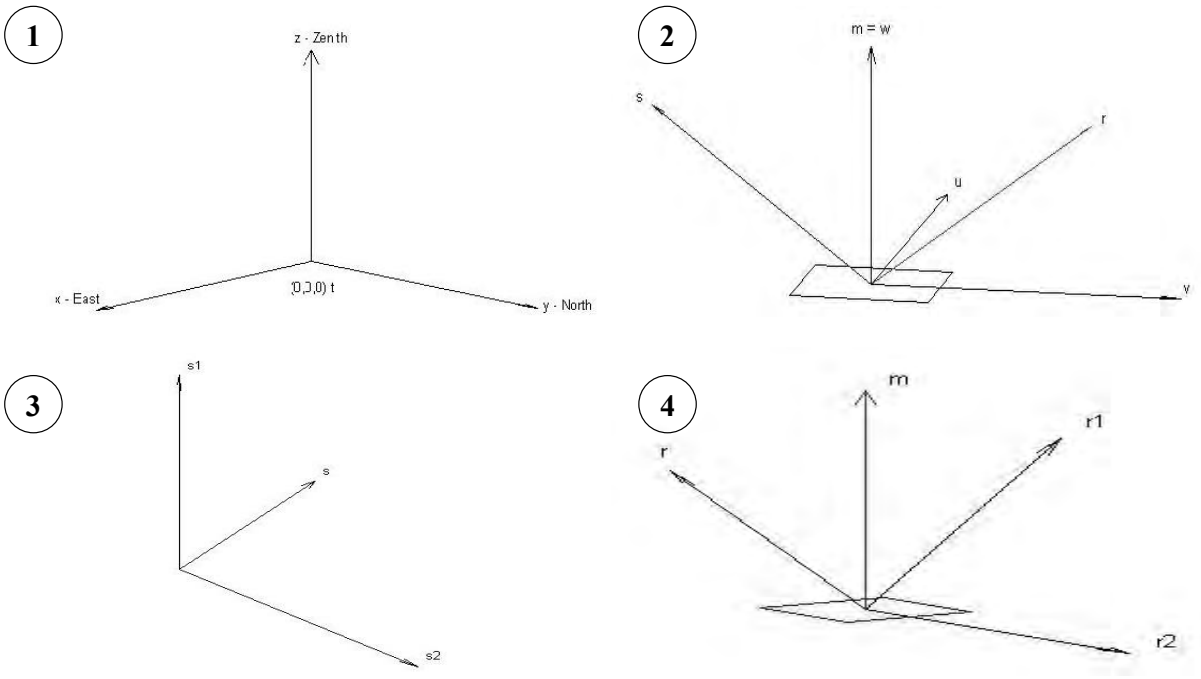

Figure 6-1: coordinate systems used in the model

That said, the code assumes each heliostat as a flat rectangle whose allowable movements are only rotation in azimuth and rotation in elevation; this doesn't mean that canted mirrors are not taken into account, but just that they are "flattened" in order to accelerate the calculation of shading and blocking.
Circular reflective surfaces, on the contrary, are neglected as there is still no field composed by this kind of heliostats. The second strong assumption concerns receiver geometry: only cavity receivers with circular apertures are considered. Finally, the errors associated to solar disc, slope and tracking are modelled as normal Gaussian distributions.

A number of input data are required in order to obtain the instantaneous optical efficiency of the collector field:

- *X, Y, Z*: coordinates of each heliostat rotational center
- Julian day number, hour of the day and DNI
- ϕ, latitude of the field and eventually λ, longitude, when local time is considered
- n_{sb}, number of neighboring heliostats that the code checks for shadowing and blocking effect
- l_h, heliostat length
- w_h, heliostat width
- R_{ap}, receiver radius
- γ, tilt angle of the receiver respect to the horizontal plane, parallel to the ground
- tower dimensions, if the code must check also the shadow of the tower
- reflectivity ρ and cleanliness
- σ_{sun}, σ_{slope}, σ_{track}, the standard deviations that determine the cone error of each reflected ray

The evaluation requires some steps, so that the script determines in order:

1) Sun position and solar vector
2) surface normal and reflected ray unit vectors
3) cosine factor
4) the position of the vertices of each heliostat in the field
5) shading and blocking factor
6) distance of each heliostat from the aim point
7) atmospheric attenuation
8) reflectivity

9) interception efficiency

10) optical efficiency, power at the receiver, incident and lost power

Sun position: the position of the sun in the sky and the components of the sun vector are gathered from the julian day of the year n_{day}, the hour of the day h, the latitude of the plant ϕ and the longitude λ if the considered time is local and not solar.
Spherical trigonometry and vectorial approach have been used to derive some of the necessary equations. Solar declination (in degrees), solar hour and solar hour angle (in degrees) are expressed by:

$$\delta = 23.45 \sin\left[\frac{360}{365}\left(284 + n_{day}\right)\right]$$

$$st = h - 12$$

$$\omega = 15\, st$$

When the longitude correction is applied, the solar hour is modified according to the following equations:

$$\Gamma = \frac{2\pi}{365}\left(n_{day} - 1\right)$$

$$et = \frac{229.2}{60}\left(0.000075 + 0.001868\cos\Gamma - 0.032077\sin\Gamma - 0.014615\cos(2\Gamma) - 0.04089\sin(2\Gamma)\right)$$

$$lc = \frac{\lambda}{15}$$

$$st = h + lc + et - 12$$

where Γ is the day angle, latter used in the equation-of-time correction, and lc is the longitude correction (λ in degrees).
Therefore, it's possible to write down expressions for the solar unit vector components in the Tower reference frame (Sproul, 2007):

$$s_x = -\cos\delta\sin\omega$$

$$s_y = \sin\delta\cos\phi - \cos\delta\sin\phi\cos\omega$$

$$s_z = \cos\delta\cos\phi\cos\omega + \sin\delta\sin\phi$$

By vector analysis it is easy to derive sun elevation α_s, being $\vec{s}$ a unit vector:

$$\sin\alpha_s = \frac{s_z}{s} = \cos\delta\cos\phi\cos\omega + \sin\delta\sin\phi$$

On the other side, the azimuth of the sun γ_s is the angle between the horizontal component of $\vec{s}$ and South direction:

$$\cos\gamma_{s,*} = \frac{-s_y}{\sqrt{{s_x}^2 + {s_y}^2}} = \frac{-s_y}{s\ \cos\alpha_s} = \frac{\cos\delta\sin\phi\cos\omega - \sin\delta\cos\phi}{\cos\alpha_s}$$

Last equation cannot determine whether sun is at East or West of the observer, as $s\ \cos\alpha_s$ has the same value for positive either negative values of the hour angle (i.e. it is morning or afternoon). According to the convention used herein, azimuth angle is positive from South (0°) to West (90°), so that:

$$\begin{cases} \gamma_s = \gamma_{s,*} & if\ \omega > 0 \\ \gamma_s = -\gamma_{s,*} & if\ \omega < 0 \end{cases}$$

Aim point: the aim point is defined as the center of the circular aperture of the receiver. Naming w_r the width of the receiver, h_t the height of the tower, from the ground till the base of the receiver, h_r the height of the receiver, each mirror will convey the reflected radiation to the target *T*:

$$T_x = 0$$

$$T_y = \frac{w_r}{2}$$

$$T_z = h_t + h_r/2$$

According to the above equations, in the Tower frame, the aim point is directed toward North, and such direction is fixed except in the case of a rotating receiver, which is the one that is supposed to be installed in the CTAER pilot plant. This configuration would reduce spillage losses and lower cosine losses during morning and afternoon. Assuming the receiver moving at the same angular speed of the sun, the coordinates of the target in every instant of the day depend on sun unit vector as well. If T is in the "rest position", the plane of the receiver is oriented by the means of a rotation of an angle θ_T around the z axis (pointing towards Zenith in the Tower frame). Being θ_T the angle between the North axis and the vectorial sum of s_x and s_y in the East-North plane, the rotated target coordinates are expressed by:

$$M_{\theta_T} = \begin{bmatrix} \cos\theta_T & -\sin\theta_T & 0 \\ \sin\theta_T & \cos\theta_T & 0 \\ 0 & 0 & 1 \end{bmatrix}$$

$$T_{\theta_T} = M_{\theta_T} * T$$

Reflected ray and normal unit vectors: once both the coordinates of the heliostat centers and the aiming point are known, this step determines for each element in the field the three components of $\vec{r}$ and $\vec{m}$, respectively the reflected ray and the surface normal unit vectors. In the Tower frame:

$$r_{i,x} = \frac{T_x - X_i}{\sqrt{(T_x - X_i)^2 + \left(T_y - Y_i\right)^2 + (T_z - Z_i)^2}}$$

$$r_{i,y} = \frac{T_y - Y_i}{\sqrt{(T_x - X_i)^2 + \left(T_y - Y_i\right)^2 + (T_z - Z_i)^2}}$$

$$r_{i,z} = \frac{T_z - Z_i}{\sqrt{(T_x - X_i)^2 + (T_y - Y_i)^2 + (T_z - Z_i)^2}}$$

Because of Snell's Law of Reflection, the incoming solar ray and the reflected ray must lay on the same plane, which makes possible finding the components of the unit vector of the normal to the heliostat surface with a vector sum:

$$m_{i,x} = \frac{s_x + r_{i,x}}{\sqrt{\left(s_x - r_{i,x}\right)^2 + \left(s_y - r_{i,y}\right)^2 + \left(s_z - r_{i,z}\right)^2}}$$

$$m_{i,y} = \frac{s_y + r_{i,y}}{\sqrt{\left(s_x - r_{i,x}\right)^2 + \left(s_y - r_{i,y}\right)^2 + \left(s_z - r_{i,z}\right)^2}}$$

$$m_{i,z} = \frac{s_z + r_{i,z}}{\sqrt{(s_x - r_{i,x})^2 + (s_y - r_{i,y})^2 + (s_z - r_{i,z})^2}}$$

Cosine factor: the cosine factor, which coincides with the cosine efficiency, determines the effective reflection area of each heliostat. The Law of Reflection comes in help again, as the dot product of the sun and the reflected ray unit vectors is exactly the sought value:

$$\eta_{cos,i} = \cos\theta_i = \vec{s} \cdot \overrightarrow{m_i} = \overrightarrow{m_i} \cdot \vec{r_i}$$

θ_i is the angle of incidence of the *i-th* heliostat.

Vertices: this function calculates the position in the field of the vertices of each heliostat *i*. Its orientation is described by a movement with respect to an initial status in the point $(0,0,0)_{\text{Tower}}$; the surface plane of the heliostat is parallel to the East-Zenith one and the normal to its surface $\overrightarrow{m_i}$ is pointing to South. In the Tower reference system, at first the mirror is rotated by an angle β_i around the z axis, then by an angle α_i around the x axis. The correct orientation is realized through two rotational matrices (Leonardi & D'Aguanno, 2011). Finally the heliostat is shifted to its own position in the field by adding its center coordinates.

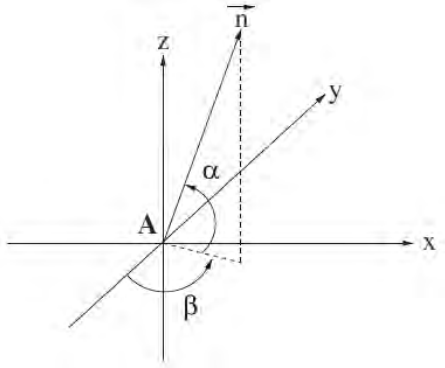

Figure 6-2: α and β angles, A is the center of the heliostat and $\vec{n}$ the normal to its surface (Leonardi & D'Aguanno, 2011)

$$\tan \alpha_i = \frac{m_{i,z}}{\sqrt{{m_{i,x}}^2 + {m_{i,y}}^2}}$$

$$\cos \beta_{i,1} = \left| \frac{m_{i,y}}{\sqrt{{m_{i,x}}^2 + {m_{i,y}}^2}} \right| \qquad \cos \beta_{i,2} = \left| \frac{m_{i,x}}{\sqrt{{m_{i,x}}^2 + {m_{i,y}}^2}} \right|$$

$$\begin{cases} \beta_i = \beta_{i,1} & if\ m_{i,x} > 0 \cup m_{i,y} < 0 \\ \beta_i = \frac{\pi}{2} + \beta_{i,2} & if\ m_{i,x} > 0 \cup m_{i,y} > 0 \\ \beta_i = -\beta_{i,1} & if\ m_{i,x} < 0 \cup m_{i,y} < 0 \\ \beta_i = -\left(\frac{\pi}{2} + \beta_{i,2}\right) & if\ m_{i,x} < 0 \cup m_{i,y} > 0 \end{cases}$$

$$M_{x,i} = \begin{bmatrix} 1 & 0 & 0 \\ 0 & \cos \alpha_i & \sin \alpha_i \\ 0 & -\sin \alpha_i & \cos \alpha_i \end{bmatrix}$$

$$M_{z,i} = \begin{bmatrix} \cos \beta_i & -\sin \beta_i & 0 \\ \sin \beta_i & \cos \beta_i & 0 \\ 0 & 0 & 1 \end{bmatrix}$$

The coordinates of the four vertices in the initial status are:

$X_{V1} = -w_h/2$	$X_{V2} = -w_h/2$	$X_{V3} = w_h/2$	$X_{V4} = w_h/2$
$Y_{V1} = 0$	$Y_{V2} = 0$	$Y_{V3} = 0$	$Y_{V4} = 0$
$Z_{V1} = -l_h/2$	$Z_{V2} = l_h/2$	$Z_{V3} = l_h/2$	$Z_{V4} = -l_h/2$

$$H_{Vi,H} = \begin{bmatrix} X_{V1} & X_{V2} & X_{V3} & X_{V4} \\ Y_{V2} & Y_{V2} & Y_{V3} & Y_{V4} \\ Z_{V1} & Z_{V2} & Z_{V3} & Z_{V4} \end{bmatrix}$$

The matrix formed by the coordinates of each vertex of the considered heliostat *i* is:

$$H_{Vi,T} = M_{z,i} * M_{x,i} * H_{Vi,H} + \begin{bmatrix} X_i \\ Y_i \\ Z_i \end{bmatrix}$$

<u>*Adjacent*</u>: this function finds the n_{sb} heliostats closest to the considered heliostat i. A generic mirror j has a distance from i equal to:

$$d_{j-i} = \sqrt{(X_j - X_i)^2 + (Y_j - Y_i)^2 + (Z_j - Z_i)^2}$$

These distances are arranged along a column vector in increasing order, and only the indices of the first n_{sb} elements are saved and used subsequently, when the function is called for the heliostat i.

<u>*Tower*</u>: this function calculates the profiles of the tower and the receiver in the Tower frame. The steel structure at the CTAER is a trapezoid, but for sake of simplicity only the section of a cut cone stands for the tower, while a square section represents the receiver. Initially the two superimposed sections lay in the East-Zenith plane, and then they are rotated in order to keep them perpendicular to the $(\overrightarrow{s_x} + \overrightarrow{s_y})$ direction. In the Tower frame, the boundaries of the overall section are fixed by six points, whose coordinates are:

$X_{T1} = -b_t/2$	$X_{T2} = - w_r/2$	$X_{T3} = -w_r/2$	$X_{T4} = w_r/2$	$X_{T5} = w_r/2$	$X_{T6} = b_t/2$
$Y_{T1} = 0$	$Y_{T2} = 0$	$Y_{T3} = 0$	$Y_{T4} = 0$	$Y_{T5} = 0$	$Y_{T6} = 0$
$Z_{T1} = 0$	$Z_{T2} = h_t$	$Z_{T3} = h_r$	$Z_{T4} = h_r$	$Z_{T5} = h_t$	$Z_{T6} = 0$

Where b_t is the length of the tower base, h_t its height, w_r the width of the receiver and h_r its height.

$$T_T = \begin{bmatrix} X_{T1} & X_{T2} & X_{T3} & X_{T4} & X_{T5} & X_{T6} \\ Y_{T1} & Y_{T2} & Y_{T3} & Y_{T4} & Y_{T5} & Y_{T6} \\ Z_{T1} & Z_{T2} & Z_{T3} & Z_{T4} & Z_{T5} & Z_{T6} \end{bmatrix}$$

Being θ_T the same angle introduced in the *aim point* paragraph, the above mentioned points of the section are correctly oriented by the rotation matrix M_{θ_T}:

$$M_{\theta_T} = \begin{bmatrix} \cos\theta_T & -\sin\theta_T & 0 \\ \sin\theta_T & \cos\theta_T & 0 \\ 0 & 0 & 1 \end{bmatrix}$$

$$T_{T,\theta_T} = M_{\theta_T} * T_T$$

<u>*Shading and blocking*</u>: the method employed herein for the calculation of the shading and blocking factor is not based on approximations or simplified assumptions, but rather it gives the its exact value thanks to a geometric approach element by element. Another important feature of the code is that also the shadow cast by the tower is taken into account.

For the shading factor, the function projects the heliostat field on a plane perpendicular to the sun beams in order to get the overlapping areas cast by the involved mirrors on the heliostat *i*; in a second phase, the shade-free surfaces are projected back along a plane perpendicular to the reflected ray $\vec{r_i}$. The portion of the area, not blocked by the front mirrors, leads to the blocking factor.

The calculation of the shading factor requires the introduction of the Sun frame: in other words, heliostat vertices are projected on a plane perpendicular to the sun beams to compute their coordinates in the Sun reference frame. This change is possible when both the two reference frames are right-handed and made up of an orthonormal basis; beside that, the operation is easy when the transformation matrix, from Tower to Sun system, is known. Concerning the Tower system, it has been built by the vectors:

- East: $\vec{x} = (1,0,0)$
- North: $\vec{y} = (0,1,0)$
- Zenith: $\vec{z} = (0,0,1)$

so, naming TS the transformation matrix, its columns are the components of the unit vectors defining the Sun frame in the Tower frame. Naming the three unit vectors $\overrightarrow{s_1}$, $\overrightarrow{s_2}$ and $\overrightarrow{s_3}$, it can be stated that $\overrightarrow{s_3}$ coincides with the sun vector $\vec{s}$; the other two unit vectors can be derived from six equations.
$\overrightarrow{s_1}$ is a unit vector normal to $\vec{s}$ and contained in the horizontal plane East-North of the Tower frame:

$$\begin{cases} s_{11}^2 + s_{12}^2 + s_{13}^2 = 1 \\ s_{11} * s_x + s_{12} * s_y + s_{13} * s_z = 0 \\ s_{13} = 0 \end{cases}$$

The three chosen solutions of the system are:

$$s_{11} = \frac{-s_y}{\sqrt{s_x^2+s_y^2}} \qquad s_{12} = \frac{s_x}{\sqrt{s_x^2+s_y^2}} \qquad s_{13} = 0$$

The unit vector $\overrightarrow{s_2}$ is orthogonal to $\overrightarrow{s_1}$ and $\vec{s}$ and completes the right-handed coordinate system; it is the vector product of $\overrightarrow{s_1}$ and $\vec{s}$:

$$s_{21} = s_{12} * s_z = \frac{-s_z * s_x}{\sqrt{s_x^2+s_y^2}} \qquad s_{22} = s_{11} * s_z = \frac{-s_z * s_y}{\sqrt{s_x^2+s_y^2}} \qquad s_{23} = \sqrt{s_x^2 + s_y^2}$$

It is possible now to write down the transformation matrix *TS*:

$$TS = \begin{bmatrix} s_{11} & s_{21} & s_x \\ s_{12} & s_{22} & s_y \\ s_{13} & s_{23} & s_z \end{bmatrix}$$

The vertices of the heliostat *i* and of tower in the Sun frame are expressed by:

$$H_{Vi,S} = TS * H_{Vi,T}$$

$$T_{S,\theta_T} = TS * T_{T,\theta_T}$$

Thanks to the function *adjacent*, the closest n_{sb} heliostats to the heliostat *i* are singled out, thus saving a considerable computational effort while checking which elements are shading. Additionally, among this group, only the mirrors whose vertical coordinate in the Sun frame is smaller than the analyzed one's take part in the process.
The function checks if the considered mirror is shaded by the tower and the close heliostats: the time and the complexity required can significantly be reduced thanks to the Matlab-built-in function *polybool*, which is able to perform logical operation (as union or intersection) on polygons in a Cartesian coordinate system. The shaded area, i.e. the intersection between the projection of the heliostat *j* on the heliostat *i*, is cut off when exists. Once all possible interfering heliostats have been checked, the shading factor is represented by:

$$\eta_{sh} = \frac{A_{i,free\ sh,S}}{A_{h\ i,S}}$$

Where $A_{free\ sh,S}$ is the area that is not shaded and $A_{h\ i,S}$ is the total area of the heliostat *i,* both in the Sun frame. Now, who reads must consider that *polybool* works on plane, not on space, so it's necessary to calculate the third dimension of every single point of the final resulting polygon; in the Sun frame, the plane passing through the analyzed reflective surface is derived from three 3-D points belonging to it. The third unknown coordinate of the points of the final polygon, in the Sun frame, belongs to the mentioned plane as well. If the unshaded polygon is made up of *k* points, then they can be expressed back in the Tower frame by:

$$H_{Vi,S,free\ sh} = \begin{bmatrix} X_{P1} & X_{P2} & X_{P3} \dots & X_{Pk} \\ Y_{P1} & Y_{P2} & Y_{P3} \dots & Y_{Pk} \\ Z_{P1} & Z_{P2} & Z_{P3} \dots & Z_{Pk} \end{bmatrix}$$

$$H_{Vi,T,free\ sh} = TS^{-1} * H_{Vi,S,free\ sh}$$

The subindex "*free sh*" stands for shade-free.

Concerning the "blocking part" of the function, it is worth reminding that the sun vector $\vec{s}$ is the same throughout the entire field, whereas a unique reflected ray vector $\vec{r_i}$ characterizes each mirror. When the unshaded surface is projected along the reflected ray direction, there must be a different transformation matrix for each element considered. The argument employed to derive the matrix to switch to the Sun plane is again adopted; the change from the Tower to the Reflected Ray frame is realized by *TR*:

$$r_{11} = \frac{-r_y}{\sqrt{r_x^2+r_y^2}} \qquad r_{12} = \frac{r_x}{\sqrt{r_x^2+r_y^2}} \qquad r_{13} = 0$$

$$r_{21} = r_{12} * r_z = \frac{-r_z * r_x}{\sqrt{r_x^2+r_y^2}} \qquad r_{22} = r_{11} * r_z = \frac{-r_z * r_y}{\sqrt{r_x^2+r_y^2}} \qquad r_{23} = \sqrt{r_x^2 + r_y^2}$$

$$TR = \begin{bmatrix} r_{11} & r_{21} & r_x \\ r_{12} & r_{22} & r_y \\ r_{13} & r_{23} & r_z \end{bmatrix}$$

The points forming the unshaded polygon are transformed in the Reflected Ray coordinates, so:

$$H_{Vi,R,free\ sh} = TR * H_{Vi,T,free\ sh}$$

Again the command *polybool* quickly locates and cuts off the part of the area which is eventually blocked. Now, the imposed control regards the position of the heliostat *j* in the plane $r_1 - r_2$: only the mirrors whose vertical coordinate in the Reflected Ray frame is smaller than the analyzed one's take part in the process.
Once all the possible heliostats have been checked, the final polygon represents the part of surface which is actually reflected to the aim point. The blocking factor is defined as:

$$\eta_{bl} = \frac{A_{i,free\ bl,R}}{A_{i,free\ sh,R}}$$

where the numerator is the unblocked and unshaded fraction of reflective surface and the denominator the unshaded one, both calculated in the Reflected Ray frame.

Atmospheric attenuation: this function calculates the loss due to atmospheric attenuation carried out by scattering and absorption by air molecules and solid or liquid aerosols. As those phenomena are extremely difficult to model, a polynomial approximation is required. For a given site, the loss (in percent) is only function of the slant range, the distance between heliostat center of rotation from the aim point:

$$D_i = \sqrt{(T_x - X_i)^2 + \left(T_y - Y_i\right)^2 + (T_z - Z_i)^2}$$

$$a.a._i = 0.99321 - 0.0001176 D_i + 1.97 * 10^{-8} D_i^2$$

Obviously this equation is used just for sake of simplicity, as it doesn't take into account either different sky conditions. The reason is that the code has been written focusing more on a small heliostat field, where distances are small, rather than commercial-scale solar thermal power plants.

Spillage: this function provides the interception efficiency for the analyzed *i-th* heliostat. The script considers the whole reflective surface and not the unshaded and unblocked one because of the assumptions adopted. Moreover, the shading and blocking effect affects no more than the 5% of the mirror area in the average.

For a conventional receiver in the Northern hemisphere, the aperture is an oriented surface, whose direction is given by the three components of its normal unit vector $\vec{t}$:

$$t_x = 0$$

$$t_y = \frac{1}{\sqrt{1 + (\tan\gamma)^2}}$$

$$t_z = \frac{-\tan\gamma}{\sqrt{1 + (\tan\gamma)^2}}$$

The vector $\vec{t}$ is tilted downwards by an angle γ and lies in the plane North-Zenith.
In a variable-geometry central receiver system, $\vec{t}$ rotates around the origin of the Tower frame as the receiver does, in other synchronously with the Sun:

$$t_{x,rot} = \frac{-s_x}{\sqrt{{s_x}^2 + {s_y}^2 + ({s_x}^2 + {s_y}^2)\,(\tan\gamma)^2}}$$

$$t_{y,rot} = \frac{-s_y}{\sqrt{{s_x}^2 + {s_y}^2 + ({s_x}^2 + {s_y}^2)\,(\tan\gamma)^2}}$$

$$t_{z,rot} = \frac{-(\tan\gamma)\sqrt{{s_x}^2 + {s_y}^2}}{\sqrt{{s_x}^2 + {s_y}^2 + ({s_x}^2 + {s_y}^2)\,(\tan\gamma)^2}}$$

During the development of the function, a convolution method approach has been selected: reflected rays from the mirrors are considered with error cones. These are calculated by convolutions of normal Gaussians distributions corresponding to each error. Such method answers for the need of speed and accuracy required, especially remembering that this same function has to take part in the optimization process as well. Although it seems that convolution codes can find the interception efficiency with good agreement, their principal lack is the accuracy to predict the peak flux at the receiver (Garcia, et al., 2008), which, however, is not the objective of this thesis.

Assuming that canting gives to every heliostat a spherical curvature, the reflected image of each mirror is represented by a single circular normal distribution of the energy flux, function of the radial distance r:

$$F(r) = \frac{1}{2\pi\sigma^2}\, e^{-\frac{r^2}{2\sigma^2}}$$

$F(r)$ expresses how the image and the flux spread over the image plane. Actually, the size and the shape of this image also dependent on the finite size of the sun and the quality of mirror curvature and surface. Furthermore, the uncertainty due to the tracking mechanism should be evaluated, so as the astigmatic effect that degrades the image of the reflected beams when the sun rays don't fall almost parallel to the mirror normal. All the mentioned errors are supposed to be standard deviations of Gaussian distributions and are aggregated into a total standard deviation with one characteristic value σ (Schwarzbölz, 2008). The superposition of these distributions leads to:

$$\sigma^2 = \sigma_{sun}^2 + \sigma_{beam\ quality}^2 + (2\sigma_{track})^2 + \sigma_{astigm,i}^2$$

- Solar intensity is not distributed uniformly across the sun disc but decreases towards the edge. For sake of simplicity, a Gaussian distribution was selected instead of Kuiper sun shape model, thus overestimating the peak at the expense of the edges. The value used to represent the standard deviation at every run of this function is:

$$\sigma_{sun} = 2.51\ mrad$$

- The mirror curvature in not ideal and, at the same time, waviness and roughness affect the surface. The slope error accounts for these errors and as it is defined with respect

to the surface normal error, its effect is doubled in the reflected ray (Collado & Guallar, 2013):

$$\sigma_{beam\ quality} = 2\ \sigma_{slope}$$

- Tracking errors have their roots in the finite motor step size, tolerances of gear boxes and wind loads on the structure. The tracking error is usually measured with respect to the normal vector, so its effect is doubled in the reflected ray. Standard deviations concerning the two axes are combined together into one circular symmetric distribution.

$$\sigma_{axis\ 1} = 1\ mrad \qquad \sigma_{axis\ 2} = 0.5\ mrad$$

$$\sigma_{track} = \sqrt{\sigma_{axis\ 1} \cdot \sigma_{axis\ 2}}$$

- When an on-axis canted spherical concentrator reflects off-axis (angle of incidence $\theta \neq 0$), rays are concentrated into two focal lines rather than on a single point. Naming f the focal point, the tangential plane concentrates the rays at a distance $f \cos\theta$, the perpendicular sagittal plane at $f / \cos\theta$. Being D_i the slant range between the heliostat i and the aim point, and *dim* a general dimension of the mirror, the reflected image dimensions in the two planes are:

$$H_{t,i} = dim \left| \frac{D_i}{f} - \cos\theta \right| \qquad W_{s,i} = dim \left| \frac{D_i}{f} \cos\theta - 1 \right|$$

$$dim = \sqrt{l_h \cdot w_h}$$

Usually the heliostat is focused on its slant range, so $D_i / f = 1$. The root-mean-square of these image extensions is treated as an additional Gaussian distribution, which widens the reflected beam (Schwarzbölz, 2008):

$$\sigma_{astigm,i} = \frac{\sqrt{0.5\ ({H_{t,i}}^2 + {W_{s,i}}^2)}}{4 D_i}$$

Even if some assumptions may take to an inaccurate representation of the individual total standard deviation, it's worth keeping in mind that the Central Limit Theorem states that the superposition of a number of arbitrarily distributed quantities converges toward a normal distribution. The greater is the number, the faster is the convergence (Schwarzbölz, 2008).

The image and distribution has to be integrated over the receiver aperture plane in order to get the interception efficiency:

$$\eta_{int} = \frac{1}{2\pi {\sigma^2}_{rec}} \int_x \int_y \exp\left(-\frac{x^2 + y^2}{2\sigma^2} \right) dy\ dx$$

The fraction of the image that doesn't impinge the receiver is the spillage. Instead of solving the last integral in two dimensions, an easier way to approach the problem is by means of statistics. At a distance equal to the slant range the total individual standard deviation on the image plane is:

$$\sigma_{i,image} = \sqrt{{D_i}^2[\sigma_{sun}^2 + \sigma_{beam\ quality}^2 + (2\sigma_{track})^2 + \sigma_{astigm,i}^2]}$$

Because of astigmatism, the circular Gaussian distribution may be inappropriate, as the flux directed to the receiver plane tends to assume an elliptical rather than circular shape. In this case the radial power distribution of the flux image is of more concern, so it is necessary to find out the radial power distribution of an elliptical Gaussian flux image around the receiver center (Guo & Wang, 2011). The major and minor axes of the elliptical distribution are arbitrary defined as:

$$\sigma_{x-i,image} = \sigma_{i,image}$$

$$\sigma_{y-i,image} = \frac{\sigma_{i,image}}{\cos\theta_{i,rec}}$$

$\cos\theta_{i,rec}$ is the incidence cosine of the reflected ray from the heliostat on the receiver surface (Besarati & Goswami, 2014). The equivalent Gaussian flux distribution on the receiver plane is represented by the standard deviation $\sigma_{c,i}$:

$$\sigma_{c-i,rec} = \sqrt{\sigma_{x-i,image}^2 + \sigma_{y-i,image}^2}$$

It is good to keep in mind that, in this study, the cone error is applied only to the central reflected ray of each reflective element, which makes quite approximated the estimation of the interception factor.

Considering a circular aperture with radius R_{ap}, the image sent to the receiver by any heliostat has some probability to fall totally or partially within the range [$-R_{ap}$, $+R_{ap}$] with mean value 0, in vertical and horizontal dimensions. Thanks to the normal cumulative distribution function implemented in Matlab, it's possible to get the interception efficiency value for both single heliostat and the entire heliostat field.

Field efficiency and power at the receiver: this last part of the code calculates the efficiency of every single heliostat and of the entire solar field, the incident solar power on the field and the power conveyed to the receiver. Reminding that ρ is the reflectivity of the mirror, eventually corrected by a cleanliness factor f_{cl}, the instantaneous optical efficiency for the generic *i-th* heliostat is:

$$\eta_{opt,i} = \rho * \eta_{cos} * \eta_{sh} * \eta_{bl} * \eta_{a.a.} * \eta_{int}$$

The relation with the instantaneous power that impinges the receiver is immediate:

$$P_i = A_h * DNI * \eta_{opt,i}$$

where A_h is obviously the reflective area of the heliostat.

$$A_h = w_h * l_h$$

As the field is composed of *n* heliostats, the total power reaching the receiver is:

$$P_{rec} = \sum_{i=1}^{n} P_i = A_h * DNI \sum_{i=1}^{n} \eta_{opt,i}$$

On the other hand, the total incident solar power on the whole heliostat field is:

$$P_{incident} = n * A_h * DNI$$

The last two equations lead to the optical field efficiency:

$$\eta_{opt,field} = \frac{P_{rec}}{P_{incident}} = \frac{A_h * DNI \sum_{i=1}^{n} \eta_{opt,i}}{n * A_h * DNI} = \frac{\sum_{i=1}^{n} \eta_{opt,i}}{n} = \overline{\eta_{opt,i}}$$

The code has been verified several times at the CTAER with the local research group checking some field configurations; in addition it shows good agreement with the declared optical efficiency of the PS10 at the design point, even if in this case the influence of the tower in the shading and blocking efficiency is neglected. The following table summarizes PS10 data accessible on scientific literature and websites (Osuna, et al., 2006), (Romero-Alvarez M., 2007), (Noone, et al., 2012):

Table 6-1: PS10 data

Latitude	37° 26' N
Heliostat type	Sanlúcar 120
Heliostat number	624
Heliostat width	12.84 m
Heliostat height	9.45 m
Reflectivity	0.88
σ_{sun}	2.51 mrad
σ_{slope}	2.9 mrad
σ_{track}	0.71 mrad
Height of aperture center	110 m
Tilt angle	12.5°
Aperture width	14 m
Aperture height	12 m
Design point day	March 21
Design point DNI	0.9 kW/m^2
Design point hour (solar time)	12
Declared Design point optical efficiency	0.77

The only change to the parameters in Table 6-1 concerns the receiver aperture: the code supports circular apertures, but not rectangular ones because of the function linked to the interception efficiency. This particular forced to find an equivalent circular area, whose radius

is 7.3 m.
In this way, about 25 seconds are required to estimate the optical efficiency in 0.7543, a value that differs from the declared one of 2%.

7 Variable-Geometry Field Optimization

In the variable-geometry central receiver test facility of CTAER in Almería (Spain), the solar field is made up of some circular concentric rails with the tower stands in the central point. In every row, each heliomobile is free to move independently from the others, on condition that it keeps the security distance.
When a rotating receiver is coupled to this kind of field, it is essential to plan an operational strategy for the solar field, in order to maximize the optical efficiency and consequently the amount of energy sent to the receiver. The achievement of this result is far from being immediate, and it's reached under some hypothesis and within precise bounds.

The starting point is a solar field composed of 30 heliomobiles, arranged in 4 rows: 6 in the first, 7 in the second, 8 in the third and 9 in the fourth[1]. As the height of the tower and the tilt angle of the receiver are fixed, the objective would be the optimization of 30 variables for every possible value of the solar apparent position in the sky, but fortunately a few simplifications can be applied to the problem.

First of all, the idea is to express the position of the first heliomobile in each row as function of the angular distance from the symmetry axis of the field, represented by the vector $\overrightarrow{t_x} + \overrightarrow{t_y}$, i.e. the sum of the two components of the vector normal to the aperture surface of the receiver. The position of the *j-th* heliomobile with respect to the *i-th* one on the same row is obtained by a rotation movement. In the first row, for example:

$$H_0 = [0, R_{row1}, h_{pedestal}]$$

$$H_1 = \begin{bmatrix} \cos\varepsilon_{1,row1} & -\sin\varepsilon_{1,row1} & 0 \\ \sin\varepsilon_{1,row1} & \cos\varepsilon_{1,row1} & 0 \\ 0 & 0 & 1 \end{bmatrix} {H_0}'$$

$$H_2 = \begin{bmatrix} \cos\varepsilon_{2,row1} & -\sin\varepsilon_{2,row1} & 0 \\ \sin\varepsilon_{2,row1} & \cos\varepsilon_{2,row1} & 0 \\ 0 & 0 & 1 \end{bmatrix} H_1 \quad H_3 = \begin{bmatrix} \cos\varepsilon_{3,row1} & -\sin\varepsilon_{3,row1} & 0 \\ \sin\varepsilon_{3,row1} & \cos\varepsilon_{3,row1} & 0 \\ 0 & 0 & 1 \end{bmatrix} H_2$$

where H_0 it's the supposed "rest position" of the first heliomobile, $\varepsilon_{1,row1}$ its angular separation from the rest position to H_1, $\varepsilon_{2,row1}$ the angular distance between H_2 and H_1.
This means that it is enough considering half the number of the elements in the field, because the other half is just mirrored, thanks to the mentioned intrinsic symmetry.
In this case, the number of variables is 3 in first row, 4 in the second row, 4 in the third row and 5 in the fourth row. In the rows with an odd number of elements, also the central one must be added to the computation as it is the only non-symmetric element.
The variable choice could appear quite cumbersome, but the aim is to reproduce accurately the degrees of freedom offered by this innovative concept. Alternatively some other hypotheses can reduce substantially the number of unknown variables: indeed, a constant angular separation may be sought for each row, or even for the entire field.
Secondly, a variable-geometry heliostat field, unlike a fixed one, follows the apparent

[1] This prototypal field configuration has been developed at CTAER

movement of the Sun in the sky, so a new hypothesis can be added: the optical efficiency of the collector subsystem depends only on solar elevation α_s, while it's not subject to the variation of the azimuthal angle γ_s. If an observer stood in the symmetry axis of the field, he would notice the vertical change of position of the Sun and no one else.

The optimization process must undergo definite bounds, linked to the security distance between close elements in the same row and to the maximum angular distance of the last mirror in each row. This last condition does not to penalize both individual cosine and interception efficiencies.
Considering a generic heliomobile, naming R_{row} the radius of the rail, its dimensions are increased for security matters:

$$w_{h,safe} = 1.1\, w_h \qquad\qquad h_{h,safe} = 1.1\, h_h$$

$$dm = 2\sqrt{{w_{h,safe}}^2 + {h_{h,safe}}^2}$$

$$\tan\frac{\tau_{min}}{2} = \frac{dm/2}{R_{row}}$$

The lower bound for the unknown variable will be the safety angular distance τ_{min}, except for the first heliomobile of the row:

- For the rows with a pair number of elements it is $\tau/2$
- For the rows with an odd number of elements it is 0

In this way the symmetry is always guaranteed when the half of the field is mirrored to have the complete layout.
The upper bound for each unknown variable is $\tau_{MAX} = 30°$, supposed to be a suitable value. Finally, the last constraint is represented by a linear inequality, applied to every single row considered. If the half number of the heliomobiles is *k*, the linear inequality is:

$$\varepsilon_1 + \varepsilon_2 + \varepsilon_3 + \cdots \varepsilon_k \leq \mu_{row\,i}$$

where ε_n is the angular separation of the *n-th* heliomobile from the *m-th* one, and $\mu_{row\,i}$ is the angular distance of the last heliomobile of the half side from the symmetry axis, in the *i-th* row.

That said, the optimization problem is now reduced to find the best value for a $\vec{X}$ vector of 16 unknown variables, each one subject to a lower bound *LB* and an upper bound *UB*, while the whole vector must respect the linear inequality:

$$A\,\vec{X} \leq \vec{b}$$

being A a matrix whose dimension is number of rows x number of variables, and $\vec{b}$ a vector whose number of components equals the number of the rows in the field.
The approach selected looks for the $\vec{X}$ vector which maximizes the optical efficiency of the variable-geometry field as function of sun elevation α_s, besides the parameters introduced in the description of the simulation tool.

α_s is varied from 10° to 80°, with a step of 5°, and $\vec{X}$ optimizes $\eta_{opt,field}$ for the various values of α_s.

Nevertheless in a central receiver system it appears clear that the optical efficiency as function of solar position is strongly discontinuous, and consequently non-differentiable in many points. The characteristic makes very hard to find a global optima with exhaustive or random searches, analytical optimization and line minimization, respectively because of computation effort required, impossibility to calculate the gradient of the function in non-differentiable points, tendency to stick in local optima.
An alternative is represented by natural optimization methods: they generate new points in the search space by applying operators to current points and move towards more optimal points in the search space. Relying on an intelligent search in a large but finite solution space, thanks to statistics and some search operators, they don't need derivatives and gradients. In this way, such algorithms can deal with discrete variables and non-continuous functions.
Additionally, this path has been chosen as variable interaction in this problem is quite high: for example, the angular position of first heliomobile in the second row influences directly the one of the second and may shade or block a back mirror. In such condition, evolutionary algorithms perform best when compared to minimum seeking or random search algorithms.

7.1 Genetic Algorithm and Refining Search

Genetic algorithm (GA) is an optimization and search technique based on natural selection. Unlike more classical methods that generate a single solution point at each iteration, the GA creates a population of points (i.e. solutions) that evolves in order to find the best individual after some generations (i.e. iterations). Such individual represents the optimal solution.

At first the algorithm creates a random initial population of N_{pop}, taking into account the specified bounds. The population is seen like a set of chromosomes (solutions) which are composed of sixteen random numbers:

$$chromosome_i = (X_1, X_2, X_3, \ldots, X_{16})$$

Each one's worth is assessed by the value assumed by fitness function, i.e. $\eta_{opt,field}$, that is estimated through the written simulation tool dedicated to central receiver systems.

$$fitness_i = f(chromosome_i)$$

The algorithm now scores each member of the population by its fitness value and decides which chromosomes are fit enough to survive and reproduce offspring in the next generation by sorting them from the lowest to the highest fitness value. The natural selection takes place by saving only $N_{pop}/2$.
In some random way couples of mothers and fathers pair to form the next generation thanks to a crossover mechanism:

$$parent_1 = (X_{1d}, X_{2d}, X_{3d}, \ldots, X_{16d})$$

$$parent_2 = (X_{1m}, X_{2m}, X_{3m}, \ldots, X_{16m})$$

$$offspring_1 = (X_{1m}, X_{2m}, X_{3m}, \ldots, X_{16d})$$

$$offspring_2 = (X_{1d}, X_{2d}, X_{3d}, \ldots, X_{16m})$$

Above, crossover points are randomly selected and there the variables are simply exchanged; it should be noticed anyway that this method doesn't allow new information to be introduced. The "genes" of the parents are propagated to the next generations, just in different combinations: the offspring is a copy of the parents. Some interesting methods offer a way to combine genes of the two parents into new variables values in the offspring, but are not employed herein.
To avoid a fast convergence into local optima because of cycling around a definite set of solutions, mutation comes in help, forcing the algorithm to explore a greater space search. This happens by introducing changes, "mutations", in some variables of parent chromosome:

$$parent_1 = (X_{1d}, X_{2d}, X_{3d}, \ldots, X_{16d}) \rightarrow parent_1 = (X_{1d}, X_{2d}, X_{new}, \ldots, X_{16d})$$

The first generation is now complete and the second one can start, undergoing again the process of selecting mates, crossover step and mutation; in addition, a number of individual survives to the next generation because of elitism, a way to keep in the best chromosomes. This process of selection, crossover and mutation is continued until a fixed number of generations have elapsed or some form of convergence criterion has been met (Coley, 1999). The role of such criterion is here assumed by the "function tolerance": the algorithm runs until the cumulative change in the fitness function value is less than or equal to "function tolerance", over the allowed number of generations.

The parameters selected to run the genetic algorithm are:

- $N_{pop} = 150$
- $N_{generations} = 150$
- $N_{elite} = 5$
- Function tolerance = 10^{-3}

The population size is about ten times the number of variables, this value has been judged suitable because it permits a good exploration of the space search and at the same time it doesn't slow down too much the algorithm.
The function tolerance on the other hand is quite low because the genetic algorithm is not the only method to maximize $\eta_{opt,field}$. Evolutionary optimization in general is really good at navigating around large complex search spaces, finding near-optimal solutions, but not always quickly. So GA is employed to locate the "hills" of the function, leaving to another technique to climb the last steps. This means that the fittest individual in the final generation is the starting point for a search method.

The second algorithm, called *pattern search* (PS) starts at the last fitness value on the function surface, and creates a set of vectors $\{\vec{v_j}\}$ which are used to determine the points to search at each iteration: the scalar Δ^m multiplies each v_i.

$$\vec{d_i} = \vec{v_i}\,\Delta^m$$

Δ^m is called mesh size. Adding the set $\{\vec{d_j}\}$ to the point left by GA a mesh of points is created:

$$\{\vec{P_J}\} = \overrightarrow{X_{GA}} + \{\vec{d_J}\}$$

At each step the algorithm polls the points in the mesh by computing their objective function values (fitness value). If it finds one point having a greater (if maximization) objective value than the actual one, it shifts. The poll is declared successful and the operation is repeated from the new point. Vice versa, if the poll is unsuccessful and doesn't find any greater objective value in the mesh, the point doesn't change in the next iteration.
A key role is played by the mesh size, that changes every step; if the poll is successful Δ^m is multiplied by 2 in the next step, or by 0.5 in case of failure.
The polling method chosen creates a pattern that follows 2N directions, where N is the number of unknown variables (16 here); the alternative option would have been a pattern of N+1 directions. However, because of the many local minima, the search through a wider solution space was favored.
The algorithm stops after a number of iterations or a time limit or if the change in the objective function in two consecutive iterations and the mesh size are both less than the function tolerance.

There is no way to know if the combination of these two algorithms leads effectively to a global optimum, but at least it guarantees a good trade-off between exploration of the space search and solution met.

Both the methods are included in the Global Optimization Toolbox of Matlab, which allows enough customization in defining initial population, parent selection, crossover, mutation functions for GA and polling and searching for PS. It has to be noticed that the algorithms in this Toolbox find the minimum of the objective function, so that the sought objective value actually is $-\eta_{opt,field}$.

7.2 Optimization Inputs and Results

The process of efficiency maximization was realized as function of the solar elevation α_s. During the fifteen runs, one each angular step, the inputs were:

$slope$ =	0°	b_t =	13.85
n_{rows} =	4	h_t =	57.7 m
$n_{h/row}$ =	[6, 7, 8, 9]	R_{ap} =	2.5 m
R_{rows} =	[44.5, 63.5, 81.5, 99.5] m	w_r =	8.22 m
τ_{MAX} =	30°	h_r =	6 m
μ_{row} =	[65°, 60°, 60°, 60°]	ρ =	0.95
n_{sb} =	15	f_{cl} =	0.95
w_h =	12.88 m	σ_{sun} =	2.51 mrad
h_h =	9.485 m	σ_{slope} =	2.9 mrad
h_{ped} =	6 m	σ_{track} =	0.71 mrad

The table down reports the results and the time required by the two algorithms:

Table 7-1: obtained efficiencies and time required

α_s (°)	$\eta_{opt,field,GA}$	$\eta_{opt,field,PS}$	t_{GA} (s)	t_{PS} (s)
10	0,5899	0,6015	6271	952
15	0,6810	0,7012	6163	1002
20	0,7470	0,7700	6043	1433
25	0,8018	0,8075	5658	675
30	0,8342	0,8366	5929	707
35	0,8459	0,8464	5486	218
40	0,8488	0,8512	5628	533
45	0,8468	0,8475	5347	652
50	0,8499	0,8509	5314	265
55	0,8433	0,8464	5355	587
60	0,8414	0,8419	5657	88
65	0,8429	0,8433	5596	129
70	0,8341	0,8362	5569	298
75	0,8246	0,8268	5617	464
80	0,8129	0,8150	5587	376

At a first glance, in most cases PS cannot succeed in increasing the optical efficiency substantially and it quickly ends, on the other hand GA seems to find a good optimum at the expense of time-consuming computation. The reason might be that PS starts when it is already too close to the "hill", where it gets entrapped.

Some changes in the structure of the two algorithms could help in decreasing the time needed, maybe finding higher optima. In GA, a different crossover function would extend the search space, while a lower tolerance could end up with opening the way to PS earlier. This should be combined in PS with mesh expansion and, in parallel, with a complete poll: the search zone would be wider, but the algorithm should check all possible patterns before declaring the poll successful or not.

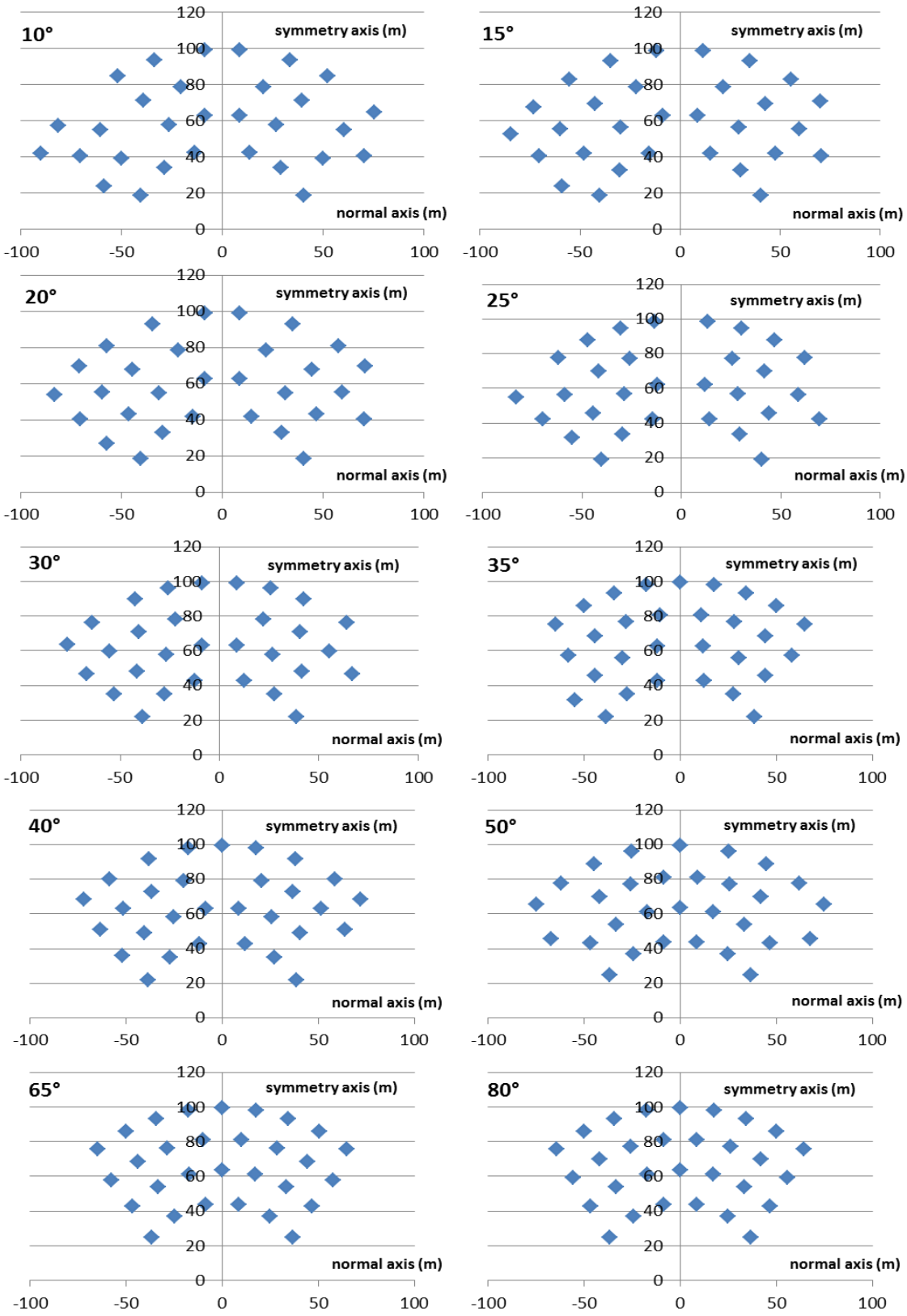

Figure 7-1: optimal configurations for variable-geometry field. Vertical and horizontal axes are respectively the symmetry axis and its normal, both in meters. The symmetry axis rotates during the day, according to the angular speed of the Sun.

As there is no certainty whether the result is a local or global maximum, the optical efficiency for each field configuration is calculated again in the range α_s= [10°, 80°], with 1°-step, in order to understand which type, among the fifteen ones, is the most adequate for every circumstance.
From the analysis only eight field configurations give the best efficiencies in the considered range, emphasizing the local nature of the found solutions. The estimate of annual efficiency, energy conveyed at the receiver and energy losses is carried on with them.

Figure 7-1 shows how the optimization process drives to fields that may differ much from each other: this is the very objective of the work indeed. The collector subsystem adapts itself to convey the highest amount of concentrated power to the aperture, but, depending on the time of the day, it might mean looking for the right trade-off between different forms of energy losses.
Early in the morning or late in the afternoon, at low α_s values, the overall optical efficiency could be penalized especially by shading and blocking, as the mirrors cast a long shadow behind them. The angular separation between the heliomobiles widens, so the higher $\eta_{sh\ \&\ bl}$ balances a reduced cosine factor and a higher spillage. It should be noticed also that till $\alpha_s = 35°$ the rows filled with an odd number of elements lose their symmetry: this particular does not mean that the vector of solutions found is a local optima, but rather that the shadow of tower stretches out the mirrors from the symmetry axis.
Vice versa, at high α_s values, the field is extremely compact and the only factor that determines the separation between the elements of a same row is the safety distance.

Based on the previous analysis, during the normal operation time, this optimization method suits an open-loop tracking system; the instant position in the field of each heliomobile, so as its inclination, would be determined by elevation and azimuth, calculated by an internal algorithm.

Subsequently, the optimal field configurations have been computed in the hypothesis of R_{ap} = 1.145 m, a lower radius of the aperture that would guarantee lower convective and radiative losses; starting from the fifteen initial configuration, the optical efficiency is again a function of α_s.
It is now possible to draw the two curves: the graphic in figure 7-2 clearly illustrates that the optical efficiency is approximatively constant when $\alpha_s \geq 30°$.
The explanation of the initial and final slopes lays above all in the cosine factor, early in the morning it is quite high because the field spreads to keep modest reciprocal interactions between the heliomobiles: the wider the field, the more relevant the cosine energy loss. On the contrary, when $\alpha_s \geq 65°$, the angle of incidence becomes larger as the mirror has to tilt more its surface, being fixed the height of the aim point.

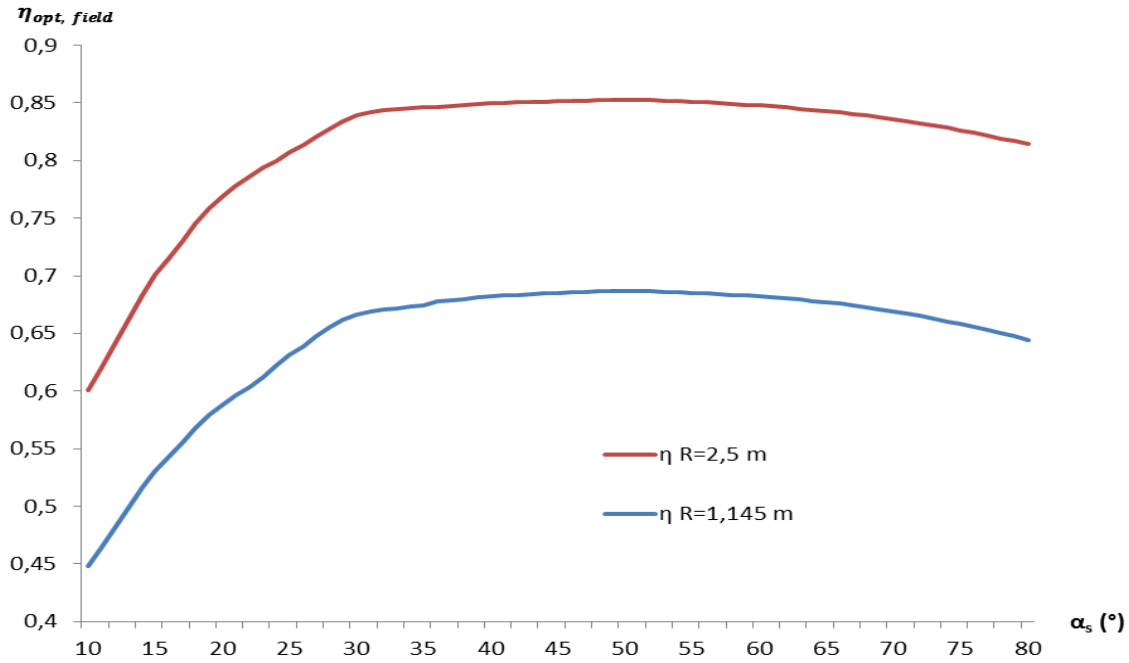

Figure 7-2: optical efficiency of the optimized variable-geometry field

8 Insolation Data and Comparisons

8.1 Facility Location and Solar Radiation Data

The CTAER (Centro Tecnológico Andaluz de Energías Renovables) is a research center specialized in the field of renewable energies whose headquarters are located in the Desert of Almería, in front of the Plataforma Solar de Almería (PSA).
There, the prototypal facility plant is under construction and, at present, consists of a steel tower, still lacking of receiver, and 13 heliomobiles arranged into two rows: six on the first and seven in the second.

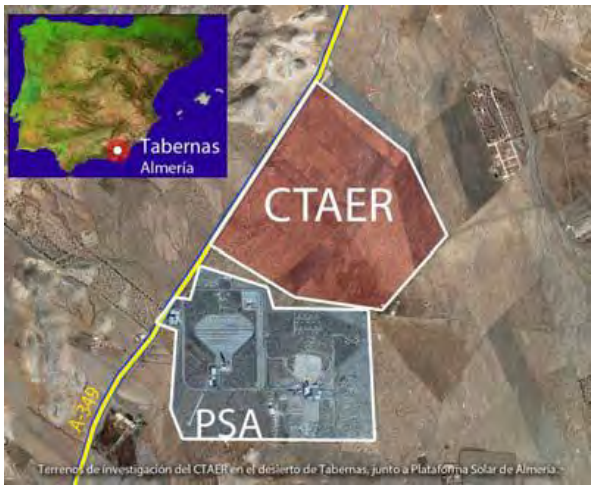

Figure 8-1: CTAER location

AICIA (Asociación de Investigación y Cooperación Industrial de Andalucía) joins the project through the GTER (Grupo de Termodinámica y Energías Renovables), which is experienced in prediction and measurement of solar radiation and modelling of CSP plants.

As radiation data of Almería delivered to the CTAER are confidential, data concerning Seville have been used in this work. A clear sky model was chosen as it fits better the objective of the study than the alternative represented by the TMY (Typical Meteorological Year). The two reasons that support this choice are determined by the fact that southern European regions are sites that rarely have extended periods of cloudy, overcast or hazy weather, so that cloudless sky is not far from reality. Secondly, the clear sky model allows to fully evaluating the potentiality of the system, especially when different solar field types are compared.
Solar radiation in Seville differs partially from the one in Almería and this is mainly due to atmospheric conditions and environment. CTAER facility is placed in a desert 30km far from the sea, implying a slightly larger number of sunny hours over the year but moreover a stronger atmospheric attenuation, because of dust and aerosols in suspension. The principal difference between the clear-sky curves of the two localities is represented by the peak reached by the DNI, more marked in the Andalusian capitol.

Among the number of clear-sky models published in specialized literature, herein it is employed the "AB model" proposed and validated by Manuel Silva Pérez (Silva, 2002). Such model is based on Kastrov's formula, modified by the introduction of a second parameter in order to reproduce DNI temporal evolution:

$$I_{clear\ sky}(t) = I_{CS} * E_0 * \frac{A}{1 + B\ m_R(t)}$$

$m_R(t)$ is the relative air mass, I_{CS} the solar constant and E_0 the Earth-Sun correction; A accounts for the strongest absorption processes that take place in some spectrum bands, while B for dispersion phenomena. In order to determine A and B, 544 clear days have been selected, thus limiting as most as possible the influence of clouds and aerosols. The very drawback of this model is that it is a local clear-sky model.

Air mass refers to the optical path length through the atmosphere where light is scattered and absorbed; atmospheric attenuation of solar radiation is not the same for all wavelengths, so the solar spectrum also changes with air mass, which changes during the day. This fact is due not to a variable atmosphere composition, but only to the length of the path that sunlight has to go through. Relative air mass is measured relative to the path length at the zenith.
The model employed evaluates m_R with a 10-minutes step and then integrates the obtained results between two halves hours in order to have hourly data. For example the DNI associated to 11 is the integration of the contribution calculated between 10.30 and 11.30. Calling ξ the zenith angle (incidence angle relative to the normal to the Earth's surface), the Kasten and Young formula (Kasten & Young, 1989) provides an accurate result of ξ up to 75°:

$$\xi = \frac{\pi}{2} - \alpha_s$$

$$m_R(t) = \frac{1}{\cos\xi(t) + 0.50572\ (96.07995 - \xi(t))^{-1.6364}}$$

Where obviously ξ changes according to the instant of the day considered.

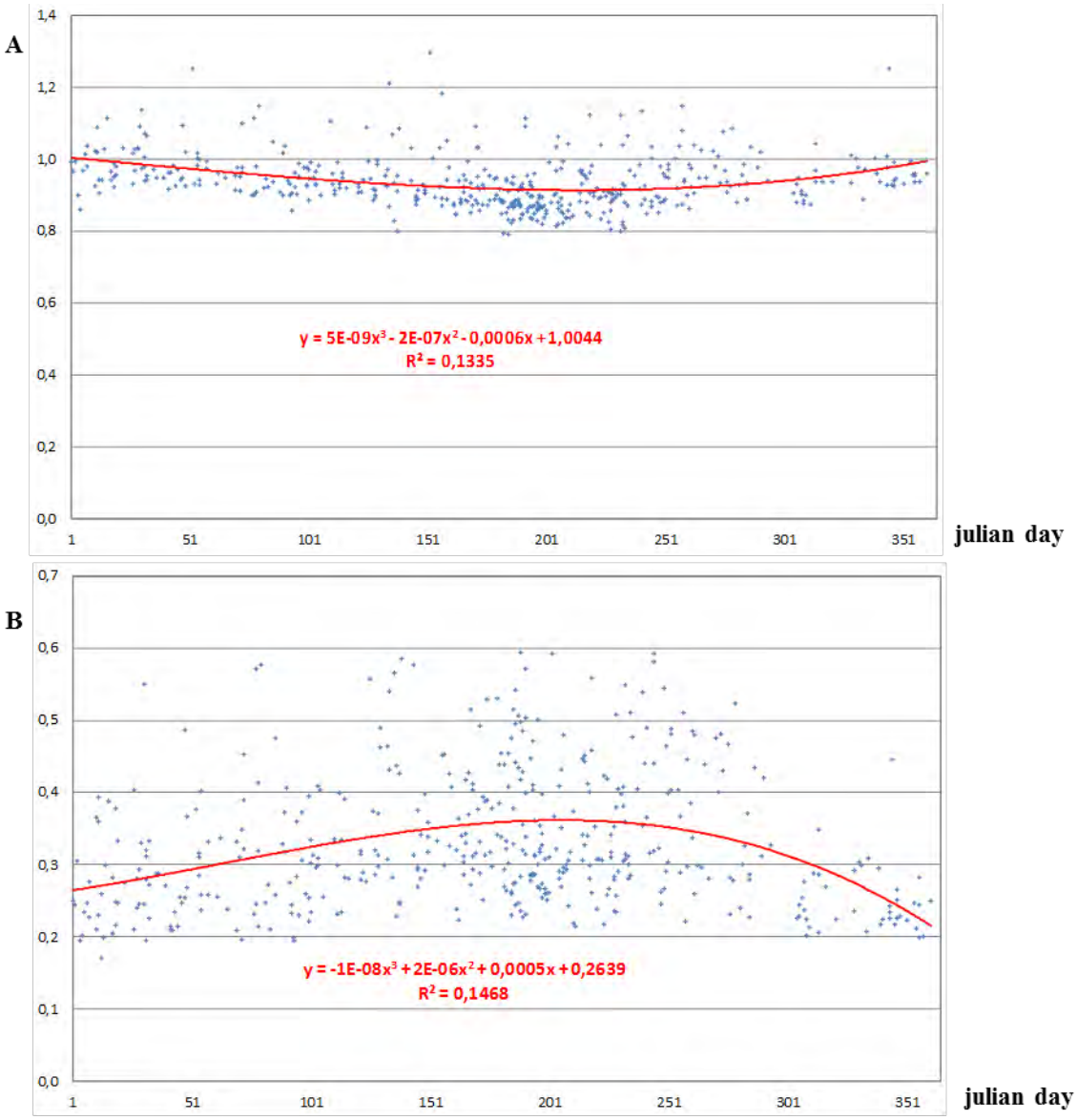

Figure 8-2: A and B as function of the Julian day of the year

8.2. Comparative Collector Fields

In order to fully evaluate the potential of the optimized variable-geometry field, it was compared with other two field types: a non-optimized variable-geometry field and spiral-layout field. The objective is to observe the major benefits that derive from the variation of the individual position of each element in the subsystem. The comparison is carried on with the same number of reflective elements, the same receiver aperture and the same site.

8.2.1. Non-Optimized Variable-Geometry Field

Starting from the hourly radiation data, the best configuration among the available ones was sought. They were sorted according to the best efficiency weighted on the cumulated DNI at every elevation angle:

$$\eta_{weight} = \frac{\sum_{\alpha_s=10°}^{\alpha_{s,max}} \eta_{VG}(\alpha_s) * DNI_{cumulated}(\alpha_s)}{\sum_{\alpha_s=10°}^{\alpha_{s,max}} DNI_{cumulated}(\alpha_s)}$$

The best field type is the one which maximizes the optical efficiency of the dynamic field for $\alpha_s = 30°$. Thus, it's supposed that the collectors move from West to East, following the apparent movement of the Sun during the daytime. Now their positions are permanent with respect to the symmetry axis of the field.

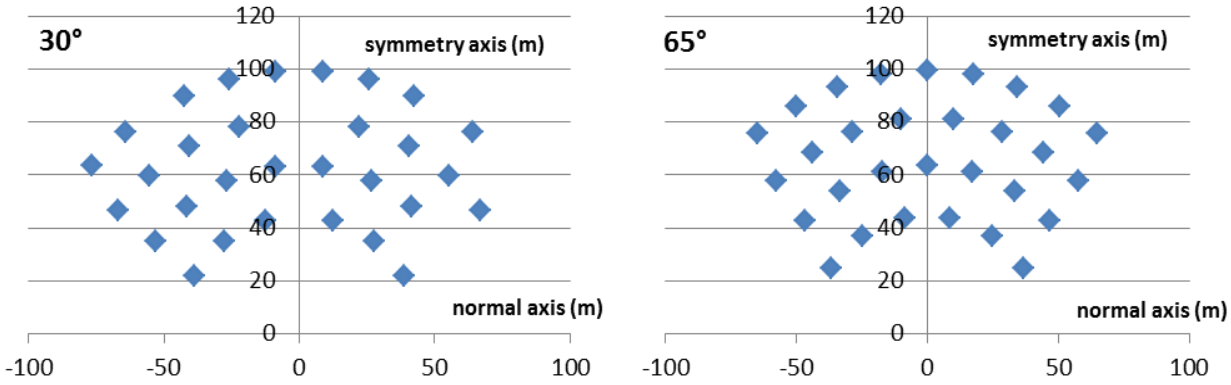

Figure 8-3: non-optimized variable-geometry fields used for comparative purposes. Vertical and horizontal axes are respectively the symmetry axis and its normal, both in meters. Left and right deployments are adopted respectively when aperture radius is R_{ap} = 2.5 m and R_{ap} = 1.145 m

8.2.2. Biomimetic Spiral Field

A spiral field has been chosen as term of representative comparison for static fields. The biomimetic layout seems able to achieve, at least in theory, the highest optical efficiency on land occupied. It is characterized by a continuous and monotonic heliostat density function which allows placing more mirrors in higher efficiency locations, without the drawback of strong shading and blocking losses (Noone, et al., 2012).
The *i-th* element of the subsystem is disposed at a radial and angular distance r_i and θ_i from the tower:

$$r_i = a\, i^b$$

$$\theta_i = 2\pi\varphi^{-2} i \qquad \varphi = \frac{1+\sqrt{5}}{2}$$

where φ is the golden ratio, a and b two parameters that rules the growth of the spiral pattern. The values of these two coefficients are borrowed from (Noone, et al., 2012), where the PS10 was redesigned according to the here discussed layout.

To accomplish this goal, a matrix of radiation data must be available. As a matter of fact, the final pattern is made up by the heliostats which send the highest amount of energy over the year. The annual incoming radiation is expressed by the hourly data of twelve representative days, one for each month; additionally each month has nh_j hours of sunshine. Only hours with $\alpha_s \geq 10°$ have been considered.

Table 8-1: monthly radiation data

n_{day}	DNI_{hourly} (KW/m^2)													nh_j
21			627.3	845.8	952.1	1003.1	1018.5	1003.1	952.1	845.8	627.3			152.8
52			741.9	891.2	968.8	1007.3	1019	1007.3	968.8	891.2	741.9			175.2
80		603.2	806	911	968.7	998.1	1007.2	998.1	968.7	911	806	603.2		212
111		692.9	828.2	904.6	948.7	971.7	978.9	971.7	948.7	904.6	828.2	692.9		221
141	533.6	719.7	824.3	886.6	923.5	943.2	949.4	943.2	923.5	886.6	824.3	719.7	533.6	256.9
172	556.4	719.4	814.1	871.6	906.1	924.6	930.5	924.6	906.1	871.6	814.1	719.4	556.4	314.3
202	522.4	703.6	806.1	867.4	903.9	923.3	929.4	923.3	903.9	867.4	806.1	703.6	522.4	395.7
233		664.2	795.3	869.8	912.9	935.5	942.6	935.5	912.9	869.8	795.3	664.2		336.2
264		574.7	766.4	866.9	922.3	950.7	959.5	950.7	922.3	866.9	766.4	574.7		238.5
294			702.6	846	920.5	957.5	968.8	957.5	920.5	846	702.6			190.8
325			607.2	813.8	913.4	960.9	975.2	960.9	913.4	813.8	607.2			135.8
355				836.4	947.9	999.5	1014.8	999.5	947.9	836.4				160.6
	6	7	8	9	10	11	12	13	14	15	16	17	18	

This method is taken by (Collado & Guallar, 2013), (Collado & Turégano, 1989), (Pitz-Paal, et al., 2011), which recommends it for optimization purposes, although they had to deal with a large central receiver system, with thousands of heliostats. In such case some simplifying hypothesis can substantially reduce the computational time.

The parameters that characterize the field are the same employed during the optimization:

$slope =$ 0°
$w_h =$ 12.88 m
$h_h =$ 9.485 m
$h_{ped} =$ 6 m
$a =$ 4.65
$b =$ 0.65
$n_{sb} =$ 15
$\gamma =$ 36.6°
$b_t =$ 13.85 m
$h_t =$ 57.7 m
$R_{ap} =$ 2.5 m and 1.145 m
$w_r =$ 8.22 m
$h_r =$ 6 m
$\rho =$ 0.95
$f_{cl} =$ 0.95
$\sigma_{sun} =$ 2.51 mrad
$\sigma_{slope} =$ 2.9 mrad
$\sigma_{track} =$ 0.71 mrad

The three aforementioned equations in the paragraph are used to draw a field larger than the expected size, but only the positions that respect the following constrains are saved, not to neglect the safety distance between the mirrors:

$$Y_i > 25\ m$$

$$\sqrt{{X_i}^2 + {Y_i}^2} \geq 25\ m$$

Next, all candidate locations are sorted by the average cosine efficiency, calculated in each instant of time sampled; the best ninety are selected to form a field three times larger than the final size.
The following step entails the calculation of the complete optical efficiency at each time step for each *i-th* element, as it gives the individual power sent to the receiver during the *k-th* hour:

$$P_{i,k} = DNI_k\ \eta_{i,k}$$

Naming nd_j the number of the hours in the representative month j and Δt_k the hourly time step, the average daily DNI of the *j-th* month is:

$$\overline{DNI_j} = \frac{\sum_{k=1}^{nd_j} DNI_k\ \Delta t_k}{nd_j}$$

The average of the instantaneous power sent by the *i-th* heliostat over the representative day is derived by the equation:

$$\overline{P_{i,j}} = \frac{\sum_{k=1}^{nd_j} P_{i,k}}{nd_j}$$

and its annual efficiency is:

$$\eta_{year,i} = \frac{\sum_j \eta_{i,j} * \overline{DNI_j} * nh_j}{\sum_j \overline{DNI_j} * nh_j}$$

The solar field is finally composed by the 30 heliostats ranked with the highest optical efficiency and the ensuing pattern is:

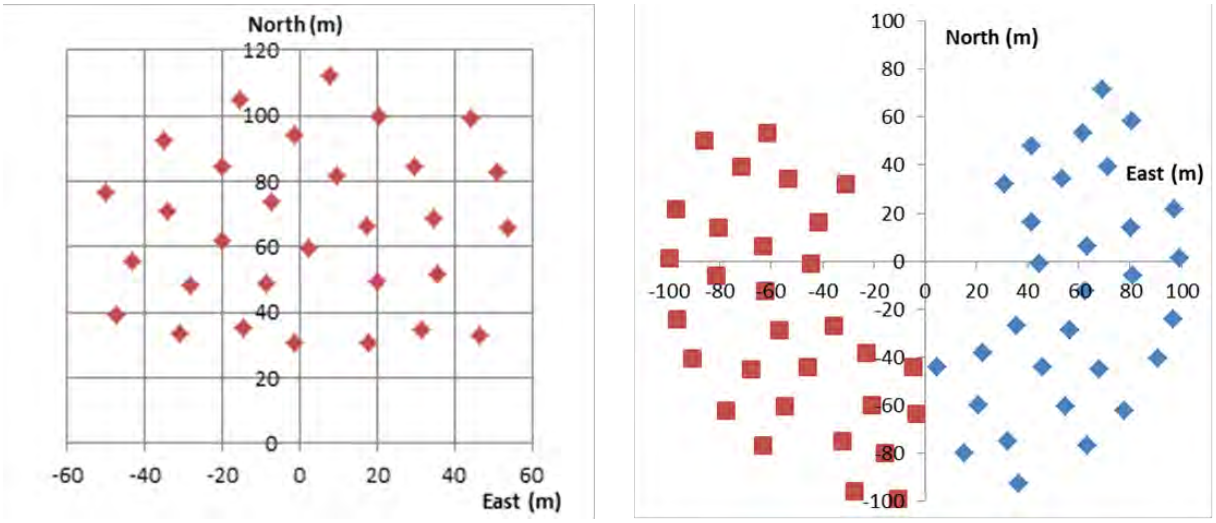

Figure 8-4: left, biomimetic layout of comparative static field; right West-side field at 6 (solar time), and East-side field at 18 (solar time) on 21/6

The first feature that might be appreciated is the non-symmetry of the field, as the polar angle of the heliostat is related to the irrational golden ratio φ. There is no element in the system that shares with another the same angular distance from the tower, thus making shading and blocking more localized, when they occur. Later, the other difference with the radially staggered pattern is land occupation. At present, it is reputed as one of major drawbacks for central receiver systems, and the same can be affirmed for the variable-geometry one here analyzed as well.
The issue is clarified by a fast assessment; the area of the convex hull of the set of heliostat positions plus the tower is:

$$S_{biomim} = 8208.5\ m^2$$

while the area occupied by the variable-geometry field in the condition of maximum coverage is given by the circle enclosed in the furthest rail from the tower:

$$S_{VG} = \pi\ R_{row,4}^2 = 31102.6\ m^2$$

Such condition derives from field movement on 21/6, when at 6 and 18 hours (solar time) the Sun describes the widest azimuthal angles (absolute value 109.13°). Mirror disposition in the two instants of the day is illustrated in the figure down, where the red and the blue dots stand respectively for morning and afternoon disposition.

8.3. Comparative Analysis

Yearly, monthly and daily comparisons between the three field types have been realized to analyze what benefits this new concept might produce in concentrating solar power at the receiver. Thanks to the limited number of reflective elements, reported data are deduced from hourly simulation and, for sake of simplicity, each sampled DNI is supposed to remain constant throughout the hour considered.
During the paragraph, optimized variable-geometry field, non-optimized variable-geometry field and spiral field are referred to as VGO, VGN and BF.

Yearly analysis involves a number of items, as the next table shows; the most important ones appear the annual weighted efficiency and the amount of energy conveyed to the aperture, defined as:

$$\eta_{year,w} = \frac{\sum_{day=1}^{365}\sum_{h=1}^{nh} DNI_h\,\eta_{opti,field,h}\,\Delta t_h}{\sum_{day=1}^{365}\sum_{h=1}^{nh} DNI_h\,\Delta t_h}$$

$$E_{rec} = \sum_{day=1}^{365}\sum_{h=1}^{nh} DNI_h\,\eta_{opti,field,h}\,\Delta t_h$$

where Δt_h is the time step of one hour, DNI_h the intensity of direct solar radiation in the hour considered, $\eta_{opti,field,h}$ the efficiency of the field in the hour of the day considered and nh the number of hours of the day.
The unweighted efficiency is simply:

$$\eta_{year,uw} = \frac{\sum_{day=1}^{365}\sum_{h=1}^{nh} DNI_h\,\eta_{opti,field,h}\,\Delta t_h}{\sum_{day=1}^{365}\sum_{h=1}^{nh} \Delta t_h}$$

and the mean of the various efficiency factors, together with the associated energy losses, complete the chart:

$$E_{loss} = \sum_{day=1}^{365}\sum_{h=1}^{nh} DNI_h\,(1-\eta_{loss,h})\,\Delta t_h$$

R_{ap} = 2.5 m	VGO	VGN	BF
$\eta_{weighted}$	0,811	0,801	0,727
$\eta_{unweighted}$	0,803	0,792	0,710
η_{cos}	0,960	0,961	0,889
η_{shadow}	0,969	0,952	0,928
$\eta_{blocking}$	0,987	0,991	0,988
atm attenuation	0,982	0,982	0,983
reflectivity	0,903	0,903	0,903
$\eta_{interception}$	0,987	0,987	0,973
$E_{incident}$ (MWh)	11653	11653	11653
$E_{receiver}$ (MWh)	9447	9339	8478

E_{cos} (MWh)	445	448	1159
$E_{s\&b}$ (MWh)	433	549	834
$E_{atm\ att}$ (MWh)	209	209	200
$E_{reflect}$ (MWh)	1136	1136	1136
$E_{spillage}$ (MWh)	147	153	267

What immediately comes to light is the different amount of concentrated energy throughout the year: the optimized variable-geometry system achieves the 10,3% more than the static one, taking advantage of the lower E_{cos}. and $E_{s\&b}$ and testifying the intrinsic benefits of the innovative concept. Both VGO and VGN have lower spillage losses as well, due to the constant flux image shape at the receiver plane: early in the morning and late in the afternoon BF is penalized by the excessive spread of such image as the average cosine angle is not negligible. Furthermore, the optimization of heliomobile positions puts VGO at the head of the group because of continue variations in the field that limit optical interactions between the elements at low sun elevation angles, although this goes to the detriment of cosine efficiency.

The same table is now filled with data coming from the same yearly simulation, but considering a lower aperture radius.

R_{ap} = 1.145 m	**VGO**	**VGN**	**BF**
$\eta_{weighted}$	0,631	0,624	0,568
$\eta_{unweighted}$	0,625	0,616	0,550
η_{cos}	0,962	0,967	0,889
η_{shadow}	0,965	0,935	0,928
$\eta_{blocking}$	0,986	0,989	0,988
atm attenuation	0,982	0,982	0,983
reflectivity	0,903	0,903	0,903
$\eta_{interception}$	0,768	0,776	0,745
$E_{incident}$ (MWh)	11653	11653	11653
$E_{receiver}$ (MWh)	7355	7269	6615
E_{cos} (MWh)	426	376	1159
$E_{s\&b}$ (MWh)	487	752	834
$E_{atm\ att}$ (MWh)	209	209	200
$E_{reflect}$ (MWh)	1136	1136	1136
$E_{spillage}$ (MWh)	2688	2611	2849

In the second case the optical efficiency decreases in all the systems, but the VGO is pointing out again the best result. The difference in energy yield is the 10,9%, when it is compared with the BF. Speaking about interception efficiency, every field suffers for a dramatic increase of spillage losses: the smaller aperture tends to favor dynamic fields, where the receiver is able to move synchronously with the sun. Compared to the previous table, the configuration used for VGN is more compact, as witnessed by the increased shading and blocking losses.

A few more comments appear useful. In the second table all the rows and all the columns were reported again to underline that also η_{cos}, η_{shadow} and $\eta_{blocking}$ underwent changes. This

particular does not find its roots neither in the code nor in the different radius of the receiver; the reason is simply that the field configurations which fits best this second case are not equal to those extrapolated when R_{ap} = 2.5 m. Furthermore the low weighted annual efficiency of the second table is not strictly linked to the aperture radius, but rather to the row deployment of the heliomobiles in the moving fields and to the proximity of the heliostats to the tower in BF. Such efficiencies would be higher if the 30 reflective surfaces in variable-geometry field were arranged on more rails, or if the spiral field was more stretched along North axis.
What emerges from the comparison between VGO and VGN is that the performances of the two fields are approximately equal; so that monthly and daily comparisons are carried on to evaluate their behavior in detail.

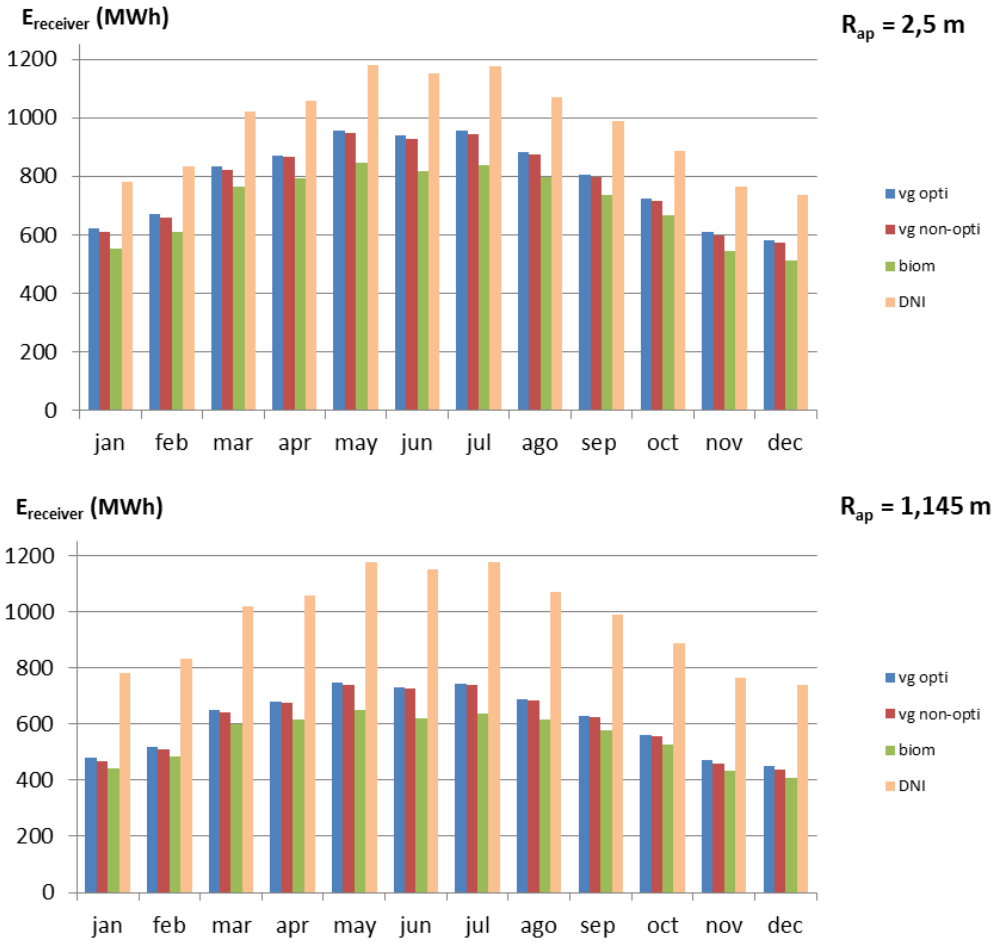

Figure 8-5: monthly comparison

Observing the two graphics they both stresses that the BF loses the challenge especially during the central months and this makes sense because that is the period in which the Sun covers the widest apparent path in sky. There, the two dynamic fields yields inevitably more, not being sensitive to the variations of solar azimuth. Once more, there is no appreciable difference between VGO and VGN (≈ 1%).

In the daily analysis four days were selected, 21st of January, 21st of March, 21st of June and 21st of December: as a matter of the facts, there is symmetry of the sun position and its direct

intensity with respect to the summer solstice, only December seems to depart from such symmetry and, therefore, is included (Collado & Guallar, 2013).

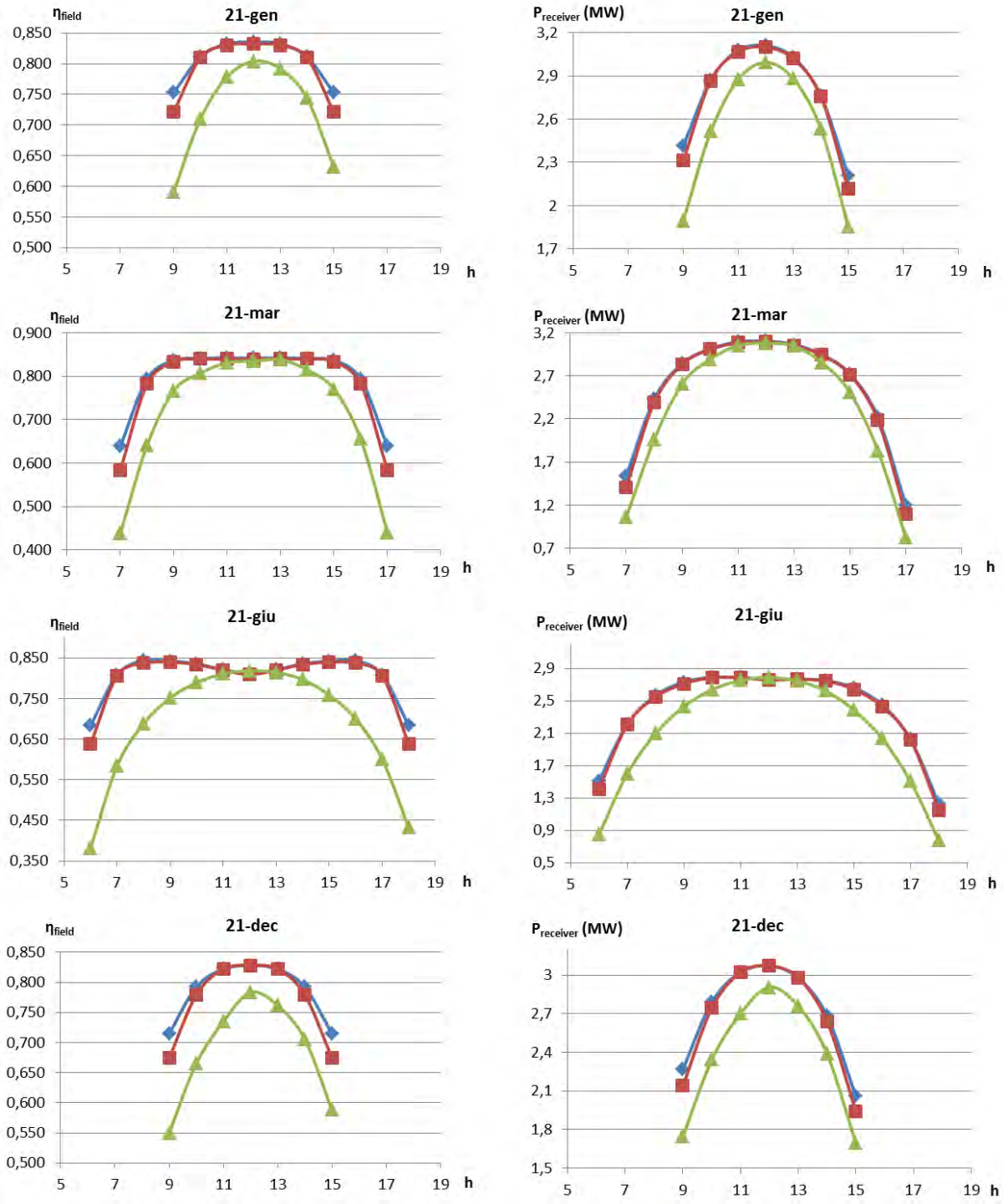

Figure 8-6: daily comparison for R = 2.5 m. In blue VGO, in red VGN, in green BF

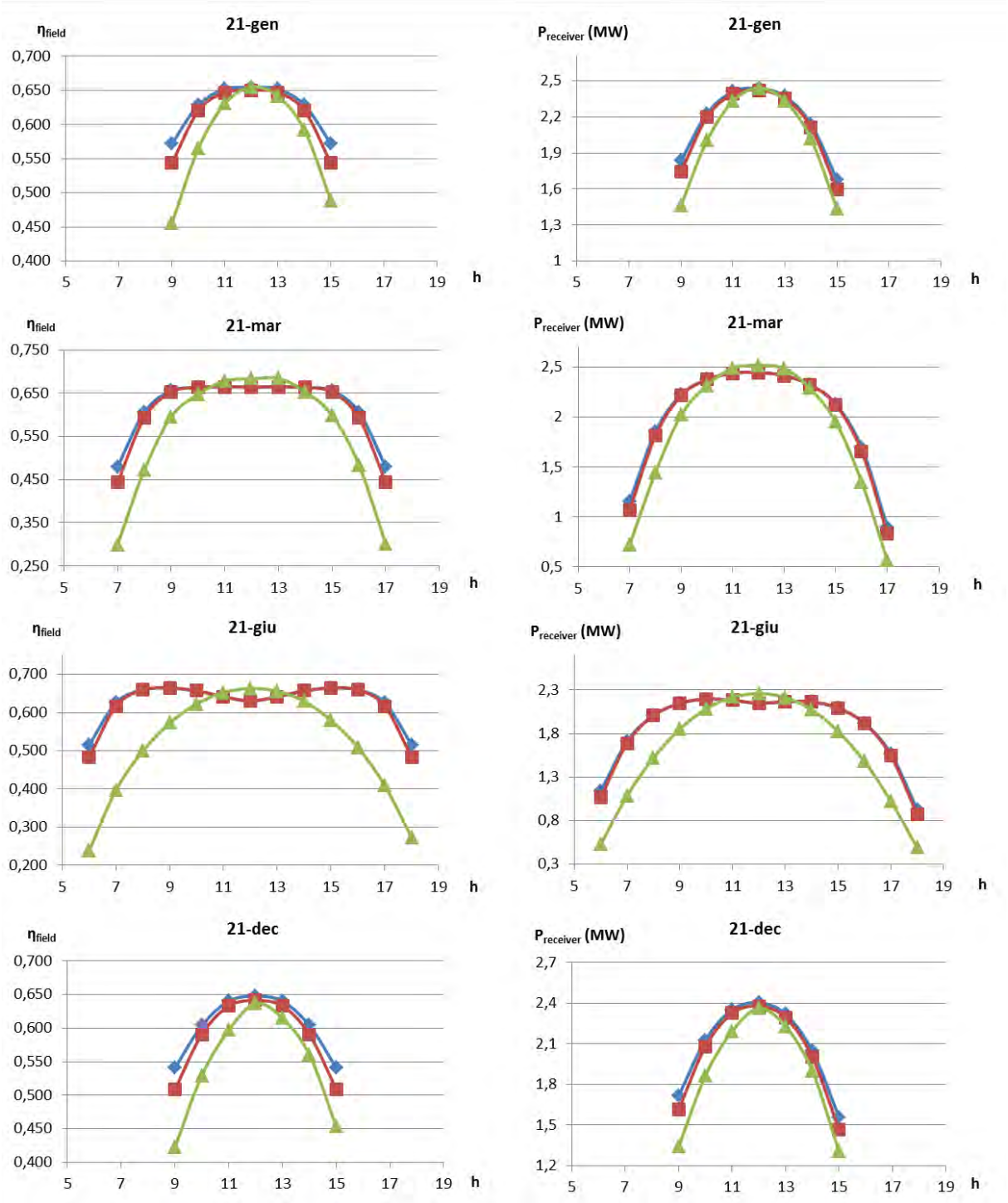

Figure 8-7: daily comparison for R = 1.145 m. In blue VGO, in red VGN, in green BF

The useful energy reaching the receiver is given by the integration of the power over the operation hours:

Table 8-2: daily comparison

R_{ap} = 2,5 m	VGO	VGN	BF	Δ%
21-gen	19475	19241	17546	9,90
21-mar	28160	27799	25705	8,72
21-giu	31247	30950	27214	12,91
21-dic	18875	18539	16537	12,38

R_{ap} =1,145 m	VGO	VGN	BF	Δ%
21-gen	15098	14812	14018	7,16
21-mar	21967	21715	20155	8,25
21-giu	24358	24184	20648	15,23
21-dic	14523	14162	13196	9,14
	$E_{receiver}$ (kWh)			

where Δ% is the percent yield obtained by VGO with respect to BF:

$$\Delta\% = \frac{E_{VGO} - E_{BF}}{E_{VGO}} * 100$$

During winter time (December and January), variable-geometry fields are able to convey to the receiver a power level that is significantly more constant than the one observed in the BF: the percent gain is remarkable, above all remembering that they are obtained in the period with the fewest sunny hours. The cause is without any doubt by the high optical efficiency even in the first morning so as in the late afternoon.

Looking at the graphics, the trend is verified also during 21/3, but it's during 21/6 that the dynamic fields outperform the static one, yielding the 15% more of energy. When Rap =1,145 m, at low solar elevations the quotient between VGO and BF optical efficiencies is about two, leading to a similar ratio between powers.

In general, the four analyzed days draw a scenario where, in VGO and VGN, the useful power level directed to the receiver appears more stable and constant during the daytime. This outcome would surely improve the thermal efficiency of the receiver and extend the lifetime of the subsystem, as it must face permanently strong thermal stresses. However some new aiming and defocusing strategies should come after, as also the maximum flux impinging on the absorber walls could be significantly more intense than the current one, especially during the first and last operation hours.

The four figures underline how efficiencies and powers levels are practically the same in the optimized and the non-optimized fields, even if a gap could be appreciated only during winter periods, in the tails of the curves. This means that a long optimization procedure is not really required in the studied case, and the optimal individual position of each heliomobile should be investigated just at low values of α_s.
One possible reason has to be sought in the restricted size of the field, since a small number of elements is expected to produce little optical reciprocal interference; additionally, the VGN is a field type that not only maximizes optical efficiency at 30° (or 65°), but also reveals itself as the best throughout the chosen range of α_s.

It's worth remembering that the advantages described herein are balanced by two major drawbacks; the management of the collector field, already rather complex, gets even more difficult as the system requires a higher level of automation and new security devices, both passive and active. Besides, increased parasitic losses should be taken into account as each heliomobile is equipped with a third electric motor.

9. Code Validation

The aim of this chapter is to validate the results previously introduced through a more detailed optical analysis. As a number of simplifications were assumed, it becomes essential to examine whether they are adequate or not; being the test facility still without receiver, there is no way to obtain the value of the concentrated flux conveyed within its aperture, so that the best option is represented by a powerful evaluation code.

Described previously also in chapter 5, Tonatiuh is a Monte Carlo ray tracer for the optical simulation of solar concentrating systems. Although it's open-source software, it's really accurate and easy to use and it has the potential to evolve into a benchmark for simulation and design of many optical systems.
Organized in "stages", the Graphical User Interface (GUI) provides 3D and tree views of the modelled system, which can be handled to analyze errors and imperfections; it's worth stressing this point, as the majority of similar codes do not allow this operation, leaving the user "blind" with respect to the input data. Furthermore, its plugin architecture makes it modular, allowing the user to add new geometries, new reflective materials or sun shape models.
Compared to Soltrace, another free available ray tracing software, the construction phase of the stage is easier: here, once defined the concentrator type and its location within the stage, a "tracker" orients it, according to its aim point and sun position.

The principal outcomes in Tonatiuh are represented above all by the lack of the user-guide and the visualization of the ray-tracing results; even if a small tutorial on the web is available and data input is intuitive, the user may get somehow lost during the first steps, so some practice is advisable, especially building the tree path.
About the second drawback, Tonatiuh gives as output a file consisting in seven-tuples of real numbers (one each photon) plus the power per photon in order to carry on the analysis on a different computational software like Mathematica, R or Matlab. Every photon launched impinges on a surface, it could be ground, a reflective or an absorber surface, and its related seven-tuple is made up by:

- Photon ID
- X coordinate
- Y coordinate
- Z coordinate
- Surface side
- Previous photon ID
- Next photon ID

Given the analyzed surface, in this case the receiver aperture, the user can select which coordinate system the output file is referring to, if local or global.

The basic stage is composed of the tower structure and four kinds of heliomobiles (or heliostats because of the punctual analysis): each one represents the type mounted on each row, as the reflective elements and canted on their individual slant range that is constant over each radius. Then, the position of every element in every row is added and the trackers are applied.
This optical analysis has been done for both the receiver apertures.

For all the runs, a pillbox sun shape was employed. Although less realistic than Buie's one, it considers the radiance coming from the Sun is constant over a cone of directions from the center of the Sun to the half angle of θ_{sun}, and drops to zero elsewhere. In other words, the standard deviation σ_{sun} is not taken into account, while σ_{track}enters inside the item σ_{slope}. The total standard deviation now becomes:

$$\sigma_{slope,Tonatiuh} = \sigma_{slope} + \sigma_{track}$$

Optical aberrations, on the other hand, are computed intrinsically because a ray tracer reproduces the path of the photons when they are mirrored by the spherical-canted surface.

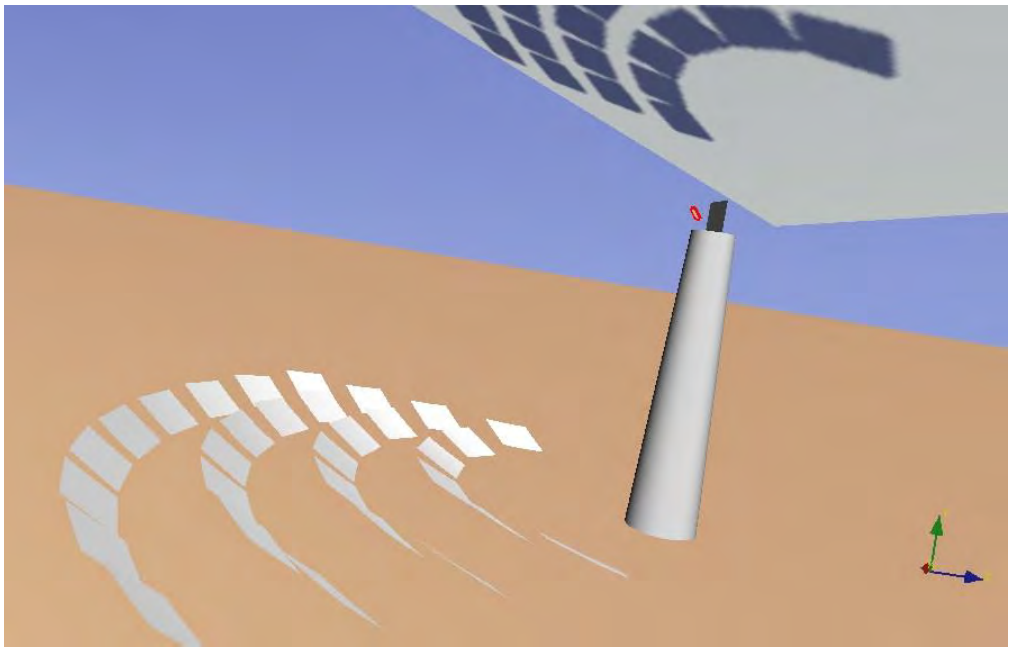

Figure 9-1: variable-geometry field in the 75-degrees configuration; the red boundaries delimit the circular aperture of the receiver.

For every field type, the sun plane is defined with the elevation correspondent to the field configuration and zero azimuth.

To compute the optical efficiency with Tonatiuh, it's necessary to determine the total concentrated power onto the aperture plane; then this is divided by the total incoming radiation power falling on the field. For sake of simplicity and uniformity, the DNI at each run is set to be 1000W/m^2.
In this way, the side effect of the validation is the chance to draw the flux maps associated to every field, thus completing the lack of the tool presented in chapter 6.
The method to derive the flux distribution is quite easy thanks to Matlab environment. The receiver plane, a square whose side equals $2R_{ap}$, undergoes a discretization in 900 parts;

Matlab reads the output file, then stores the photons impinging in each tessera and finally sums their specific power. The useful total power is the integration of those discretization points that are located within the aperture boundaries, while the incident total power is, like in chapter 6:

$$P_{incident} = n * A_h * DNI$$

The table 9-1 emerges from the comparison shows an interesting trend. At first, the code is not so far from being exact when R_{ap} = 1.145m; the tendency is even more evident at low solar elevation angles.
The reason which explains the phenomenon concerns the astigmatism. In the developed code, this aberration is modelled through an extra cone-error component, whose effect is to spread the circular Gaussian distribution of the reflected image. Actually, the deformation of such image approaches an ellipse and, even if the equivalent radial distribution mitigates the problem, it's cannot reproduce exactly a complex optical aberration. Reminding that at low elevation angles the angular span of the collector system reaches its maximum, the images of the furthest heliomobiles in each row are supposed to be more misshaped. We can deduce that the principal cause of the error is the assumption made in the interception efficiency calculation, where the single central reflected ray is not enough to model adequately the complex time-variant deformation. Nevertheless, even a simple ray tracing approach during field refinement would definitely enlarge computation time.

Table 9-1: optical efficiency comparison, developed code vs Tonatiuh

	R_{ap} = 1.145m			R_{ap} = 2.5m		
field type	$\eta_{opti,field}$	$\eta_{opti,Tonatiuh}$	**e%**	$\eta_{opti,field}$	$\eta_{opti,Tonatiuh}$	**e%**
10	0,4506	0,403	10,59	0,6015	0,592	1,60
15	0,5333	0,489	8,27	0,7012	0,703	-0,29
20	0,5914	0,538	9,03	0,7700	0,761	1,12
25	0,6307	0,596	5,44	0,8075	0,821	-1,62
30	0,6623	0,621	6,25	0,8366	0,840	-0,41
35	0,6774	0,654	3,47	0,8464	0,868	-2,58
40	0,6794	0,646	4,95	0,8511	0,861	-1,21
45	0,6762	0,649	4,05	0,8475	0,865	-2,02
50	0,6831	0,653	4,41	0,8509	0,862	-1,26
55	0,6762	0,652	3,65	0,8464	0,866	-2,27
60	0,6723	0,650	3,27	0,8419	0,863	-2,45
65	0,6796	0,663	2,47	0,8433	0,861	-2,10
70	0,6723	0,656	2,45	0,8362	0,853	-2,04
75	0,6612	0,644	2,57	0,8268	0,845	-2,18
80	0,6475	0,627	3,20	0,8150	0,833	-2,25

When R_{ap} = 2.5m, the percent difference is substantially lower. Although this may be seen as a reassuring factor, it must be noticed that, coupling the table with the flux map, the aperture area is clearly oversized, so this radius magnitude makes the analysis fail its ultimate goal, i.e. to find out whether the interception efficiency is well approximated or not. On the other hand,

the larger radius seems to verify that shading and blocking calculation method is matching its aim of precision, even if in the code a section of the tower, and not its volume, is projected.

Being e% the detected error its definition and its related trend as function of the solar field configuration is reported below:

$$e\% = \frac{\eta_{opti} - \eta_{Tonatiuh}}{\eta_{opti}} 100$$

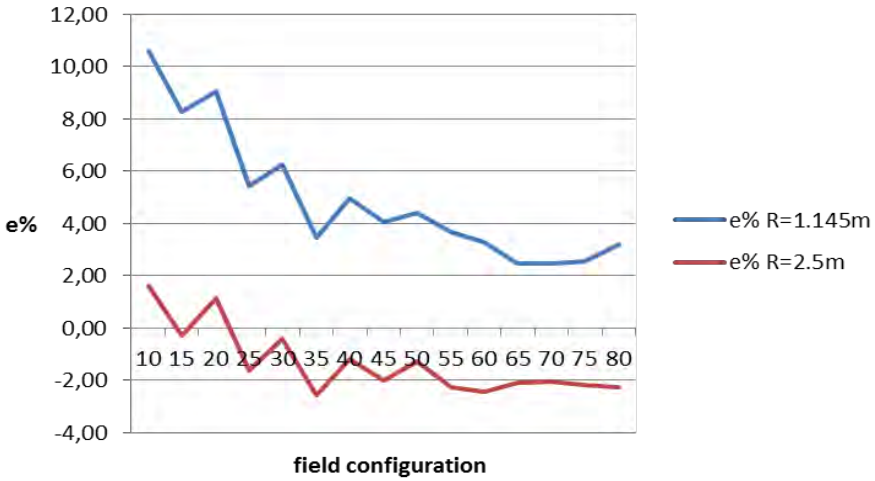

Figure 9-2: percent error as function of the variable-geometry field configuration

Flux map distributions help in providing a visual support to the statements of this chapter, underlining how receiver dimensions influence so strongly spillage losses. Maximum flux density values here may exceed 1000 kW/m^2, as one single aiming point was chosen; in real applications an aiming point strategy optimization is required to meet peak flux limitations, so that a little more spillage is admitted. Presented flux distribution therefore has to be intended as an upper level. In addition, flux maps show how much the bigger receiver aperture is oversized, as reported in figure 9-3.

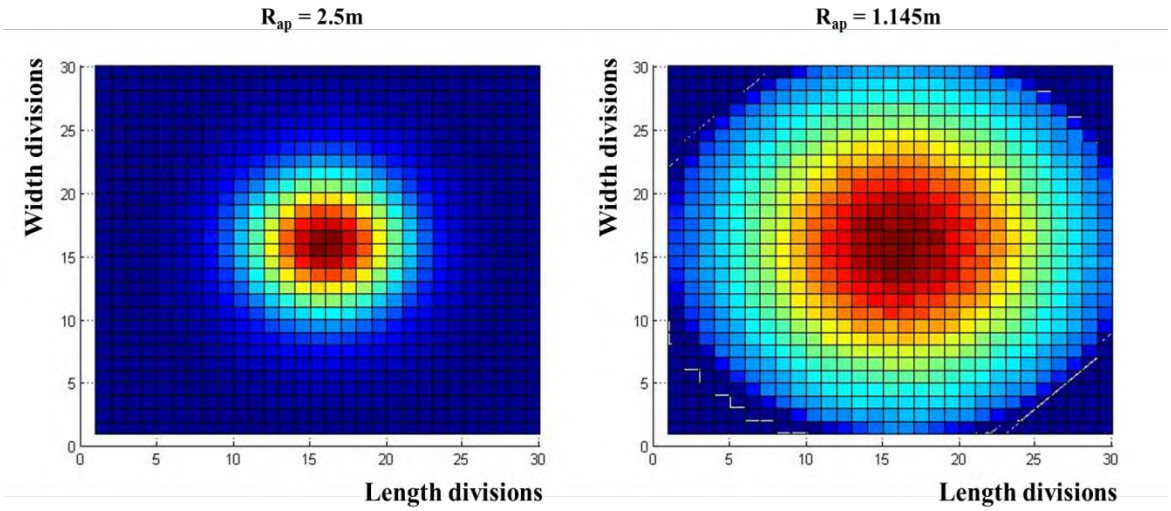

Figure 9-3: flux maps of 50-degrees configuration. Each square has a total length of $2R_{ap}$

A further ray-tracing analysis is performed for the three fields mentioned in chapter 8 over the four selected days of the year: the aim now is not only the comparison between the results given by the model and Tonatiuh, but also a deeper understanding of how concentrated rays impinge the aperture during the hours of each day. For this purpose, the smaller receiver radius is chosen as it appears the most suitable for the analyzed field. Tables 9-2 and 9-3 indicate that the error of the model follows the same aforementioned trend when dynamic fields are taken into account, but increases notably considering the spiral field. Peak error reaches the 35% on 21/6 at 18, and focusing on the average uncertainty, the main conclusion is that yearly and monthly predictions are quite overestimated.
Once more the key point seems spillage loss calculation: at low solar elevations and wide azimuthal angles, the high average cosine factor implies a substantial deformation of the images sent to the receiver plane, whose reproduction is the weak point of the model. An immediate example could be 18 (solar hour) on 21/6 when the optimized variable-geometry field has an average cosine factor equal to 0,937, the non-optimized one 0,954 and the spiral one 0,683.

Thanks to Tonatiuh it's possible to observe the influence of optical aberrations on the concentrated flux at the receiver. 21/6 is the day selected for this last comparison as the sun covers the widest apparent path in sky.
The maps underline that the spiral field (BF) undergoes an irregular flux especially in first hours of the morning, when image deformation implies spillage losses unknown by the two variable fields (VGN and VGO). As a result of the constant rotation during the day, their flux map does not change in shape, but only in intensity.

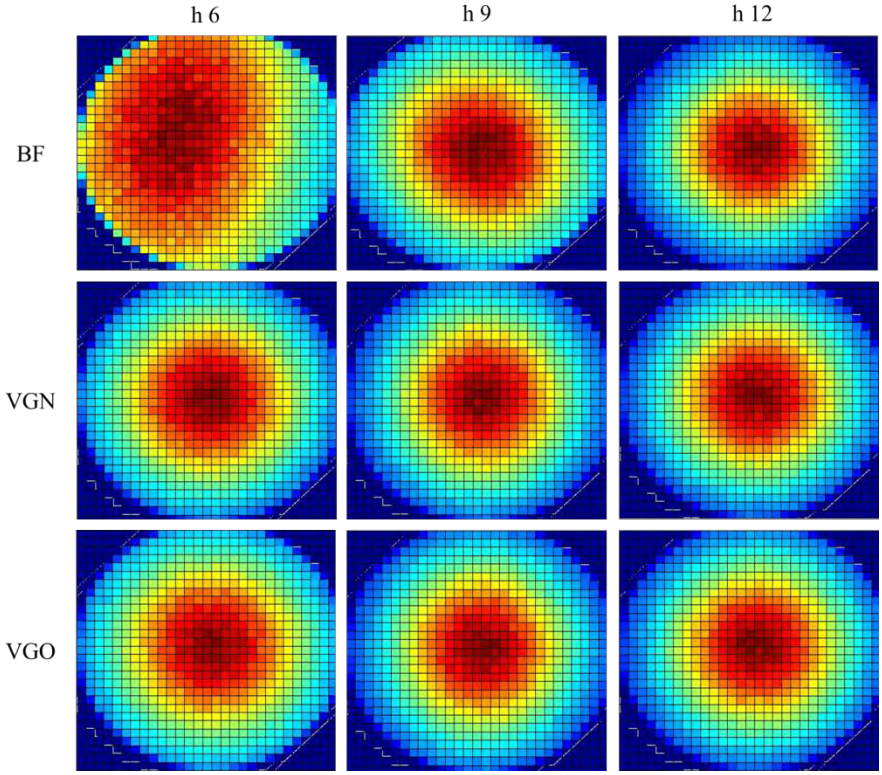

Figure 9-4: flux maps of the three analyzed fields on 21/6. R_{ap}= 1,145m

Table 9-2: daily comparison model-Tonatiuh

21-gen

				P_{rec} - model (kW)			P_{rec} - Tonatiuh (kW)			$e\%_{m-T}$			Flux max (kW/m^2)		
hour	**el (°)**	**az (°)**	**DNI (W/m^2)**	**VGO**	**VGN**	**BF**	**VGO**	**VGN**	**BF**	**VGO**	**VGN**	**BF**	**VGO**	**VGN**	**BF**
9	18,56	-44,45	875	1835	1743	1461	1681	1600	1275	8,37	8,18	12,73	787	773	579
10	25,90	-31,46	967	2227	2198	2002	2112	2055	1746	5,18	6,51	12,78	1045	1021	856
11	30,75	-16,42	1009	2410	2391	2331	2374	2291	2017	1,50	4,19	13,47	1172	1119	1027
12	32,46	0,00	1016	2436	2422	2439	2424	2340	2138	0,52	3,38	12,36	1209	1185	1075
13	30,75	16,42	993	2372	2353	2333	2335	2255	2038	1,52	4,16	12,64	1165	1115	1032
14	25,90	31,46	929	2141	2113	2017	2028	1975	1693	5,28	6,54	16,08	985	977	815
15	18,56	44,45	800	1678	1594	1434	1537	1462	1228	8,38	8,24	14,36	727	706	570

21-mar

				P_{rec} - model (kW)			P_{rec} - Tonatiuh (kW)			$e\%_{m-T}$			Flux max (kW/m^2)		
hour	**el (°)**	**az (°)**	**DNI (W/m^2)**	**VGO**	**VGN**	**BF**	**VGO**	**VGN**	**BF**	**VGO**	**VGN**	**BF**	**VGO**	**VGN**	**BF**
7	11,61	-80,43	658	1155	1069	720	1043	962	550	9,74	10,03	23,66	480	459	221
8	23,14	-70,35	834	1853	1812	1443	1749	1691	1227	5,61	6,72	15,00	859	825	537
9	33,88	-58,40	927	2227	2216	2023	2211	2147	1834	0,69	3,11	9,35	1094	1097	898
10	43,13	-43,25	978	2377	2377	2318	2347	2347	2113	1,27	1,26	8,84	1190	1180	1060
11	49,73	-23,60	1002	2440	2440	2491	2440	2440	2294	0,00	0,00	7,90	1247	1230	1193
12	52,20	0,00	1006	2448	2448	2519	2460	2459	2344	-0,49	-0,47	6,97	1275	1271	1237
13	49,73	23,60	992	2416	2416	2487	2417	2441	2289	-0,03	-1,03	7,96	1280	1260	1189
14	43,13	43,25	956	2324	2324	2289	2294	2295	2075	1,31	1,26	9,33	1169	1153	1040
15	33,88	58,40	888	2133	2123	1949	2117	2055	1735	0,74	3,21	10,97	1059	1017	821
16	23,14	70,35	763	1695	1658	1352	1601	1546	1167	5,54	6,72	13,66	784	768	512
17	11,61	80,43	511	898	831	563	809	748	430	9,90	10,02	23,71	369	350	169

Table 9-3: daily comparison model-Tonatiuh

21-giu

				P_{rec} - model (kW)			P_{rec} - Tonatiuh (kW)			$e\%_{m-T}$			Flux max (kW/m^2)		
hour	**el (°)**	**az (°)**	**DNI (W/m^2)**	**VGO**	**VGN**	**BF**	**VGO**	**VGN**	**BF**	**VGO**	**VGN**	**BF**	**VGO**	**VGN**	**BF**
6	13,99	-109,01	602	1138	1065	527	1051	967	369	7,66	9,24	30,03	485	460	129
7	25,49	-100,98	746	1711	1686	1085	1623	1576	820	5,14	6,55	24,44	806	769	309
8	37,31	-92,70	830	2007	2007	1520	1939	1940	1267	3,38	3,33	16,66	975	967	535
9	49,20	-83,15	882	2147	2147	1851	2148	2148	1651	-0,04	-0,05	10,78	1103	1099	754
10	60,79	-70,06	912	2194	2196	2082	2236	2232	1935	-1,91	-1,63	7,06	1179	1143	944
11	71,03	-46,91	927	2180	2181	2217	2224	2216	2092	-2,02	-1,63	5,66	1148	1128	1097
12	76,05	0,00	930	2149	2148	2259	2185	2178	2142	-1,66	-1,36	5,20	1111	1106	1137
13	71,03	46,91	921	2165	2166	2214	2207	2201	2088	-1,91	-1,61	5,70	1142	1129	1099
14	60,79	70,06	898	2162	2164	2073	2201	2196	1922	-1,77	-1,48	7,31	1138	1138	953
15	49,20	83,15	859	2092	2092	1824	2091	2090	1629	0,01	0,06	10,71	1058	1087	742
16	37,31	92,70	793	1917	1917	1479	1851	1853	1232	3,44	3,32	16,70	966	930	506
17	25,49	100,98	684	1568	1546	1025	1488	1445	761	5,11	6,48	25,74	727	714	287
18	13,99	109,01	491	928	869	491	855	789	317	7,82	9,22	35,28	393	376	111

21-dic

				P_{rec} - model (kW)			P_{rec} - Tonatiuh (kW)			$e\%_{m-T}$			Flux max (kW/m^2)		
hour	**el (°)**	**az (°)**	**DNI (W/m^2)**	**VGO**	**VGN**	**BF**	**VGO**	**VGN**	**BF**	**VGO**	**VGN**	**BF**	**VGO**	**VGN**	**BF**
9	15,88	-42,41	866	1716	1615	1341	1587	1473	1161	7,52	8,82	13,47	728	708	525
10	22,92	-29,87	961	2127	2080	1864	2009	1943	1643	5,54	6,58	11,87	960	948	788
11	27,53	-15,53	1003	2352	2326	2193	2262	2181	1918	3,84	6,21	12,55	1137	1075	961
12	29,15	0,00	1012	2403	2379	2362	2337	2254	2038	2,75	5,26	13,71	1178	1128	1034
13	27,53	15,53	989	2320	2294	2229	2230	2151	1974	3,89	6,23	11,42	1090	1066	1025
14	22,92	29,87	924	2047	2001	1899	1931	1866	1591	5,66	6,77	16,23	929	909	758
15	15,88	42,41	786	1558	1467	1307	1439	1338	1098	7,63	8,81	15,96	671	652	495

10. Conclusions

The objective of this study was the optimization of the collector field configuration for the first variable-geometry central receiver system test facility. The structure based on this new CSP concept is under construction at CTAER in Almería and its principal innovative characteristics could be resumed in:

- rotating collector field around a tower, placed in the center of the field itself
- solar power concentrated by heliomobiles
- rotating receiver

The system introduces intrinsically some changes with respect to a conventional central receiver, so that now the operation strategy must deal with the increased dynamics of the reflective surfaces.
The reason which justifies this research is that in a conventional CRS, the solar field is the most expensive subsystem in the plant and, at the same time, is affected by a high absolute value of exergetic losses. Boosting its efficiency would result directly in a lower LCOE when such systems are employed to generate electric power.

A review of the existing codes dedicated to central receiver systems was carried on and illustrated the current lack of software and tools that can assess energy simulation or field layout optimization for the analyzed facility. In order to fulfill the goal of the project, both evaluation and optimization tools were developed in Matlab.

Field simulation evaluates the amount of useful power conveyed at the receiver by calculating cosine, shading and blocking, atmospheric attenuation, reflectivity and spillage losses; furthermore the shadow cast by the tower is included and optical efficiency can be obtained also for polar conventional collector subsystems of large solar power plants.

Secondly, based on a field configuration developed through a modified version of the NSPOC code, an optimization method for heliomobile deployment was introduced, exploiting the Genetic Algorithm of the Global Optimization Toolbox in Matlab, under some hypothesis and constraints.
As the field and the receiver move synchronously with the sun, the optical efficiency is not sensitive to variations of solar azimuthal angle throughout the day, so that the optical efficiency of the variable-geometry field was maximized by finding the optimal deployment of the heliomobiles for each solar elevation angle. A further refinement was performed in order to neglect the configurations that led to the lowest local optima. Best deployments show that the optimization process draws a field more widened during early morning or late afternoon, in order to limit shading and blocking interactions.

In order to fully evaluate the potential of the optimized variable-geometry field, it was compared with other two field types: a non-optimized variable-geometry field and spiral-layout field. Last pattern was chosen because recent studies demonstrated that it reaches higher optical efficiency than the radially-staggered or the grid one. In section 8.2 a method to design the spiral field was explained.
The comparison was carried on considering the same number of reflective elements and two

different aperture surfaces; yearly, monthly and daily simulations led to the final considerations and results:

- dynamic fields are able to convey more energy at the receiver, about 10% during the whole year and a peak of 15% on the day 21/6
- the smaller the aperture of the receiver, the higher the difference in energy conveyed between dynamic and static systems
- in a small field, like the one analyzed, there is no substantial difference in energy conveyed to the receiver between the two considered variable-geometry fields (≈ 1%)
- in a variable-geometry field, flux distribution impinging onto aperture surface is more uniform during the day.

Increased energy at the receiver is mainly due to field movement throughout the day, which strongly reduces cosine losses, while the difference between the optimized and the non-optimized variable fields (≈ 1%) just represents the avoided shading and blocking losses at low solar elevation angles. As a matter of facts, this is the only appreciable effect of the optimization process, meaning that it makes sense only during winter time or till solar elevation $\alpha_s \leq 35°$.
Beside the higher annual energy yield, the variable-geometry field presents some interesting features more. Keeping the average cosine efficiency as close to 1 as possible during the day, the shape of the flux image conveyed to receiver aperture is far more constant than the one of a static field, thus spillage losses are limited. On the other hand, this intrinsic characteristic ease receiver design and makes it less subject to substantial time-variant thermal stresses which decrease receiver life. Ray-tracing analysis reveals that in a dynamic field the higher flux is located always in the aperture center, while in the analyzed static field it spreads over one side at low solar elevation angles, when optical aberrations are dominant.
Last two advantages appears to be secondary, but still notable: management and communication with the heliomobile is realized via wi-fi, so that long wiring and cables under the ground are avoided, and, although not examined here in detail, focusing and defocusing operations, like aiming strategy implementation, are eased by the independent movement of each heliomobile.
Despite the improved efficiency, this innovative field is not exempt from three principal drawbacks. First, land usage is extremely high, and such problem would be even increased for big power plant (> 1000 reflective elements),then the management of the operation and security systems are rather more complex because of the new dynamics, and more parasitic losses have to be taken into account, as each heliomobile is equipped with a third electric motor.
Finally, it is worth bearing in mind that this new concept has been built for research and not commercial purposes, which makes this facility suitable for a large number of tests, spacing from different receiver or concentrator types to various heliomobile deployments, as they can be freely arranged on the rails.

This research focused on small collector systems, whereas central receiver systems are usually equipped with an extremely large number of heliostats. Some further studies should prove or deny the tendency for a commercial-scale plant (about 1000 heliostats); this is not possible with the developed Matlab script as the time required would rise to unacceptable values and it

would presume a revolution in tool architecture, which is not within the means of who writes. A method that could succeed in the case of large fields should be close to the one adopted in YNES, a code described in chapter 5: there the field is divided into a grid and the nodes which presents the highest incoming normalized radiation are selected.

Specifically about the tool, it can calculate with good approximation the optical efficiency for large and small fields, but its major outcome is represented by spillage calculation. Here, the interception factor is deduced by a statistical method based on the convolution of some standard deviations that stand for optical errors. This approach was selected because of the guaranteed speed, a very valuable characteristic when the optimization algorithm must run that particular function thousands of times. Supported by the Central Limit Theorem, this method proved to be really fast and reliable when the number of reflective elements checked is numerous, less when it's adopted in small solar fields.
Two calculation methods may significantly improve the estimate of the interception factor: the discretization of the reflective surface, in order to increase the number of the distributions and accelerate the convergence to a more exact value, or a hybrid ray-tracing/convolution method, which would be a right trade-off between computation time and precision. Additionally both the suggested modifications couple well with the direct evaluation of the flux distribution at the receiver.
The last comment concerns the angular speed of the elements in the mobile field. The heliomobiles are supposed to move synchronously with the sun throughout the day, although their rotation around the central receiver will not be continuous, but rather discretized according to a precise time-step. Further analyses should evaluate the additional energy loss due to the mismatch between the real and the ideal position of the field and optimize the aforementioned time-step.

Acknowledgements

A diferencia de la disertación, esta última página empieza en español ya que las primeras personas que quiero agradecer son las que me han acompañado durante este segundo año de mi aventura sevillana.
En primer lugar, mi gratitud va a Manuel Silva, que ha permitido que me acercara a este proyecto de investigación y que ha sido capaz de guiarme durante los momentos más críticos, cuando iba perdido entre códigos desconocidos y tentativas infructuosas. Luego un enorme gracias a todo el GTER de Sevilla, a Elena, Jose, Miguel y Sara, por todo lo que he aprendido de ellos (maldito Matlab) y sobre todo por la risas, ¡sin vosotros me habría vuelto loco después de dos meses!
A la vez, no puedo no agradecer a Miguel Frasquet, sus consejos, su habilidad en aclarar mis dudas y su disponibilidad han sido fundamentales en la realización de este trabajo, así como la ayuda de Rosa, Fernando y Pablo del CTAER.

Un "gracias" distinto es para los que más han representado mi vida en Sevilla, en particular a Alegría, Bianca, Chomi, Daniel, Giacomo, Jose, Laura, Lele, Nino y Paula; gracias por haberme esperado, por haberme regalado bellísimos momentos, grandes tardes, fantásticas noches y "mañanas" horribles: Sevilla, aunque preciosa, no habría podido convertirse en especial sin vosotros…y claramente sin la freiduría de calle Feria y el Nikkei y la Bicicletería, y el FunClub y el depósito de la grúa municipal.

Spostandomi a Padova invece desidero ringraziare il prof. Del Col, che ha seguito l'ultima parte di questo cammino, e la prof.ssa Stoppato, dimostratasi sempre disponibile nell'aiutarmi tra dubbi, piano di studi ed esami.
Non un semplice grazie, forse più un abbraccio, va a tutti coloro che hanno saputo farmi risentire a casa in un'attimo quando tornavo in patria, ed in particolare a Alberto, Beppe, Borto, Chiap, Chiara, Fil (meglio una statua), Fra, Jack, Giulio, Irene, Luca e Rugge. Voi, e non solo, rappresentate il lato di Padova che più mancava in terra spagnola(so che al momento del papiro questa ruffianata non mi aiuterà, ma almeno ci avrò provato).

Tutta la mia riconoscenza va poi alla mia famiglia, che mi ha sempre incoraggiato e sostenuto, nonostante a volte non riuscissi a vedere più in là del palmo della mia mano.

Infine, un grazie di cuore a chi mi ha aspettato.

Padova, 9 ottobre 2014 L.C.

Bibliography

A.T. Kerney GmbH, 2010. *Solar Thermal Electricity 2025,* s.l.: s.n.

Aichmayer, L., 2011. *Solar Receiver Design and Verification for Small Scale Polygeneration Unit.* Royal Institute of Technology, Stocholm: Master of Science Thesis.

Ailight Energy, n.d. *http://www.airlightenergy.com/.* [Online].

Augsburger, G., 2013. *Thermo-economic optimisation of large solar tower power plants.* École Polytechnique Fédérale de Lausanne: Thèse pour l'obtention du grade de Docteur ès Sciences.

Ávila-Marín, A. L., 2011. Volumetric receivers in Solar Thermal Power Plants with Central Receiver System technology: A review. *Solar Energy,* Issue 85, pp. 891-910.

Ballestrín, J. & Marzo, A., 2012. Solar radiation attenuation in a solar tower plant. *Solar Energy,* Volume 86, pp. 388-392.

Behar, O., Khellaf, A. & Mohammedi, K., 2013. A review of studies on central receiver solar thermal power plants. *Renewable and Sustainable Energy Reviews,* Issue 23, pp. 12-39.

Belhomme, B., Pitz-Paal, R. & Schwarzbözl, P., 2014. Optimization of Heliostat Aim Point Selection for Central Receiver Systems Based on the Ant Colony Optimization Metaheuristic. *Journal of Solar Energy Engineering,* Volume 136, pp. 1-7.

Belhomme, B., Pitz-Paal, R., Schwarzbözl, P. & Ulmer, S., 2009. A New Fast Ray Tracing Tool for High-Precision Simulation of Heliostat Fields. *Journal of Solar Energy Engineering,* Volume 131, pp. 1-8.

Besarati, S. M. & Goswami, D. Y., 2014. A computationally efficient method for the design of the heliostat field for solar power tower plant. *Renewable Energy,* Volume 69, pp. 226-232.

Blackmon, J. B., 2012. Heliostat size optimization for central receiver solar power plants. In: K. Lovegrove & W. Stein, eds. *Concentrating solar power technology - Principles, developments and applications.* s.l.:Woodhead Publishing Limited, pp. 535-576.

Blanco Muriel, M., 1985. *Cálculo del rendimiento geométrico del campo de heliostatos. Aplicación a la planta CRS del proyecto IER-SSPS,* Universidad de Sevilla: Master of Science Thesis.

BP, 2013. *BP.* [Online] Available at: http://www.bp.com/en/global/corporate/about-bp/energy-economics/statistical-review-of-world-energy-2013/energy-charting-tool.html

Buck, R., 2014. Heliostat Field Layout Improvement by Nonrestricted Refinement. *Journal of Solar Energy Engineering,* Volume 136, pp. 1-6.

Buck, R. et al., 2002. Solar-Hybrid Gas Turbine-based Power Tower Systems (REFOS)*. *Journal of Solar Energy Engineering,* 124(1), pp. 2-9.

Buck, R. & Teufel, E., 2009. Comparison and Optimization of Heliostat Canting Methods. *Journal of Solar Engineering,* Volume 131, pp. 011001 1-7 .

Chen, Y. T. et al., 2001. Non-imaging, focusing heliostat. *Solar Energy,* 71(3), pp. 155-164.

Chong, K.-K. & Tan, M. H., 2012. Comparison Study of Two Different Sun-Tracking Methods in Optical Efficiency of Heliostat Field. *International Journal of Photoenergy,* 2012(Article ID 908364), p. 10.

Coley, D. A., 1999. *An Introduction to Genetic Algorithm for Scientists and Engineers.* First ed. Singapore: World Scientific Publishing.

Collado, F. & Guallar, J., 2013. A review of optimized design layouts for solar power tower plants with campo code. *Renewable and Sustainable Energy Reviews,* Issue 20, pp. 142-154.

Collado, F. J., Gómez, A. & Turégano, J. A., 1986. An analytic function for the flux density due to sunlight reflected from a heliostat. *Solar Energy,* Issue 37, pp. 215-234.

Collado, F. J. & Turégano, J. A., 1989. Calculation of the annual thermal energy supplied by a defined heliostat field. *Solar Energy,* 42(2), pp. 149-165.

Duffie, J. A. & Beckman, W. A., 2006. *Solar Engineering of Thermal Processes.* X ed. s.l.:John Wiley & Sons, Inc..

Garcia, P., Ferriere, A. & Bezian, J.-J., 2008. Codes for solar flux calculation dedicated to central receiver system applications: A comparative review. *Solar Energy,* Issue 82, pp. 189-197.

Gil, A. et al., 2010. State of the art on high temperature thermal energy storage for power generation. Part 1—Concepts, materials and modellization. *Renewable and Sustainable Energy Reviews,* Volume 14, pp. 31-55.

Giuliano, S., Buck, R. & Eguiguren, S., 2011. Analysis of Solar-Thermal Power Plants With Thermal Energy Storage and Solar-Hybrid Operation strategy. *Journal of Solar Energy Engineering,* Issue 133, pp. 1-7.

Guo, M. & Wang, Z., 2011. On the analysis of an elliptical Gaussian flux image and its equivalent circular Gaussian flux images. *Solar Energy,* Issue 85, p. 1144–1163.

Haupt, R. L. H. S. E., 2004. *Practical Genetic Algorithms.* Second ed. Hoboken, New Jersey: Wiley-Interscience Publications.

Ho, C. K., 2008. *Software and Codes for Analysis of Concentrating Solar Power Technologies,* s.l.: Sandia National Laboratories.

Ho, C. K. & Iverson, B. D., 2014. Review of high-temperature central receiver designs for concentrating solar power. *Renewable and Sustaineble Energy Reviews,* Issue 29, pp. 835-846.

Igel, E. A. & Hughes, R. L., 1979. Optical analysis of solar facility heliostats. *Solar Energy,* Volume 22, pp. 283-295.

International Energy Agency, 2010. *Technology Roadmap - Concentrating Solar Power,* s.l.: IEA PUBLICATIONS.

International Energy Agency, 2012. *World Energy Outlook 2012,* s.l.: IEA PUBLICATIONS.

International Energy Agency, 2013. *World Energy Outlook 2013,* s.l.: IEA PUBLICATIONS.

IRENA, 2012. *RENEWABLE ENERGY TECHNOLOGY: COST ANALYSIS SERIES - Concentrating Solar Power,* s.l.: s.n.

IRENA, 2012. *Renewable Power Generation Cost.* [Online] Available at: https://www.irena.org/DocumentDownloads/Publications/Renewable_Power_Generation_Costs.pdf

Kasten, F. & Young, T., 1989. Revised Optical Air-Mass Tables and Approximation Formula. *Applied Optics,* Volume 28, pp. 4735-4738.

Kistler, B. L., 1986. *A User's Manual for DELSOL3: A Computer Code for Calculating the Optical Performance and Optimal System Design for Solar Thermal Central Receiver Plants,* s.l.: Sandia National Laboratories.

Kolb, G. J. et al., 2007. *Heliostat Cost Reduction Study,* s.l.: Sandia National Laboratories.

Kuravi, S. et al., 2013. Thermal energy storage technologies and systems for concentrating solar power plants. *Progress in Energy and Combustion Science,* Volume 39, pp. 285-319.

Lee, H., 2014. The geometric-optics relation between surface slope error and reflected ray error in solar concentrators. *Solar Energy,* Volume 101, pp. 299-307.

Leonardi, E. & D'Aguanno, B., 2011. CRS4-2: A numerical code for the calculation of the solar power collected in a central receiver system. *Energy,* Issue 36, pp. 4828-4837.

Lovegrove, K., 2012. Fundamental principles of concentrating solar power (CSP) systems. In: K. Lovegrove & W. Stein, eds. *Concentrating solar power technology - Principles, developments and applications.* s.l.:Woodhead Publishing Limited, pp. 16-67.

Lovegrove, K. & Stein, W., 2012. *Concentrating solar power technology - Principles, developments and applications.* I ed. s.l.:Woodhead Publishing Limited.

Mar, R. W. & Swearengen, J. C., 1981. Material issues in solar thermal energy systems. *Solar Energy Material,* Issue 5, pp. 37-53.

Mills, D. R., 2012. Linear Fresnel reflector (LFR) technology. In: K. Lovegrove & W. Stein, eds. *Concentrating solar power technology - Principles, developments and applications.* s.l.:Woodhead Publishing Limited, pp. 151-196.

Noone, C. J., Torrilhon, M. & Mitsos, A., 2012. Heliostat field optimization: A new computationally efficient model and biomimetic layout. *Solar Energy,* Volume 86, pp. 792-803.

Osuna, R. et al., 2006. *PS10, construction of a 11 MW solar thermal power plant in Seville, Spain.* Sevilla, SolarPACES.

Pacheco, J. E. et al., 2002. *Final Test and Evaluation Results from the Solar Two Project,* s.l.: Sandia National Laboratories.

Pitz-Paal, R., 2007. HIGH TEMPERATURE SOLAR CONCENTRATORS, in Solar Energy Conversion and Photoenergy System . In: *Encyclopedia of Life Support Systems (EOLSS).* Oxford: Eolss Publishers.

Pitz-Paal, R., Bayer Botero, N. & Steinfeld, A., 2011. Heliostat field layout optimization for high temperature solar thermochemical processing. *Solar Energy,* Volume 85, pp. 334-343.

Quero, M. et al., 2013. *Solugas - Operation experience of the first solar hybrid gas turbine system at MW scale.* Las Vegas, USA, SolarPACES 2013.

Rabl, A., 1975. Comparison of solar concentrators. *Solar Energy,* Volume 18, pp. 93-111.

Ramos, A. & Ramos, F., 2012. Strategies in tower solar power plant optimization. *Solar Energy,* Volume 86, pp. 2536-2548.

Reno, M. J., Clifford, W. C. & Stein, J. S., 2012. *Global Horizontal Irradiance Clear Sky Models: Implementation and Analysis,* Albuquerque, New Mexico, USA: Sandia Report.

Romero-Alvarez M., Z. E., 2007. Chapter 21 - Concentrating Solar Thermal Power. In: *Handbook of Energy Efficiency and Renewable Energy.* s.l.:s.n.

Romero, M., Marcos, M. J., Osuna, R. & Valerio, F., 2000. *Design and implementation plan of a 10 MW solar tower power plant based on a volumetric-air technology in Seville (Spain).* Madison, Wisconsin, Proceedings of the Solar 2000 Solar Powers Life-Share the Energy.

Sánchez, M. & Romero, M., 2006. Methodology for generation of heliostat field layout in central receiver systems based on yearly normalized energy surfaces. *Solar Energy,* Volume 80, pp. 861-874.

Schell, S., 2011. Design and evaluation of eSolar's heliostat fields. *Solar Energy,* Volume 85, pp. 614-619.

Schramek, P. & Mills, D. R., 2003. Multi-tower solar array. *Solar Energy,* Volume 75, pp. 249-260.

Schwarzbölz, P. S. M. P.-P. R., 2008. *Visual HFLCAL - a software tool for layout and optimization of heliostat fields.* Berlin, SolarPACES.

Segal, A. & Epstein, M., 1999. Comparative performances of "tower-top" and "tower-reflector" central solar receiver. *Solar Energy,* 65(4), pp. 207-226.

Siala, F. M. F. & Elayeb, M. E., 2001. Mathematical formulation of a graphical method for a no-blocking heliostat field layout. *Renewable Energy,* Volume 23, pp. 77-92.

Siemens, 2010. *Steam turbines for CSP plants,* s.l.: Siemens AG.

Silva, M. A., 2002. *Estimación del recurso solar para sistemas termosolares de concentración.* Universidad de Sevilla: Master of Philosophy Thesis.

Sproul, A. B., 2007. Derivation of the solar geometric relationships using vector analysis. *Renewable Energy,* Volume 32, pp. 1187-1205.

United Nations, 2011. *International Reccomendations for Energy Statistics (IRES),* New York: s.n.

Vant-Hull, L. L., 2012. Central tower concentrating solar power (CSP) system. In: K. Lovegrove & W. Stein, eds. *Concentrated solar power technologies.* s.l.:Woodhead Publishing Limited, pp. 240-283.

Yogev, A., Kribus, A., Epstein, M. & Kogan, A., 1998. Solar "tower reflector" system: a new approach for high-temperature solar plants. *International Journal for Hydrogen Energy,* 23(4), pp. 239-245.

Zaibel, R., Dagan, E., Karni, J. & Ries, H., 1995. An astigmatic corrected target-aligned heliostat for high concentration. *Solar Energy Materials and Solar Cells,* Volume 37, pp. 191-202.